An Optical Fibre based Force Apparatus

Applications to Soft and Living Matter

by

Seshagiri Rao R V

A thesis submitted to the Jawaharlal Nehru University
for the degree of Doctor of Philosophy

April 2015

DECLARATION

I, hereby, declare that this thesis is composed independently by me at Raman Research Institute, Bangalore, India, under the supervision of Dr.Pramod A Pullarkat. The subject matter presented in this thesis has not previously formed the basis of the award of any degree, diploma, associateship, fellowship or any other similar title in any other University.

Dr.Pramod A Pullarkat
Raman Research Institute

Seshagiri Rao R V

CERTIFICATE

This is to certify that the thesis entitled **An Optical Fibre based Force Apparatus Applications to Soft and Living Matter** submitted by Seshagiri Rao R V for the award of the degree of DOCTOR OF PHILOSOPHY of Jawaharlal Nehru University is his original work. This has not been published or submitted to any other University for any other degree or diploma.

Dr. Ravi Subramaniam
Director
Raman Research Institute

Dr.Pramod A Pullarkat
Thesis Supervisor

ACKNOWLEDGEMENTS

There are many people who contributed directly or indirectly in making this thesis work a reality. I would like to take this opportunity to express my gratitude to all of them.

My first expression of thanks goes to my PhD supervisor, Dr.Pramod Pullarkat, who accepted to take me as his student despite knowing my weird background. He showed a lot of patience throughout these years, continuously encouraged me to handle situations of all types without which the project would not been a success. I would like to thank Chirag Kalelkar who contributed in the calibration of the device and one of the problems pursued.

During my PhD years, Prof. Yashodhan Hatwalne and Dr. Sadiq Rangwala assessed my work every year, not only for the annual review, but with a genuine concern about my work and a wish to see me improve my capabilities. I sincerely thank them. I acknowledge Dr.Ashish Lele (NCL,Pune), Dr.Rononojoy adhikari (IMSC,Chennai), Dr.Sanjib Sabhapandit (RRI), Prof.Avinash DeshPande(RRI), Prof.Shriram Ramaswamy (TCIS,Hyderabad) Prof. Abhishek Dhar (ICTS), Prof. Joseph Samuel (RRI) for helpful discussions.

I wish to thank Shubham, who has an indispensable role in some of the experiments. His uncompromising hard work, enthusiasm and adaptability actually inspired me remain optimistic in a few moments of doubt.

I acknowledge Prof. Judith Albert (Oxford), Prof.Sandy Parkinson (Utah) and their lab members for supplying bacterial strains and discussing necessary protocols.

I am grateful to the technical staff of RRI, in particular the mechanical workshop. Achan, no words to describe his skills. He created a few master pieces of mechanical accessories of the device we built. I thank Mr. Dhason, Mr. Ram, Mr mani, Mr. Venu, and Mr. Paul from the mechanical workshop of RRI for helping my experiments run smooth. I thank Som , Rishin and other technical staff of electronics work shop. I thank our group secretary Radhakrishna and other staff including Ishaq, Murali and Raja. I would also like to thank RRI Administration for taking care of most of the formal/official procedures from time to time.

When it comes to lab mates, It had always been a pleasant and warm environment. we spent time together in high and low. PhD life would have been much harder without them being around. I thank Renu, Sushil, Roli, Som, Venu, Chandrasekhar, Sampada, Alka and Susav ... for being there.

The there are my good pals, Chandrakant, mamta(Mom), Nishant, Pragya, Madhukar, JK, Mari and Som. It was always a happy time with them.

Azhar and Anagha. I don't think there is any point being formal with them.

My sisters and their family members were always with me supporting,cheering and encouraging.

Last but not the least, my mother, Habeeba and Isa, each of them unique in their ways, made my life wonderful.

Seshagiri Rao R V
Bangalore
June, 2014

SYNOPSIS

Force plays a fundamental role in several physical as well as biological processes. Force measurement has been an important branch of sciences and engineering. A variety of force measurement techniques enabled powerful exploration of many areas of science including physics and biology.

In the force range of micro-newton to pico-newton or less, there are a variety of instruments catering to a broad range of applications. In this field some of the more widely used force devices include Atomic Force Microscope (AFM) optical tweezers and magnetic tweezers. Apart from these techniques, several methods such as pulling neurons using micro-needles, live-cell rheology using micro-plates, stretching DNA using etched optical fibres etc., have been developed for specific applications in mechano-biology and other disciplines.

Another emerging field that is employing sophisticated force measurement techniques is extensional rheology. Extensional properties of materials are important because extensional modes of deformation are obtained in a wide variety of industrial and laboratory settings, including tensile testing of materials, flow from an orifice, fibre-spinning of a thread, atomization involving breakup of liquid jets, flow through porous media, stagnation-point flows among others.

Dynamics of active matter, explored using statistical physics and hydrodynamics, is yet another area where force measurements at pico-scale can contribute to make it experimentally rich. An understanding of model active systems, even at a phenomenological level, provides insight about fundamental non-equilibrium statistical physics and, potentially, about the inner workings of biological systems.

While a variety of instruments and techniques are available in the field of force measurement and extension rheology, there are areas where novel methods of force application are in demand. Considering the biological cells like neurons a device which can pull on axons while performing simultaneous microscopy can facilitate understanding their mechanical properties. Similarly in the field of extensional rheology there are no rheometers that can operate at microscopic scale to probe

materials properties. Studies of active particle systems too is provided with limited means of experimental techniques and state of art direct force measurement methods are needed to probe several aspects of the dynamics of the self propelled systems.

As a major part of this thesis, We developed a cantilever based force transducer, which has pico-newton resolution in force and a few nano-meter in position. It has demonstrated capabilities to probe some of the problems in the areas of mechano-biology, extension rheology and active matter dynamics. We used the setup to pull on axons, form micro-scale filaments from synthetic polymers and study the dynamics of E.coli. The capability of the instrument covers a wide range in force measurement from the order of a milli-newton to that of a pico-newton. The device on one hand shares the features with single molecule force spectroscopy techniques like AFM, Optical Tweezers and Magnetic tweezers and on the other hand it works as an extension Rheometer at microscopic scales.

Technical details of the device and the experiments performed are explained in the following sections. These sections represent the respective chapters in this thesis.

Chapter 2 - Instrumentation

This chapter describes the design, working and the calibration protocols of our force device.

We developed a force measurement device which uses an etched optical fibre as a force-sensing cantilever. The working area of this device comprises a piezoelectric transducer and an optical fibre coupled to a laser, placed above the objective of a microscope. A cylindrical portion of the optical fibre acts as the cantilever for force sensing. The length and diameter of the cantilever can be adjusted to achieve the desired force sensitivity. The tip of the cantilever is seen as a bright spot through the microscope when laser light is coupled into the fibre. A Position-Sensitive Detector (PSD) is used to track its motion or deflection.

The device can be operated in passive or active modes. In the passive mode the

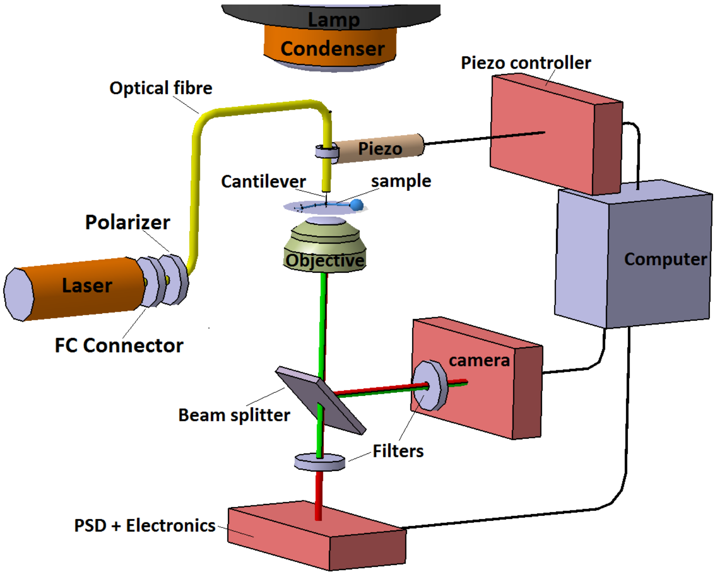

Figure 1: Schematic of MER, for transverse pulling experiments. Laser light coming out of the calibrated cantilever is focused on to a CCD camera and a PSD which track the position of tip of the cantilever. Cantilever tip is attached to the cell and is pulled using a piezo, normal to the cylindrical axis of the cell.

cantilever senses the force exerted by the surrounding medium. Force is measured using the deflection of the cantilever and its spring constant. In the active mode a piezo actuator is used to apply the force. In a set of experiments where the setup is used to pull on axons, the cantilever tip is attached to the axon and is pulled using a piezo, normal to the cylindrical axis of the cell where the two ends of the axon are fixed. In another set of experiments the extensional rheological properties of liquids are studied. In this experiment a few pico litre-volume of the sample is placed within the gap between the tip of the cantilever and another rigid rod mounted parallel to the cantilever, and the rigid rod is driven by the piezo. In the force application mode the piezo displacement equals the sum of the cantilever deflection and the sample extension.

The setup was mounted on a vibration-isolation table. A 17mW He-Ne laser, operating at an output wavelength of 633nm was used. The laser intensity was controlled by a linear polariser. One end of an optical fibre was coupled to the laser source using an FC connector. The single-mode optical fibre used has a mode field diameter (core) of 4.3μm for a design wavelength of 633nm, and a fibre outer diameter of $125 \pm 1\mu$m. A portion of the other end of the fibre was etched to required diameter using Hydrofluoric acid and was used as the cantilever in the force measurement experiments. A CCD camera, a position sensitive detector (PSD) and a quadrant photo diode (QPD) were used, based on the need, to detect the cantilever position, and the sample imaging was performed using the CCD camera. The sample was illuminated by green light using an interference filter placed above the microscope condenser. A red-absorption filter was placed in front of the camera to attenuate the intensity of the laser light incident on it, while allowing the scattered light (green) due to the sample to pass almost unhindered. In this method both the laser spot (tip of the cantilever) and the sample can be imaged simultaneously.

Cantilever was calibrated for its spring constant using Two different methods. In one of the methods the cantilever was excited to its resonance frequency. Spring constant of the cantilever was calculated using this frequency, mechanical properties of the cantilever material and the cantilever dimensions. In the other method Young's modulus of the cantilever material was found using static bending of the cantilever. Given the length and diameter of the cantilever its spring constant can be calculated using the calibration factor as $5.63 \times 10^{-5} \times d^4/l^3$. The diameter of the cantilever can be tuned between 125μm and 6μm by etching and the desired length can be obtained by cutting the fibre and hence the spring constant of the cantilever can be tuned in a wide range. We calibrated the camera, the PSD and the QPD using standard protocols. The three detection modes are compared in the table (2.2) With the calibration of the cantilever and the position detection devices, we get position resolution of the order of few nano-meter, force resolution of the order of a pico-newton and a wide force range of milli-newton to pico-newton. To control the force or extension as per the requirement a user-friendly software has been written using LabVIEW. The software allows the user to select from the modes of operation: Constant Strain Mode and Constant Force Mode. The user-selected mode is implemented via a feedback-loop algorithm.

TABLE 1: Comparison of position detection devices

Device	spatial resolution (40x)	temporal Resolution	active area (40x)
Andor camera	$<$ 2nm	10hz	200μmx200μm
PSD	35nm	200Hz	120μmx120μm
QPD	$< 2nm$	1MHz	0.5μmx0.5μm

Chapter 3 - Dynamics of active suspensions

This chapter explains the experiments we performed using our device and other methods on active suspensions.

The dynamics of active matter is an important area in the interface of non-equilibrium statistical physics and hydrodynamics. While there are many examples of self propelled systems, bacterial baths are attractive model active systems owing to several advantages. The energy input is homogeneous, individual bacteria can be directly observed, bacterial cells are easy to culture and grow and critical parameters such as density, activity, and swimming behaviour can be brought under experimental control.

With the help of our device we introduce a new method to probe the active suspensions. There are definite advantages of using this device as compared using the techniques like optical tweezers. Experiments do not suffer from the issues like to local heating up of the sample and co-trapping of bacterial cells with beads.

We used three well characterized strains of E.coli RP-5232, RP-437 and RP-1616. RP-5232 is a predominant swimmer, RP-437 swims and tumbles (wild type) and RP-1616 is a predominant tumbler. All these strains are rod shaped cells and are nearly $2 - 3\mu$m long and close to 1μm in diameter. While RP-5232 has a typical swimming speed of 30-60 microns/sec, RP-1616 is characterised for the parameters like tumbling frequency ($1.8Hz$) and a mean tumble time (0.2s).

we performed two different types of experiments with these bacterial baths.

1. Cantilever based experiments, where the cantilever of suitable dimensions is immersed in the bacterial bath and deflections of the cantilever recorded and analysed for various parameters.

2. Particle tracking experiments, where fluorescent beads mixed in bacterial baths are tracked and analysed. These experiments were aimed at comparing the results of cantilever experiments wherever relevant in terms of numbers or trends.

These two types of experiments are completely different in nature and other than the sample (bacterial bath at a given density) there are no shared features. As we started with the motivation of determining the parameters like effective temperature due to bacterial activity, the choice of performing the experiments in the above two modes gives the estimate of the desired quantities independently and their agreement in values/trends stands as a robust test for the consistency in the results.

We started with looking at the influence of bacterial cells, at a known density, on the fluctuations of the cantilever. Figure (3.15) shows the distributions of the cantilever fluctuations in the medium without bacteria and medium with different strains of bacteria at a volume fraction of 8.4×10^{-4}. We see that the distributions of cantilever fluctuations in the control medium and the tumblers are gaussian, while that of wild type shows gaussian profile with exponentially falling tails. Distributions corresponding to cantilever fluctuations in swimmers exhibit large deviation from gaussian profile showing power law fall off with an exponent close to -1.5. The standard deviation of these distributions increases steadily from control to swimmers. Kurtosis, was found be close to 3 for control and tumblers, about 8 for the wild type and about 60 for the swimmers on the average.

The position distributions of the cantilever in the presence of tumblers showed a gaussian behaviour and the width of the distribution increased with increasing density. This observation indicates that the interaction of the tumblers with cantilever can be considered as stochastic gaussian noise. Therefore,we can define an 'effective temperature' which is a measure of bacterial activity. The effective temperature increased linearly with the density and is found close to two orders larger as compared to the room temperature. Then measured and compare the effective temperature of tumbling strain as a function of the density using both cantilever based experiments and particle tracking experiments. We see good agreement in the trend of variation of effective temperature with density from the two independent modes of experiments.

Chapter 4 - Extensional rheology at microscopic scale This chapter describes the devices utility as an extensional rheometer and the experiments we performed toward this end.

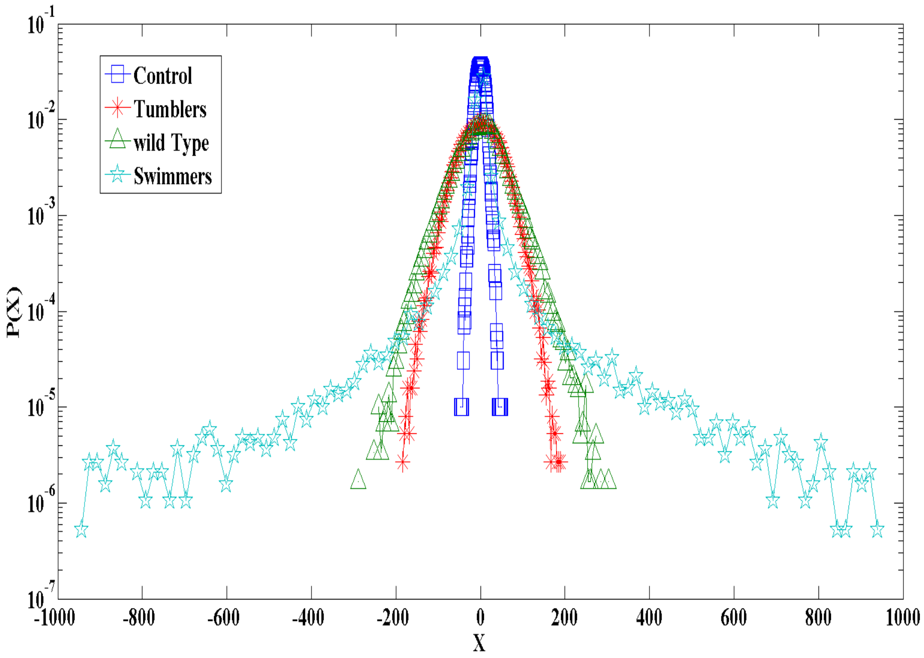

Figure 2: Distributions for the position data of cantilever in medium without bacteria and medium with different strains of bacteria at a volume fraction of 8.4×10^{-4}. We see that the distribution for plain medium and tumblers shows a gaussian while that of wild type shows distorted gaussian and that of swimmers exhibit large deviation from gaussian behaviour and the tails fall off with a power law close to -1.5. The standard deviation of these distributions increases steadily from control to swimmers.

Many real fluids in everyday life are subjected to extensional flows for various purposes and for some of these fluids there can be a very large difference between their shear and extensional viscosities and hence the knowledge of behaviour of materials under extensional flow is very important in many processes like fibre spinning, film blowing, etc. Some widely used methods for the study of materials such as polymer melts and solutions, under extensional flow, involve rheometers such as the Filament Stretching Extensional Rheometer (FiSER), the Capillary Breakup Extensional Rheometer (CaBER), etc.

In general the rheometer consists of two plates. Sample under probe is loaded between these plates and extension is imposed at known rate, in different modes such as exponential strain, step strain, etc. Usually extensional viscosity is calculated using two different methods. In one of the methods where force is a measured quantity, stress developed in the filament is calculated using force and mid filament radius data. The ratio of the stress and the imposed strain rate gives viscosity.

In the other method where force is not measured, mid filament radius data is obtained as a function of time. Using the values of surface tension and developing appropriate model, viscosity is computed.

All the existing extensional rheometers in the world probe the material properties at macroscopic scale. Extensional Rheometry at microscopic scales is an important application of our device. The sample requirement is just a few pico-litre and the filament lengths are of the order of few tens of micrometers. This feature can be very useful while characterising scarce or expensive liquids, especially biological fluids. Its facility of high resolution force measuring over a wide range is a major improvement over the other similar devices. Simultaneous imaging of the entire filament profile allows for particle tracking velocimetry and birefringence studies to measure stress or strain profiles in the samples.

We performed proof of principle experiments in various modes of rheometry using different plate geometries. We performed experiments imposing exponential strain and step strain on Newtonian and non-Newtonian samples at microscopic scale. The results of an experiment imposing a step strain on PDMS are shown in the figure wherein we measure the uni-axial extensional modulus of the material under probe. This experiment is also a demonstration of the feedback control we developed. We see discrepancy in the measured values of material parameters

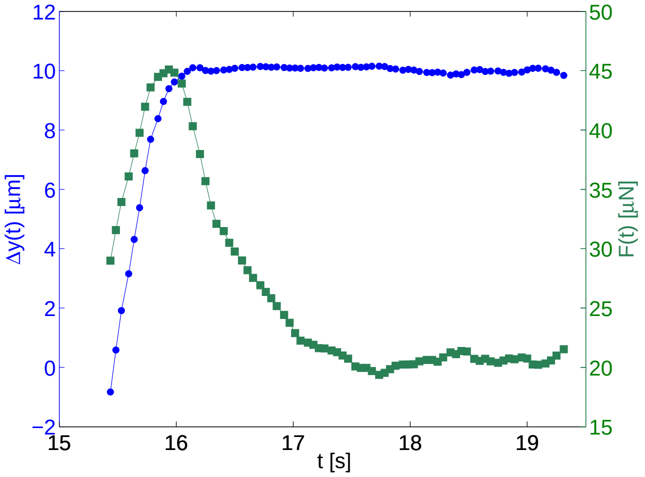

FIGURE 3: A plot of the extension $\Delta y(t)$ and the force $F(t)$ as a function of the elapsed time t, from a test with a commanded step of 25μm imposed on a polydimethylsiloxane (PDMS) filament with initial length $L_0 = 30.6\mu$m.

as compared the results of the existing rheometers. The discrepancies, between the results with our device and the other existing rheometers, can be broadly attributed to two effects.

1. In the filament stretching mode (FiSER) using an exponential strain profile, material properties are calculated ignoring the contribution of surface tension to the measured force and cylindrical profile is assumed for the filament evolution. In our case both these conditions need modification and suitable models are to be developed to account for surface effects as well as catenoidal filament evolution.

2. In capillary breakup mode experiments the constitutive models are based on calculating viscosity using surface tension, but assume uniform cylindrical evolution of the filament. In case of MER the filament being catenoidal we need modified models to account for the role of geometry.

On the experimental front, these problems may be overcome by measuring the entire filament profile in real time and an accurate estimate of the surface tension of the material under study. We show that both these measurements are indeed possible with our device. However, existing models have to be modified to take these effects into account, if one is to extract useful information from such measurements. Such an effort is in progress.

Summary

We developed a force device that can be used to probe a broad spectrum of science including mechano-biology, non equilibrium statistical physics and extensional rheology. After building and calibrating the device we performed experiments on active suspensions and extensional properties of fluids at microscopic scale.

Prof. Pramod A Pullarkat
Raman Research Institute

Seshagiri Rao R V

Publications

- Seshagiri Rao R. V.,Chiarg Kalelkar and Pramod A Pullarkat,
  ‘*Optical fiber based force transducer for microscale samples*’,
  Rev. Sci. Inst **84**, 105107(2013).

Contents

Chapter 1

Introduction

I am writing this introduction and motivation to my thesis work keeping Application of Force measurement to three disciplines of science in view, namely Mechano-Biology, Dynamics of active matter and Extensional Rheology.

Force plays a fundamental role in several physical as well as biological processes. Force measurement has been an important branch of sciences and engineering. A variety of force measurement techniques enabled powerful exploration of many areas of science including physics and biology.

With the advent of technology in the past few decades, force measurement at small scale gained pace. If we think about force techniques applicable in the force range of micro-newton to pico-newton or less, there are a variety of instruments catering to a broad range of applications. In this field some of the more widely used force spectroscopy devices include Atomic Force Microscopy (AFM) [1, 2] optical tweezers [3, 4] and magnetic tweezers [5–7]. Apart from these techniques, several methods such as pulling neurons using micro-needles [8, 9], live-cell rheology using micro-plates [10–12], stretching DNA using etched optical fibres [13] or using magnetic beads [14], Optical cell stretchers [15], micro-pipette based force transducers [16], MEMS-based force transducers [17, 18] etc., have been developed for specific applications in mechano-biology and other disciplines. Many of these devices allow independent control of the force or the tensile strain depending on the mode of measurement. Each of these techniques have their advantages and disadvantages, which depend on the problem under consideration and the ease of fabrication or commercial availability.

The power and breadth of these techniques are demonstrated by a large variety of measurements and systems probed. Current force manipulation capacity, considering the above mentioned techniques, spans six orders of magnitude in length scale of probing (10^{-8}m to 10^{-4}m) and in force (10^{-14}N to 10^{-8}N). Applications range from, tooling studies in metals, determination of nano particle structures, exploring various types of chemical bonding to several biological applications like unzipping DNA, studies on molecular motors etc.

In general, the application of force in biological systems provide a means to selectively modify the steps in a biochemical reaction cycle that involves motion. Detailed measurements of the force-extension relationships using these techniques enriched the research in the field of elasticity measurements of individual bio-polymers. Several experiments probing passive as well as active mechanics of single bio-polymers were reported. Elastic properties of DNA using magnetic tweezers [14], studies of Cytoskeletal elasticity using AFM [19], membrane tension studies using optical tweezers [20, 21], exploring protein binding and protein unfolding using AFM [22, 23] are some of the applications probing passive mechanics. Similarly transcriptional pausing by RNA polymerase [24],direct observation of base-pair stepping by RNA polymerase [25], measuring stall forces of molecular motors [26] using optical tweezers are a few examples of exploring active mechanics. In parallel with these developments, similar techniques were developed to mechanically rupture molecular bonds [27], energy landscapes in folding of nucleic acids [28]. Also force spectroscopy contributed to and benefited from the theoretical approaches that permit the extraction of detailed equilibrium thermodynamic parameters from inherently non-equilibrium pulling experiments [29–31].

Another emerging field that is employing sophisticated force measurement techniques is extensional rheology. Extensional properties of materials are important because extensional modes of deformation are obtained in a wide variety of industrial and laboratory settings, including tensile testing of materials, flow from an orifice, fibre-spinning of a thread, atomization involving breakup of liquid jets, flow through porous media, stagnation-point flows among others. In the field of extensional rheology [32–34], some widely used methods for the study of materials such as polymer melts and solutions involve devices such as the Filament Stretching Extensional Rheometer (FiSER) [35, 36], the Capillary Breakup Extensional Rheometer (CaBER) [37, 38], Meissner-type elongational Rheometer [39], Sentmanat Extensional Rheometer [40], etc. These devices operate at macroscopic scales and require large quantities of sample from about tenth of a milli-litre to few tens of milli-litres based on the application and device. Small-scale extensional Rheometers include the micro plate-based Rheometer [10–12], magnetic bead micro Rheometer [41], etc. Using these techniques material functions such as the uni axial extensional modulus and the uni-axial extensional viscosity of the specimen are calculated.

Dynamics of active matter, explored using statistical physics and hydrodynamics, is yet another area where force measurements at pico-scale can contribute to make it experimentally rich. Active complex fluid systems such as living cells [42–44] assemblies of molecular motors and filaments [45–47], flocks of birds [48, 49], and vibrated granular media [50] differ from conventional equilibrium media in that some of their components consume and dissipate energy, thereby creating a state that is far from equilibrium. An understanding of model active systems, even at a phenomenological level, provides insight about fundamental non-equilibrium statistical physics and, potentially, about the inner workings of biological systems. Bacterial baths [51–55] are attractive model active systems owing to various reasons. The energy input is homogeneous, individual bacteria can be directly observed, bacterial cells are easy to culture and grow and critical parameters such as density, activity, and swimming behaviour [51] can be brought under experimental control. Several experiments have been reported on a rich variety of non-equilibrium phenomena in this system class including anomalous diffusion [52, 53] and pattern formation [55, 56], while recent theories of self-propelled organisms predict ordered phases such as flocks [48], their instabilities [57], novel rheological effects [58], and giant density fluctuations [59, 60].

In the following sections I will give a basic description of different techniques discussed above, give a brief account of some calibration methods and then justify the need for a new force device to explore some of the problems in physics, engineering and biology.

1.1 An over view of different techniques

Several techniques in the field of force microscopy, extension rheology and active dynamics were mentioned above. As we already discussed, some of these techniques are widely used for a variety of applications, while some other are specific to a class of problems. In this section I will provide a brief over view of some of the force techniques and extensional Rheometers.

1.1.1 Atomic Force Microscope

Atomic Force Microscope (AFM) invented by Binning and Quate [1] as an improvement over scanning probe microscope later became a powerful tool to explore a wide range of samples at pico newton force resolution. AFMs operate by measuring force between a probe and the sample. Normally, the probe is a sharp tip, which is a 3-6 um tall pyramid with 15-40 nm end radius. As later development tips are available with different geometries. The vertical resolution of an AFM is typically up to 0.1 nm. To acquire the image resolution, AFMs generally measure the vertical deflections of the cantilever using the optical lever. The optical lever operates by reflecting a laser beam off the cantilever. The reflected laser beam strikes a position sensitive photo detector consisting of a quadrant photo-diode. The differences between the segments of photo-diode signals indicate the position of the laser spot on the detector and thus the angular deflections of the cantilever. The figure (1.1) below illustrates the working of an AFM.

AFM-based force spectroscopy has emerged as a powerful tool to study the rupture of molecular bonds, ranging from covalent bonds [61] to the unfolding of proteins [62] and nucleic acids [63]. Apart from being a single molecule force technique, AFM has several versatile applications. To name a few, tooling studies,

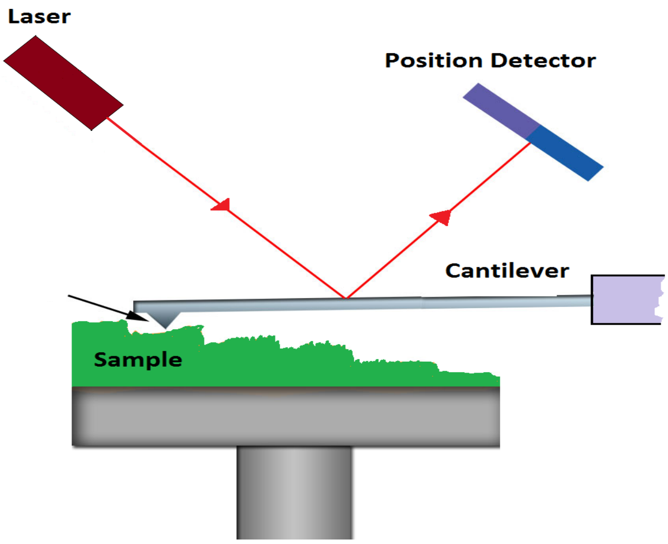

FIGURE 1.1: Schematic of AFM. The AFM tip deflects vertically and the laser light reflected from the cantilever illuminates the Position detector. Force is calculated using the measured deflection of the cantilever and calibrated spring constant.

roughness measurements, corrosion studies of metals, determination of morphology and surface properties, kinetic studies, ageing phenomena, surface treatment modifications, adhesion force measurement of polymers, nano- and micro-particle structures, Langmuir-Blodgett film studies etc [64–68].

1.1.2 Optical Tweezers

Optical Tweezers, developed by Arthur Ashkin and colleagues [3], operate based on the momentum transfer associated with the bending of light beams. Light carries momentum that is proportional to its energy and in the direction of propagation. Any change in the direction of light, by reflection or refraction, will result in a change of the momentum of the light. If an object bends the light, changing its momentum, conservation of momentum requires that the object must undergo an equal and opposite momentum change. This gives rise to a force acting on the object. A laser beam is focused by an objective to a spot in the specimen plane. This spot creates an optical trap which can hold a small particle at its centre. The forces felt by this particle consist of the light scattering and gradient forces due to the interaction of the particle with the light. The figure (1.2) below shows the working of optical tweezers.

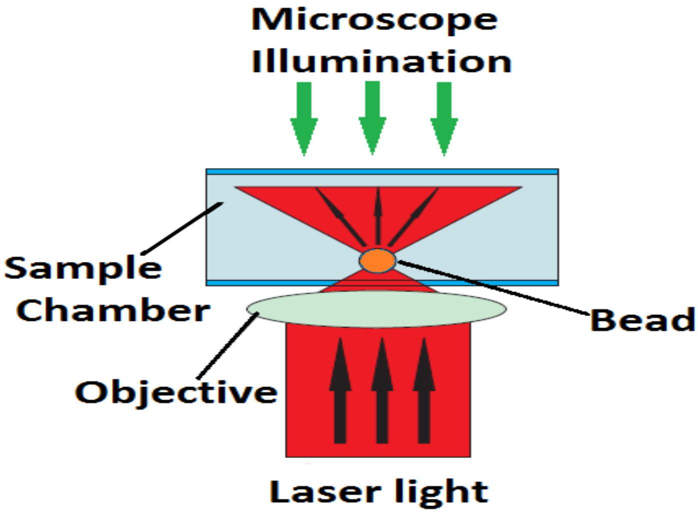

(a)

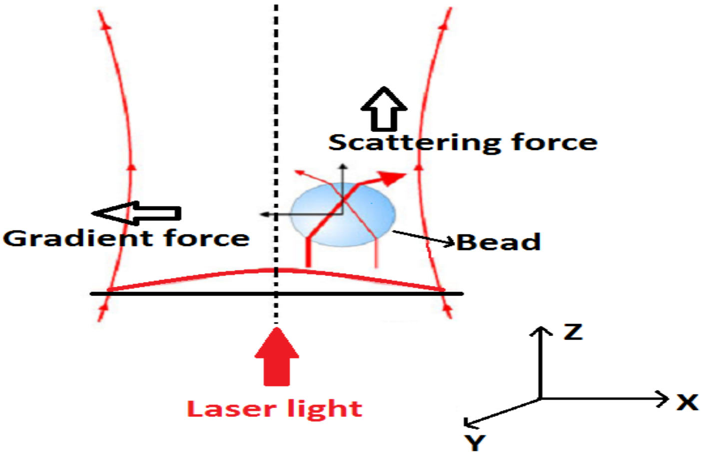

(b)

FIGURE 1.2: (a) Schematic of an optical trap for the inverted microscope configuration (b) Close up of the details of working area.When the laser rays interact with a bead, they show bending. The net force from all these rays show up in two components. (1) The scattering force along incident light (Z-direction here) and (2) The net gradient force pulls the bead towards the focal point. The final trap centre is decided by the balance of gravitational,scattering and gradient force. The bead deflection during force measurement is done using a QPD by imaging the scattered light on to it.

One major application of optical tweezers is to impose a specific interaction between the trapped bead and a fixed sample and to measure the force and displacement resulting from the interaction. In this class, there are reported experiments measuring the force and displacement of optically trapped kinesin-coated beads moving along fixed micro-tubules [69, 70]. In other similar applications, binding probability and unbinding force were measured for virus-coated beads brought into contact with erythrocytes [71] etc.

As yet another application, optical traps are used as force and displacement transducers of a probe that is attached to a substrate by the molecule/sample of interest. Examples for this types of application are, measurements of translocation and force generation of individual RNA polymerase molecules as they transcribe DNA. This single molecule assay has revealed details of transcription including the stall force [72] (about 30 pN), transcriptional pausing [73, 74], backtracking of the polymerase along the DNA template [75] and the mechanism of polymerase translocation [25].

1.1.3 Magnetic Tweezers

Magnetic tweezers [5, 6] work on the simple principle that a magnetic particle in an external magnetic field experiences a force proportional to the gradient of the square of the magnetic field. Magnetic traps consist of a pair of permanent magnets or an electro-magnet placed above the sample holder of an inverted microscope. Magnetic tweezers can be used to manipulate and rotate, magnetic particles ranging from 0.5 to 5μm. Mainly two types of magnetic particles are used as probes in this technique, the super para-magnetic particles and the ferro magnetic ones based on the application. While the super para-magnetic beads are used in most of the applications, ferro magnetic probes allow application of larger forces ($> nN$) and are used in generation of torques. As the magnetic field strength decreases nearly exponentially with a characteristic length scale comparable to the separation between the magnets. As a result the force on the probe remains nearly constant over the active distance. Due to this effect Magnetic tweezers can act as passive force clamps at large range of bandwidths over the working distances.

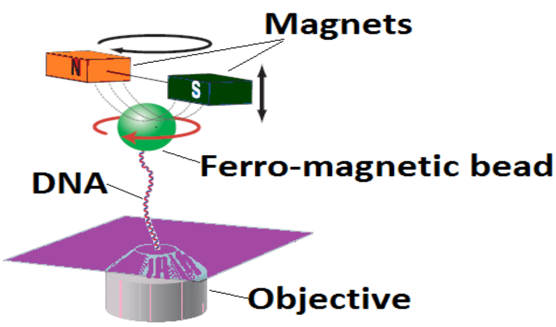

Figure 1.3: Schematic of a magnetic trap: A set of permanent magnet or an electro-magnet generates the field. The probe is a magnetic bead which comprises a latex matrix with magnetic nano-particles embedded in. The beads can be made of super para-magnetic material or ferro-magnetic material based on the applications. Often the beads are functionalized so that they can adhere to the sample molecules. The bead position is measured using video microscopy. Non-magnetic tracer particles are attached to the magnetic beads to make rotational measurements and hence torque.

Magnetic tweezers do not suffer from the problems of sample heating and photo damage as in optical tweezers, which enable non invasive force and displacement measurements in complex environments,such as the interior of cells [76] and within bio-polymer networks [77]. Permanent magnet configurations are relatively simple to assemble, and they combine force clamp properties with the ability to impose rotation. This combination makes magnetic tweezers ideally suited for the study of DNA topology and several related areas [78, 79].

1.1.4 Surface Force Apparatus(SFA)

The Surface Forces Apparatus (SFA) was developed, by Tabor, Winterton and lsraelachvili [80–82], for measuring van der Waals forces in air or vacuum. Later, the instrument was adapted for measuring forces in liquids. This device measures intermolecular potentials by direct force measurement. A schematic of the SFA is shown in figure (1.4). Two thin sheets of atomically smooth mica are approached in crossed cylinder geometry. The curvature of each surface is achieved by gluing the mica sheets onto an optically polished cylinder lens. One of the surfaces is connected to the SFA frame via a force measuring spring with the spring constant k. The deflection of this spring is obtained indirectly using Multiple Beam Interferometry to measure the separation between the surfaces, D, while the approach mechanism, M, is changing the total size, S, of the mechanical loop.

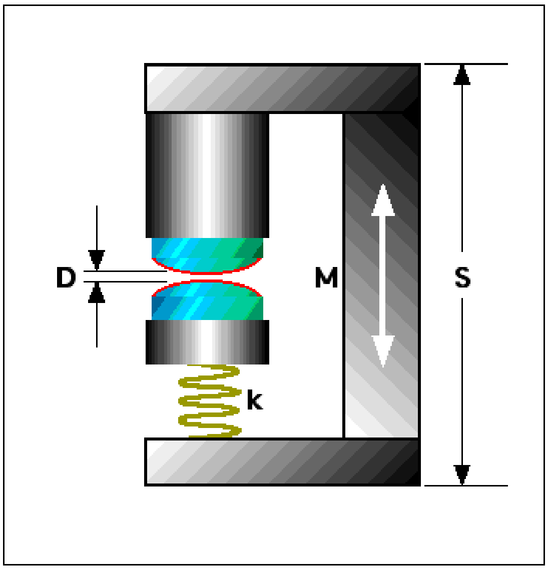

FIGURE 1.4: Schematic of SFA: The deflection of the spring with stiffness k is obtained with Multiple Beam Interferometry to measure the separation between the surfaces, D, while the approach mechanism, M, is changing the total size, S, of the mechanical loop.

1.1.5 Micro-needle technique

Glass micro-needles were used to apply forces on cells and the basic technique is similar to that of MER. In fact using an optical fibre as a cantilever is an improvisation over this technique. This is a simple technique, where flexible, calibrated, glass micro-needles were used to apply forces on cells to explore the mechanical properties of these cells [83–85]. The micro-needle technique is of good use in case of pulling on cylindrically symmetric objects and has been effectively applied to probe mechanical properties of axons, where the axons can be stretched at different strain rates or can be subjected to step strains and the force relaxation can be observed [8, 9, 83, 86]. In case micro-needles no laser is used and deflections of the needle as well as extension produced in the cells have to be measured by optical microscopy. Due to this limitation the controlled force or extension measurements are difficult to perform and also precision in position determination is low. Measured forces in these experiments were few nano-newton and extensions of few microns to few tens of microns. figure (1.5) shows the working of the micro-needle based force setup.

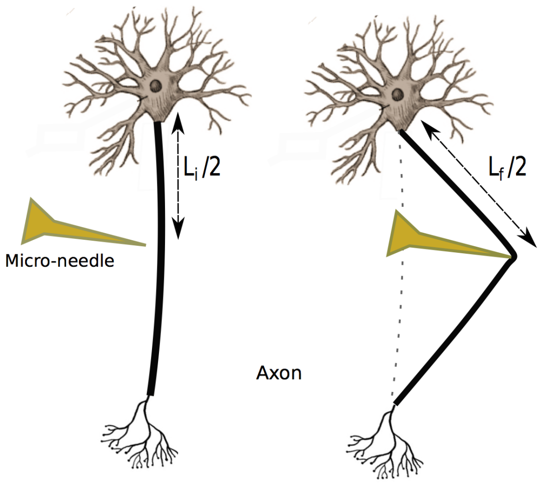

FIGURE 1.5: The cell which is nearly cylindrical in geometry is pulled laterally by a calibrated glass micro-needle. The deflection of the needle along with its spring constant gives force. Extension produced in the sample is calculated by the difference in the initial and final lengths of the sample. In this case video microscopy is used to determine both the deflection of the needle and the extension in the sample.

1.1.6 Micro plates

This is one of the techniques used to pull on single live cells [10–12] by attaching the cell between two functionalized glass micro plates. One of the plates is rigid and the other which is flexible acts as a force transducer. The cell can be uni-axially stretched by moving the rigid plate with the help of a piezo actuator. The figure (1.6) shows the schematic of this technique. Using a feedback mechanism strain or force can be controlled independently. Using this device forces can be applied in the range of 10nN to 10μN and accuracy in plate deflection measurement is about 50nm.

This technique is suitable to perform various rheological measurements such as relaxation response to step strain, creep response to a step force and oscillatory mechanical excitations on living cells.

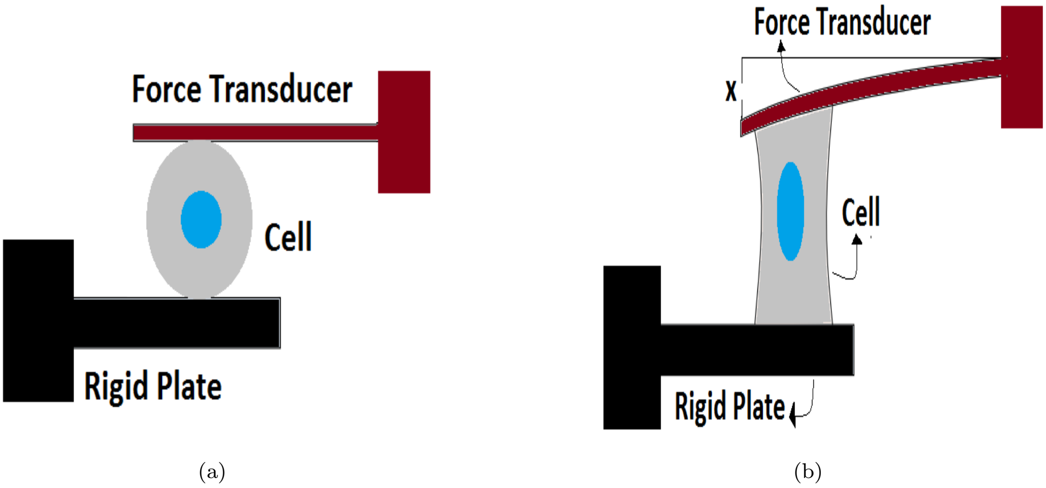

(a)

(b)

Figure 1.6: (a) Schematic of Micro plate based force transducer. A cell is sandwiched between two specially fabricated glass micro-plates of which one is rigid and the other acts as force transducer (b) The deflection x of the flexible calibrated plate (transducer) is the measure of applied force. The deflection is measured by scattering laser light from the tip of the flexible plate or by putting it in contact with a higly flexible optical fibre.

1.1.7 Optical cell stretcher

The optical stretcher developed by Kas and group [15] is a laser based tool that can trap and deform individual biological cells. The momentum transfer of light to the opposing surface causes the stretching force. The cell deformation can be measured by optical microscopy and analysis.

The deformations can be used to understand the cell cytoskeleton that resists the external forces. Changes in the cytoskeletal geometry indicate pathological changes and can be detected with the optical stretcher. Viscoelastic properties of cells can be explored by applying step stresses and measuring the resultant relaxation [87].

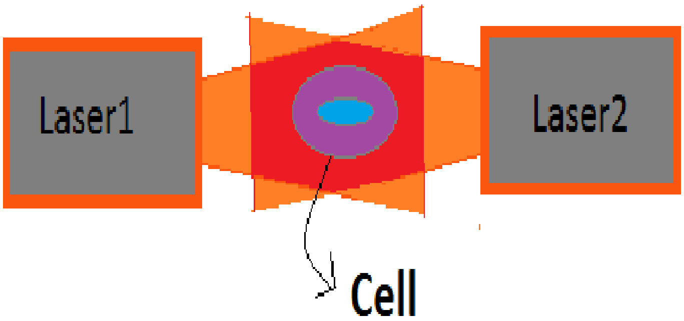

Figure 1.7: The momentum transfer of light to the opposing surface stretches the biological cell. The cell deformation is measured by video microscopy and analysis.

1.2 Extension Rheometers

1.2.1 Filament Stretching Extension Rheometer (FiSER)

The filament stretching extensional Rheometer (FiSER), developed by Sridhar and co workers [35, 36], has been designed to induce a true uni-axial extensional flow on polymer solutions. Sample polymer is placed between two plates and a set of linear motors drive one of the end plates at an exponentially increasing velocity, while measuring force on the other plate and diameter of the fluid filament as a function of time and position. For uni-axial extension of a filament, the length of the filament varies with time as

$$L(t) = L_0 exp(\dot{\epsilon} t) \tag{1.1}$$

where l_0 is the initial length of the filament and $\dot{\epsilon}$ is the strain rate. Therefore by imposing an exponentially increasing velocity profile, a constant strain rate can be achieved in the samples, barring end plate flow limitations.

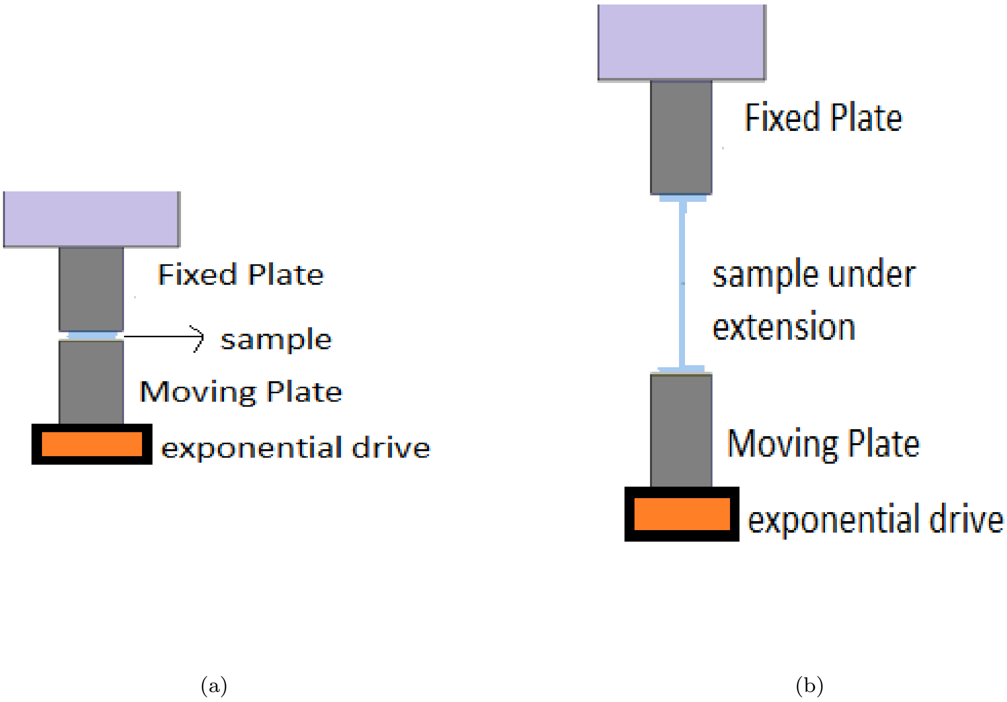

(a) (b)

FIGURE 1.8: (a) Schematic of FiSER. (b) Polymer sample under extension using FiSER: sample is loaded between the two end plates and one of the plates is subjected to exponential velocity profile. The fixed plate acts as force transducer. Extensional viscosity of the sample is calculated from the profiles of force and mid diameter of the filament measured by laser a micrometer.

For visco-elastic fluids such as polymer melts and solutions, the transient uni-axial extensional viscosity as a function of both the rate of stretching and the total deformation can be measured with FiSER. Knowledge of the resulting material function is of great importance in governing the dynamics and stability of polymer processing operations such as fibre-spinning, film-blowing and blow moulding.

1.2.2 Capillary Breakup Extensional Rheometer (CaBER)

In CaBER [37, 38] a polymer sample is placed between two plates similar to that in FiSER but a step strain profile is imposed on one of the end plates, keeping the other end plate fixed. The fluid under consideration evolves due to surface forces and only its mid-filament diameter is monitored using a laser micro meter. Visco-elastic properties of the fluid are characterized based on developed models.

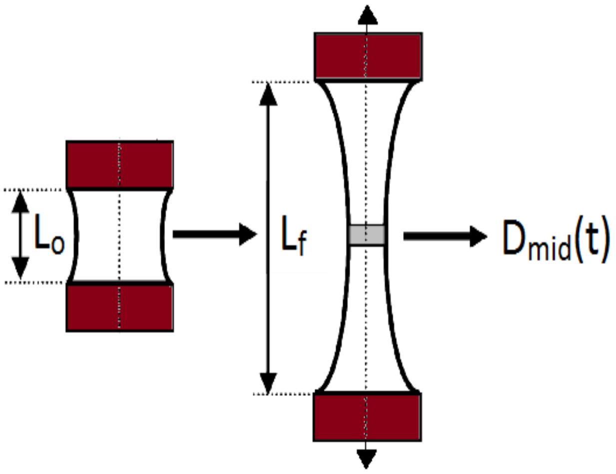

FIGURE 1.9: Schematic of CaBER: After placing the sample a step strain profile is imposed on the movable plate and mid filament diameter is monitored. Extension viscosity is calculated as a model based parameter

1.3 Standard calibration methods

Calibration of any instrument forms a very important part of its application. In this section I will discuss few standard calibration methods applicable to some of the above discussed instruments. Devices like optical tweezers are usually calibrated for trap stiffness or maximum force using the techniques such as viscous drag method and measuring Brownian motion etc. A widely used method for cantilever calibrations is measuring the resonant frequency and relating it to the spring constant via bending modulus. If the cantilever geometry is non-cylindrical, then this method can bring in considerable amount of complication in calibration. For example the AFM cantilevers need specialized techniques and model based calibration methods mainly due the probe geometry as mentioned above.

1.3.1 Measuring Brownian motion

This method of calibration is ideal for the devices like optical tweezers. Position of the probe (trapped bead) is recorded as a function of time and the power spectrum of this time series data is used to determine the stiffness of the trap.

When a particle is not confined nor trapped, its motion is driven by random, uncorrelated Brownian forces $F(t)$ which have an average value of zero, and a power spectrum which is constant for all values of the frequency f (white noise). If the particle is trapped, then its motion in one dimension may be modelled as a damped, driven harmonic oscillator, that is to say that the restoring force is a linear function of displacement. The motion of the particle of radius a in a solvent of viscosity η can be represented by the Langevin equation. The fluid in which the particle is suspended, has a Stokes drag coefficient $\gamma_0 = 6\pi\eta a$ which opposes the motion.

$$m\ddot{x}(t) - \gamma_0\dot{x}(t) + kx(t) = F(t) \tag{1.2}$$

In the over damped condition the inertial term is dropped and remaining part is solved using Fourier transformation from time to frequency domain.

$$x(t) = Z^{-1}[X(f)] = \int_{-\infty}^{\infty} X(f)e^{-2\pi fit}\,df \tag{1.3}$$

The Langevin equation without inertial term in the frequency domain becomes,

$$(f_c - if)X(f) = \frac{F(f)}{2\pi\gamma_0} \tag{1.4}$$

where f_c is the characteristic corner frequency of the trap/spring given by,

$$f_c = k/2\pi\gamma_0 \tag{1.5}$$

This complex function can be simplified by squaring its modulus and we can express the particle's motion in terms of a power spectrum.

$$4\pi^2\gamma_0^2(f_{c^2} + f^2)S_x(f) = S_F(f) \tag{1.6}$$

the power spectrum of the transformed Brownian force $F(f)$ has a constant value across all frequencies, $F(f) = 4\gamma_0 k_b T$. Solutions to the eq (1.6) give Lorentzian distribution in the form of

$$S_x(f) = \frac{k_b T}{\gamma_0 \pi^2 (f_c^2 + f^2)} \tag{1.7}$$

This gives the frequency dependence of fluctuations, or the power spectrum, of the position (in case of optical trap position of the bead). An example of an ideal power spectrum is shown in Figure (1.10)). The position fluctuations are approximately constant at low frequencies until f_c is reached, at which point the slope of the power spectrum changes significantly. Conceptually, the particle in the trap experiences free diffusion over shorter time scales (i.e. high frequency,$f > fc$) but is bound by the potential at low frequencies. The corner frequency delineates the two regimes. Thus, measurement of the fluctuations in the position of a bead in a trap due to Brownian motion can be used to determine f_c. Therefore, this is a measurement of the trap stiffness, k, which allows us to determine the force on a bead in the trap directly from its change in position.

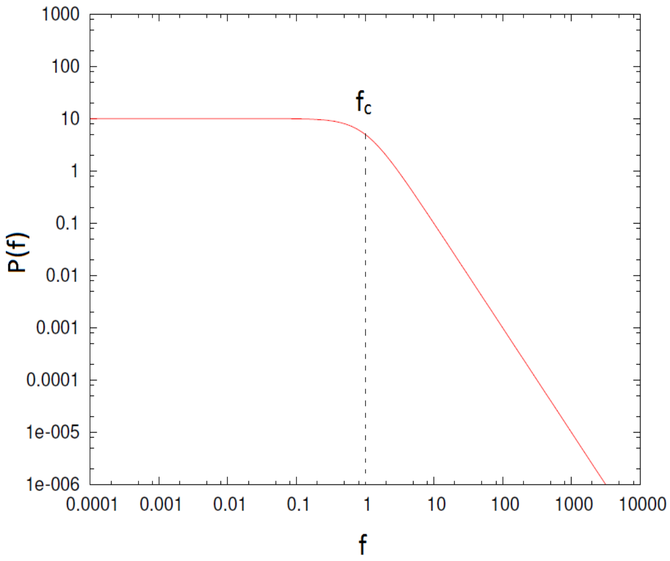

Figure 1.10: An ideal power spectrum for the position of a bead in optical trap. The corner frequency separates the potentially bound region from the free diffusion region

1.3.2 Calibration by resonance

This method is better suited for cantilever based force devices. The cantilever is excited, using an external source like a function generator, at different frequencies to determine the resonant frequency. This frequency is a function of the properties of the cantilever material and the cantilever geometry and hence the stiffness or spring constant of the cantilever. If we consider a slender $(d << l)$ cylindrical cantilever with length l, cross sectional area S, area inertia I, Young's modulus E and density ρ, we get

$$\omega_0 = \frac{b}{l^2}\sqrt{\frac{EI}{\rho S}} \tag{1.8}$$

the value of b comes out of the boundary conditions such as free,hinged and clamped states of cantilever [88]. if the geometry varies from that of a cylinder, necessary coefficients are to be included based on the requirement, but the form of dependence remains the same. Now if we calculate I and S and assume constant values for E and ρ, then the relation becomes

$$\omega_0 \propto \frac{d}{l^2}. \tag{1.9}$$

where d is the diameter. Then one can calculate the spring constant of the cantilever from the already determined parameters. For cylindrical cantilevers the spring constant k depends on the length and the diameter of the cantilever as

$$k \propto \frac{d^4}{l^3}. \tag{1.10}$$

. In case of the devices like AFM this method is more accurate keeping the error within $5 - 10\%$ [89].

1.3.3 Other methods

There are some other notable improvised methods to calibrate AFM cantilevers. One technique developed by Sader and co-workers, uses resonant frequency and quality factor of the cantilever in the known fluid and the plan view dimensions of the cantilever [90].

Another method developed by Hutter and Bechhoefer uses thermal method and the quality factor of the cantilever to obtain spring constant. This method is simple and does not require additional hardware. Also the error is claimed be within 5% [91].

Butt and Jaschke proposed thermal noise based calibration procedure Calculating the contributions of several modes of vibration, cantilever geometry and offered a comprehensive method of cantilever calibration [92]

Some more commonly used methods to calibrate AFM cantilevers are, method of added masses by Cleaveland et al [93], comparison with a reference cantilever of known stiffness etc. A comparative analysis of some of the important techniques related to AFM cantilevers is described by Burnham et al [94].

Magnetic tweezers are usually calibrated for position using thermal vibrations method and drag force method [95].

1.4 Need for a new device

While a variety of instruments and techniques are available in the field of force measurement and extension rheology there are areas, where novel methods of force application are in demand. Considering the biological cells like neurons a device which can pull on axons while performing simultaneous microscopy can facilitate understanding their mechanical properties. The active and visco-elastic properties of axons are considered to be important in axonal retraction after injury or during rewiring and in stretching during limb movement. There are reported experiments pulling on axons using micro-needles [8, 9].

We wanted to improve upon the micro-needle technique and build a better device to probe axons and other similar cells to begin with. As a major part of my thesis work, We developed a cantilever based force transducer [96], which has pico-newton resolution in force and a few nano-meter in position. It has demonstrated capabilities to probe some of the problems already mentioned in the areas of mechano-biology, extension rheology and active matter dynamics. We used the setup to pull on axons, form micro-scale filaments from synthetic polymers and study the dynamics of E.coli. While the experiments on extensional rheology of polymers were performed at milli-newton and micro-newton scales, the axon pulling experiments pertained to nano-newton and studies on E.coli involved pico-scale forces. In summary the capability of the instrument covers a wide range in force measurement from the order of a milli-newton to that of a pico-newton. The device on one hand shares the features with single molecule force spectroscopy techniques like AFM, Optical Tweezers and Magnetic tweezers and on the other hand it works as an extension Rheometer like FiSER, CaBER etc. The detailed comparison of our device with other discussed techniques is provided in the discussion section of instrumentation chapter.

Chapter 2

Instrumentation

2.1 Introduction

In this chapter we will discuss the development of the force measurement set up we built in our lab and named Micro Extension Rheometer (MER). There were reported experiments exploring mechanical properties of axons using micro needles [8, 9]. We wanted to build a better and versatile device to probe neurons and similar soft and biological systems, where cantilever based force transducers are useful. Also we wanted the setup to be capable of controlling force or extension independently, which can be achieved via feedback mechanisms. As the device became a reality, we found several potential areas where force transduction using our instrument is applicable and went on to explore some of them. In the following sections we present the description of the setup, its configurations based on applications, and then go ahead to explain the calibration process of various components of the device in detail.

2.2 Setup description and components

2.2.1 Basic operating principle

We developed the Micro-Extensional Rheometer (MER) which uses an etched optical fibre as a force-sensing cantilever. A schematic diagram of the MER set up in different configurations is shown in Figures (2.1) and (2.2). The corresponding working area are shown in figures(2.3) and (2.4). The working area comprises a piezoelectric transducer and an optical fibre coupled to a laser, placed above the objective of a microscope. A cylindrical portion of the optical fibre acts as the cantilever for force sensing. The length and diameter of the cantilever can be adjusted to achieve the desired force sensitivity. The tip of the cantilever is seen as a bright spot through the microscope when laser light is coupled into the fibre. A Position-Sensitive Detector (PSD) is used to track its motion or deflection. To study the extensional rheological properties of polymers, a few pico litre-volume of the sample is placed within the gap between the tip of the cantilever and the end of a syringe needle (or any other suitable material of appropriate dimensions) attached to the piezo, as shown in Fig (2.4). In another set of experiments where the setup is used to pull on axons, the cantilever was mounted on piezo actuator as shown in fig (2.3) and force is applied on axons in transverse direction where the two ends of the axon are fixed. A lamp within the microscope is used to illuminate the sample through a condenser using green light, and images are recorded by a camera mounted on a side port of the microscope. Appropriate filters are used in front of the camera and the PSD to separate the green illumination light and the red laser light. The PSD reading and piezo control are obtained using a home developed LabVIEW code. A feedback mechanism is developed using LabVIEW in order to control force or extension. Recorded images are analysed using a home developed MATLAB code.

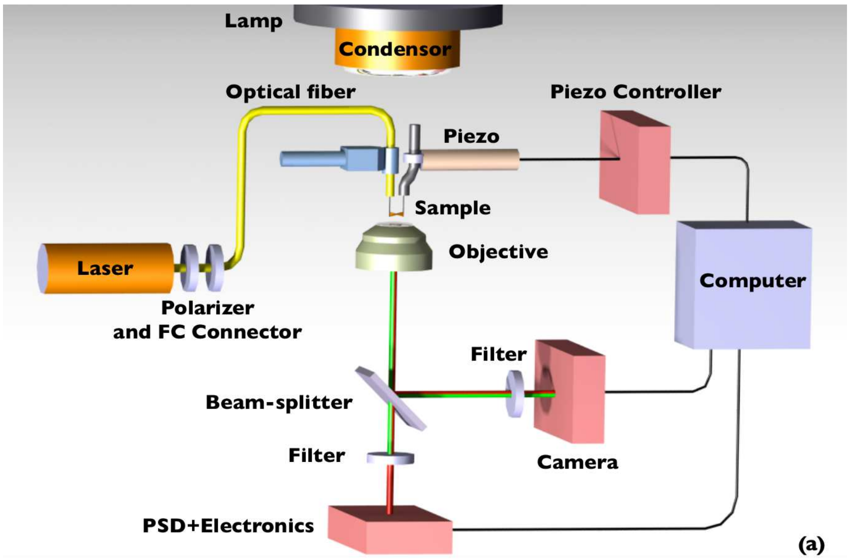

FIGURE 2.1: Schematic of MER for polymer rheology experiments. Laser light coming out of the calibrated cantilever is focused on to a PSD which tracks the position of tip of the cantilever. Sample is loaded between this cantilever and the other rigid rod and the rod is pulled using a piezo producing an axial extension in the sample. The sample evolution is imaged on the CCD camera using green microscope illumination

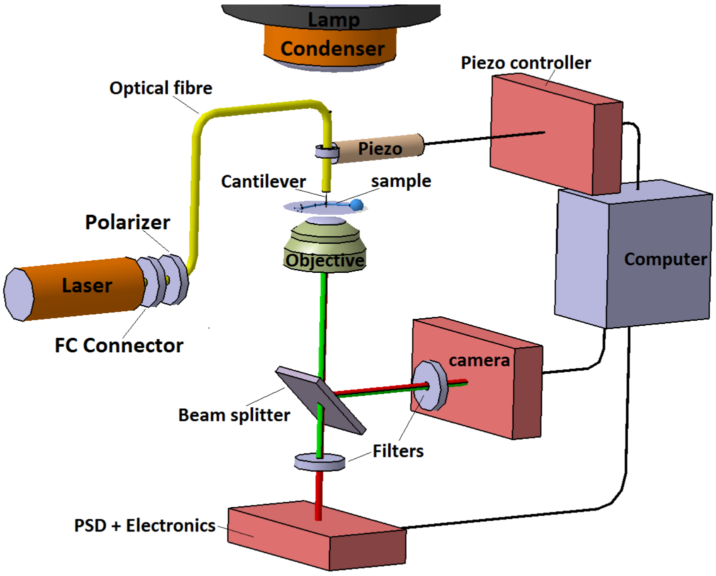

FIGURE 2.2: Schematic of MER, for transverse pulling experiments. Laser light coming out of the calibrated cantilever is focused on to a CCD camera and a PSD which track the position of tip of the cantilever. Cantilever tip is attached to the cell and is pulled using a piezo, normal to the cylindrical axis of the cell.

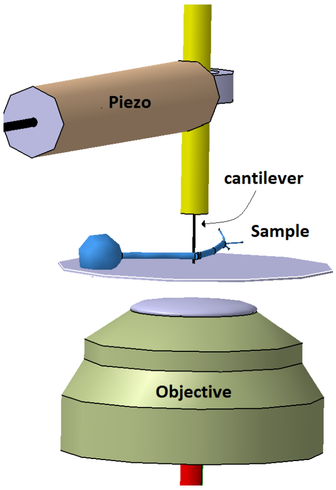

Figure 2.3: Schematic showing the close up of working area of neuron pulling setup. The axon is fixed at the two ends and is pulled by the cantilever normal to the axis of the axon.

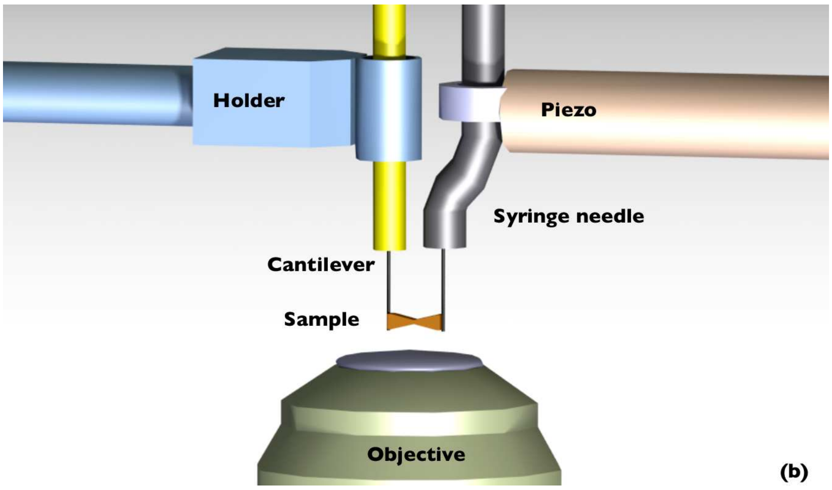

Figure 2.4: Schematic showing close up of working area for extension rheology experiments. The sample is loaded between the cantilever and another rigid rod. The rigid rod is mounted on the piezo. The piezo drives the rigid rod and the sample undergoes axial extension.

2.2.2 Technical details of MER

The setup was mounted on a vibration-isolation table (VH3648W-OPT, Newport Corp., United States). A 17mW, polarized, TEM_{00} He-Ne laser (25-LHR-925, CVI Melles-Griot, United States) with a beam diameter of 0.96mm, operating at an output wavelength of 633nm was used. The laser intensity was controlled by a linear polariser (46575, Edmund Optics, Singapore). The laser light was coupled to the optical fibre using an FC connector (F240FC-B, Thorlabs Inc.,

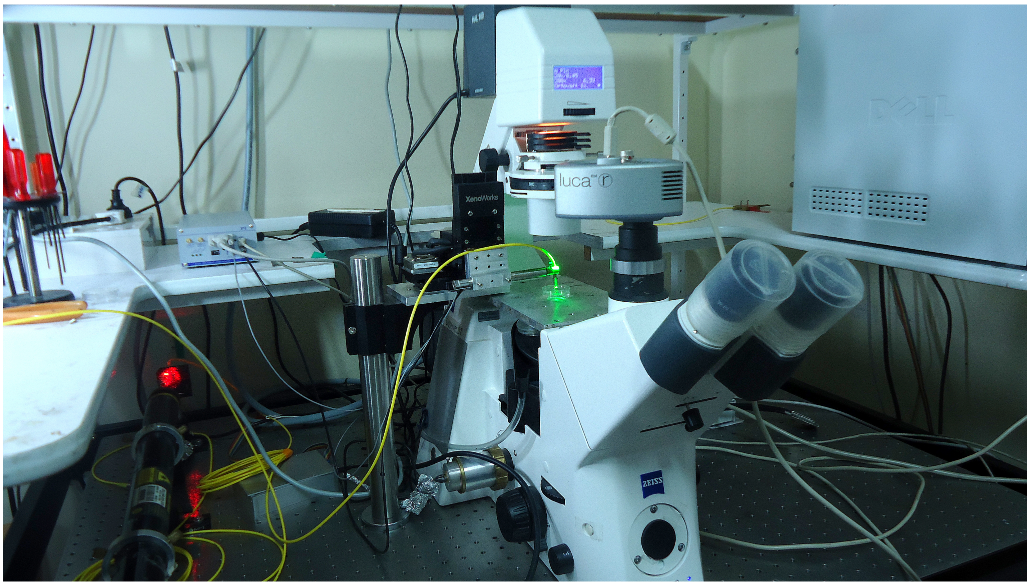

FIGURE 2.5: Photograph of the setup

United States). The single-mode optical fibre (P1-630A-FC, Thorlabs Inc., United States) used has a core of diameter 4.3μm made of germanium-doped silica for a design wavelength of 633nm, and a cladding of diameter $125 \pm 1\mu$m made of silica. The tip of the cantilever as well as the sample were imaged using a microscope (Zeiss Observer.D1, Carl Zeiss GmbH, Germany). The sample was illuminated by green light using an interference filter placed above the microscope condenser. A beam-splitter sends 20% of the incident light to a side port mounted with a CCD camera (Andor Luca R604, Andor Technology, Ireland). A red-absorption filter was placed in front of the camera to attenuate the intensity of the laser light incident on it, while allowing the scattered light (green) due to the sample to pass almost unhindered. In this method both the laser spot (tip of the cantilever) and the sample can be imaged simultaneously. The CCD camera has a resolution of 1004(H)×1002(V) pixels, a pixel size of $(8 \times 8)\mu\text{m}^2$ and a frame rate of 12.4 Hz. For some of the applications, mainly in case of experiments on extension rheology of polymer melts, a high-speed camera (MotionPro Y4, Integrated Design Tools Inc., United States) is available as an option. Using camera was the simplest mode of position determination, although real time force readout was not possible in this method.

As another mode of position detection, we used a pin-cushion type two-dimensional

PSD (S2044, Hamamatsu Photonics, Japan) with an active area of $(4.7 \times 4.7)\text{mm}^2$. The operating principle is explained in the calibration section ahead. The PSD was mounted with the detector surface coinciding with the image plane of the side port of the microscope which collects 80% of the light incident on the objective. A narrow bandpass interference filter (FL632.8-10, Thorlabs Inc., USA) placed in front of the detector allows only the laser light to be incident on the PSD. The PSD signal processing circuit (C9069, Hamamatsu Photonics, Japan) calculates the position of the light spot using a standard sum and difference module (details in appendix A), performs A/D conversion and sends digital output at 200Hz through a RS-232 interface to a computer. The PSD gives as output, the signal position and the incident light level in 12-bit hexadecimal format. A home built LabVIEW (Ver. 11, National Instruments, United States) code was used to record the PSD output and convert from hexadecimal to decimal. This code was tested against the application software of the PSD (Ver 1.1, Hamamatsu Photonics, Japan).

The third option we had for position sensing was employing a Quadrant Photo-Diode (QPD) (QD-50-0, OSI Opto electronics, United States). QPD was mounted on a side port of the microscope. Output from QPD was fed into a 16-bit Data-Acquisition Card (PXIe-6363, National Instruments, United States). This device has a limited spatial range of about a micrometer, but offers superior temporal resolution with a sampling rate up to 2MHz and a spatial resolution of about 2 nm.

The piezo actuator (P-841.60, Physik Instruments GmbH, Germany) used for applying displacements has a 90μm travel range, and comes with a single-axis piezo servo-controller (E-625.SR) having 24-bit A/D and 20-bit D/A resolutions. The piezo is equipped with a strain gauge, which acts as a feedback to the controller, in order to overcome hysteresis effects. The piezo can be operated in an open loop mode without employing strain gauge or in a closed loop mode, where the strain gauge is functional. The actuator can sustain a pushing force up to 1000N and a pulling force up to 50N. The piezo is controlled using a LabVIEW code via a serial-port interface. Prior to use, zero-point adjustment of the piezo servo-controller was carried out, as described in the manual and the LabVIEW-control tested against the vendor application software MikroMove (Ver. 2.4.06, Physik Instruments GmbH, Germany).

A feedback algorithm was implemented in the LabVIEW code to perform controlled force or controlled strain tests (see section on feed back for details). The optical fibre and the piezo were mounted on the microscope stage using two separate sets of three-axis translation stages with micrometer precision from Thorlabs Inc. (United States) and Holmarc Opto-Mechatronics Pvt. Ltd. (India). An aluminium box is used to enclose the parts mounted on the microscope stage to minimize disturbances due to air currents.

Important components of setup:

1. Vibration isolation table

2. Laser source and accessories

3. Optical fibre

4. Inverted microscope and related optics

5. Position sensitive detector

6. CCD camera

7. Piezo electric actuator

8. Quadrant photo diode

The Detailed specifications of above components are given in appendix A.

2.3 Setup configurations

As already mentioned, we tried three different types of applications using the device. In this section we will explain the specific configuration of the setup in these experiments and accordingly define the measurable parameters. In the force application experiments based on whether the force is applied transversely or longitudinally with respect to the sample the configuration changes. In any configuration where force is applied, it is to be noted that the sum of deflection of the cantilever d and extension produced in the sample x amount to the piezo actuator displacement D as shown in figures (2.6) and (2.7. The two measured quantities are the piezo displacement D, read as the strain gauge output and the PSD reading, tracking the light spot.

2.3.1 Setup for Neuron pulling experiments

The sample (axon) is a part of a neuronal cell which is nearly cylindrical in geometry and is fixed at the two ends. The cantilever is mounted on the piezo, brought into contact of the cell close to its midpoint and is pulled normal to the length of the initial cylindrical axis as shown in figure (2.3).

Looking at the schematic given by figure (2.6) we can find that the extension in the sample x is given by the difference in PSD reading. The deflection d in cantilever comes from the subtraction of Piezo displacement D and x. In this mode we read D from strain gauge output and x from PSD. Multiplying the spring constant k to d we get the force as $F = -kd$.

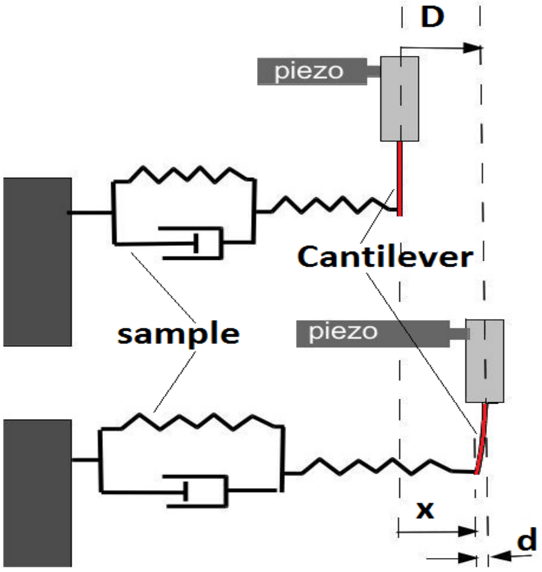

FIGURE 2.6: Schematic showing deflection of cantilever and extension in the sample when cantilever is sitting on the piezo.

2.3.2 Extensional rheology experiments

As already discussed in the previous chapter extensional properties of materials are of great importance a large variety of industrial and laboratory applications, including tensile testing of materials, flow from an orifice, fibre-spinning of a thread, atomization involving breakup of liquid jets etc.

The sample is loaded between the cantilever and another rigid cylinder, while this rigid cylinder is mounted on the piezo actuator. Suitable strain (exponential/step) is commanded to piezo using a LabVIEW code. When displacement is commanded to piezo, the rigid rod pulls a filament out of the polymer and the cantilever sitting on the other end of the sample shows deflection, which is the measure of force experienced by the cantilever. In this case, the cantilever deflection d is given by the difference in PSD reading of initial (before pull) and final (after pull) positions. The extension is calculated as $x = D - d$, which is the difference of Piezo displacement and PSD reading as shown in figure(2.7).

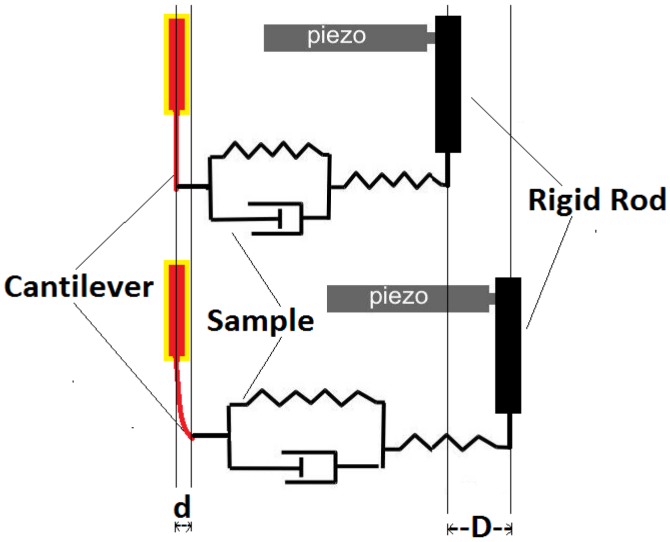

FIGURE 2.7: Schematic showing deflection of the cantilever and extension in the sample when the sample is loaded between the cantilever and another rigid rod. The rigid rod is mounted on the piezo actuator.

2.3.3 Passive configuration: Force sensing

In the experiments, where active systems like bacteria are probed, the configuration is simple. There is no piezo actuator in this mode as there is no force application. Cantilever was mounted on a translation stage and was immersed in the bath, usually a cylindrical container, with bacterial solution (See fig. (3.1)). The diameter of the container is kept small and a drop of mineral oil is placed on top of the liquid so as to minimise the effects of convection. A QPD was used to record the cantilever fluctuation ata faster rate of about $100kHz$. For some of the required experiments and video microscopy a CCD camera was used.

2.4 Preparation of cantilevers

Optical fibre cantilevers are easy to fabricate and do not require specialized equipment for manufacture and hence provide cost and time advantages. More importantly, the cylindrical geometry of the cantilever allows for quick and precise calibration [92]. For calibration tests as well as several experiments, we used optical fibres with etched as well as un etched tips (see Figs.2.9 (a) and 2.9 (b)). To etch the optical fibres the following protocol was followed.

2.4.1 Etching Process

Based on the requirement, a definite length of the fibre was chosen. Outer Plastic sheath was taken out using scalpel/scissors and the next layers of plastic coating was removed by exposing the cable to flame. Then what remained was the glass part of the optical fibre. The required length of the fibre was dipped into freshly prepared solutions of Hydrofluoric Acid (HF, Merck, India). For example, to obtain an etched fibre with a diameter $\sim 10\mu$m, the following concentrations of HF were used in the sequence: 48% for 30 minutes, 25% for 25 minutes and 15% for 15 minutes, followed by a rinse with de-ionised water. The acid is gently stirred using a magnetic stirrer during the etching process. The time required for etching

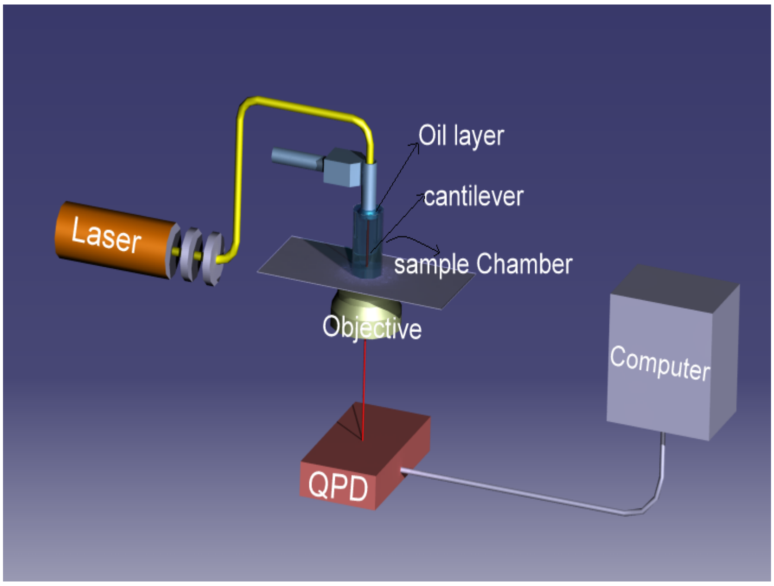

(a)

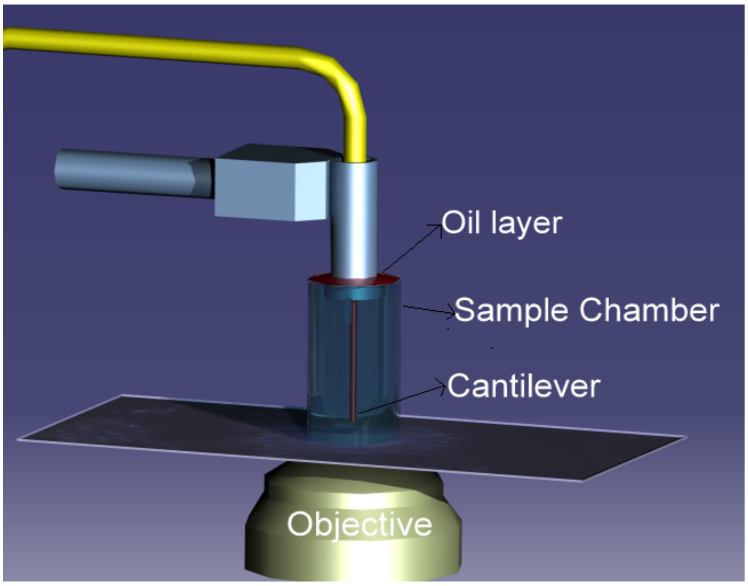

(b)

FIGURE 2.8: (a) Schematic showing setup for force sensing.The cylindrical container is filled with the bacterial solution and an etched fibre acting as cantilever is immersed in the bath. The effect of bacterial activity reflected in terms of cantilever deflection can be tracked by a QPD. Narrow tube and placing a drop of oil on top of the liquid help minimising convection. (b) Zoomed in version of working area

the fibre varied with the required diameter and the age of the hydrogen fluoride solution used. All the etching process employing HF was carried out under a chemical safety hood with appropriate personal protection following the standard HF handling protocol.

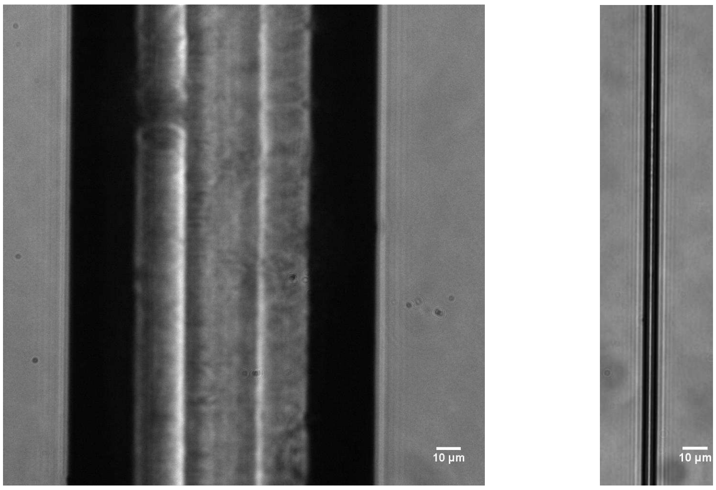

(a) (b)

FIGURE 2.9: (a) Image of an un-etched cantilever with a diameter of 125μm. (b) The etched part of the cantilever of nearly 8μm diameter. Scale bar in both the figures is 10μm

This method produces nearly uniform cylindrical cantilevers with a taper which is less than 1μm over a length of 15mm. After etching, the tip is cut using a scalpel to obtain a nearly circular aperture (confirmed by observing the profile of the emergent light). The length of the fibre is measured under a stereo-microscope using a Vernier calliper with a least count of 20μm and the diameter is measured using the microscope and the CCD camera, with an accuracy better than a micron.

2.5 Calibrations and tests

Various components of the setup were calibrated using standard methods to obtain their least counts and to set the limits on their performance.

2.5.1 Cantilever calibration

A. Resonance method

One end of the optical fibre is connected to Laser fibre Coupler to focus the laser from the source into the fibre. The other end of the fibre is etched to required cross section and is mounted onto the microscope stage. Emergent laser beam is collected via the objective and is observed using the camera through computer interface. A hollow conical plastic tip, attached to an ear phone, was pointed towards the tip of the fibre to focus the sound waves (see figure(2.10)).

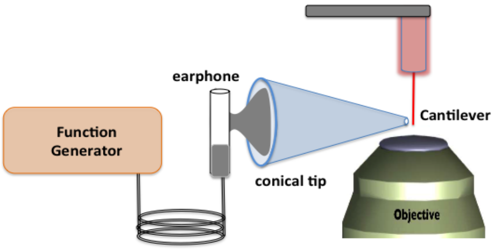

FIGURE 2.10: Schematic showing the process of exciting the cantilever with sound waves for calibration by resonance. A conical plastic tip focuses the sound waves generated, by feeding a sinusoidal wave form, from a function generator to an earphone on. The earphone is connected to the output of function generator. The resonance frequency of the cantilever is determined by tuning the sound waves using the function generator.

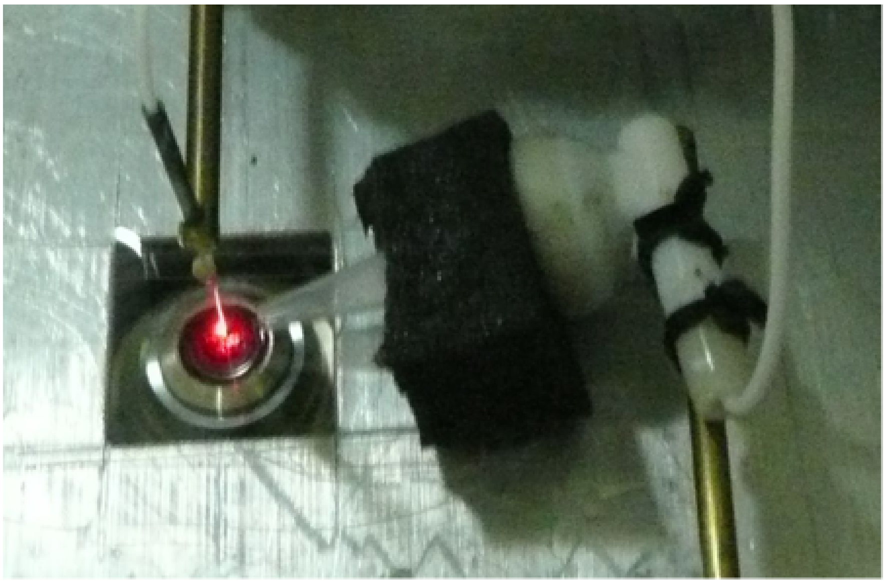

FIGURE 2.11: Photograph of the setup used for the resonance method of calibration.

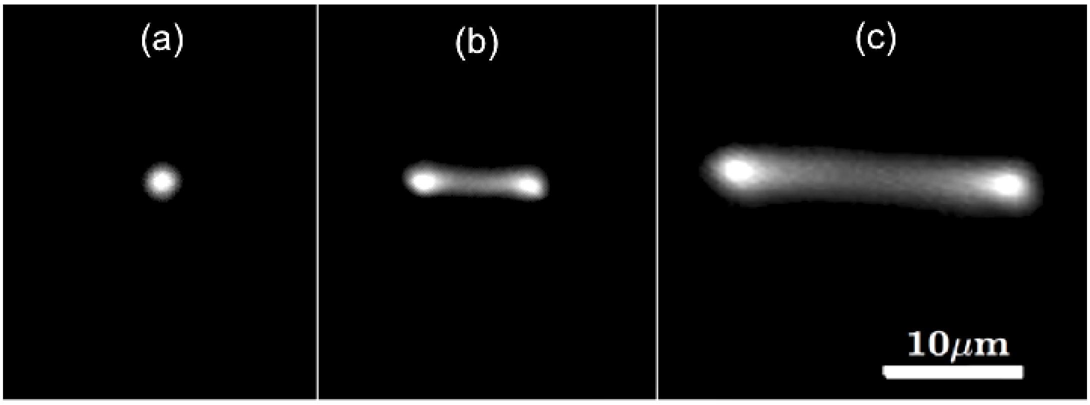

FIGURE 2.12: When the cantilever is at rest the light coming out of the tip appears as a circular light spot. After the cantilever is excited close to the resonance frequency, the amplitude of the cantilever vibration broadens and that is shown by the stretched spot which resembles a dumb bell. It can be seen that at resonance the amplitude is maximum.

The fibre tip was oscillated at desired frequency, the sound being generated via an Agilent 33220A arbitrary waveform generator (Agilent Corp., United States). With increase in the amplitude of oscillation (varied by adjusting the voltage), the spot gradually extends outwards in the shape of a dumbbell since the exposure time of the camera is much larger than the period of oscillation. The distance between the intensity maxima of the dumbbell was recorded by varying the frequency in small steps. Figure(2.12) shows the increase in amplitude of cantilever vibration at resonance.

We compared the experimentally obtained resonant frequency data with the theoretical expression for a slender cantilever. We use the known expression for the smallest characteristic frequency of transverse oscillations of a rod clamped at one end with the other end free [88]:

$$\omega_{min} = \frac{3.52}{l^2}\sqrt{\frac{EI}{\rho S}} \tag{2.1}$$

Here $I = \pi d^4/64$ is the area moment of inertia of the rod, $S = \pi d^2/4$ is the cross-sectional area, $\rho = 2.297 \times 10^3 \mathrm{kg/m^3}$ is the density of the glass fibre (measured by weighing known lengths of the fibre using a micro balance). The measured value $\omega_{min} = 2\pi\nu_r = 251.33$ rad/s was substituted in Eq. (2.1), to obtain a Young's modulus of $E = 141.91$ G Pa. We note that the measured value of E is roughly double of the value provided by the manufacturer of about 73G Pa. The resonance frequency of oscillation depends on the length and diameter of the fibre in the form $\nu_r \propto d/l^2$.

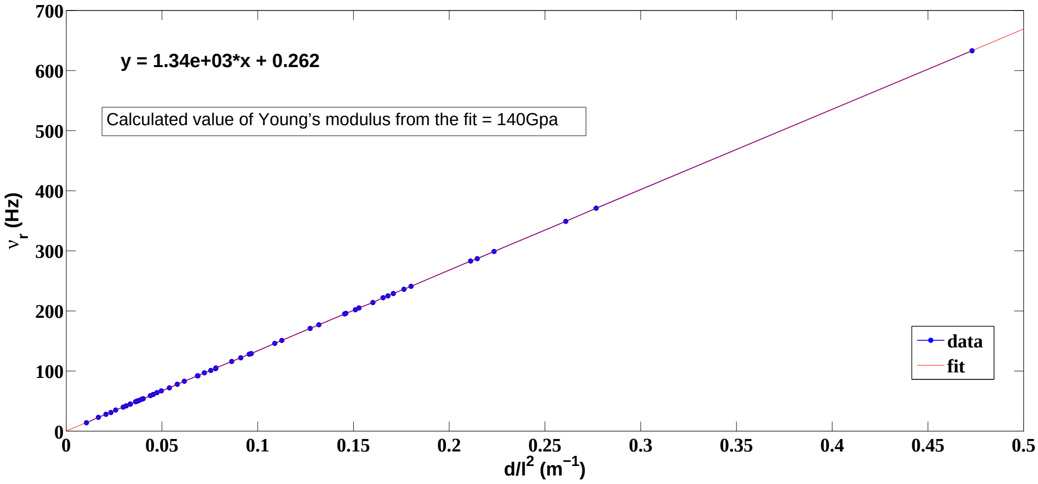

FIGURE 2.13: Calibration of the cantilever. Resonance frequency (ν_r) vs d/l^2 of the cantilever. This linearity shows that cantilever spring constant can be measured accurately from its length and diameter measurements.

In Fig.(2.13), we show this proportionality for a set of cantilevers with lengths in the range of 6-24.3mm and diameter in the range of 6.5-124.5μm. This agreement between the measured and the estimated values shows that the cantilever spring constant can be accurately estimated from a measurement of its length and diameter once the material is characterized, i.e. its Young's modulus and density are known.

In order to test for linearity(resonance frequency being independent of amplitude of the input sinusoidal signal), an etched fibre of length $l = 19.6$mm and diameter $d = 14\mu$m was oscillated using sound waves. Sound wave intensity was varied to change the amplitude of oscillation. In Fig. (2.14), a plot of the resonance frequency ν_r as a function of the amplitude at resonance γ_0 of the fibre tip is shown. The resonance frequency ($\nu_r = 40$Hz) is found to be nearly independent of the amplitude at resonance within the tested range of 25.3-69.1μm.

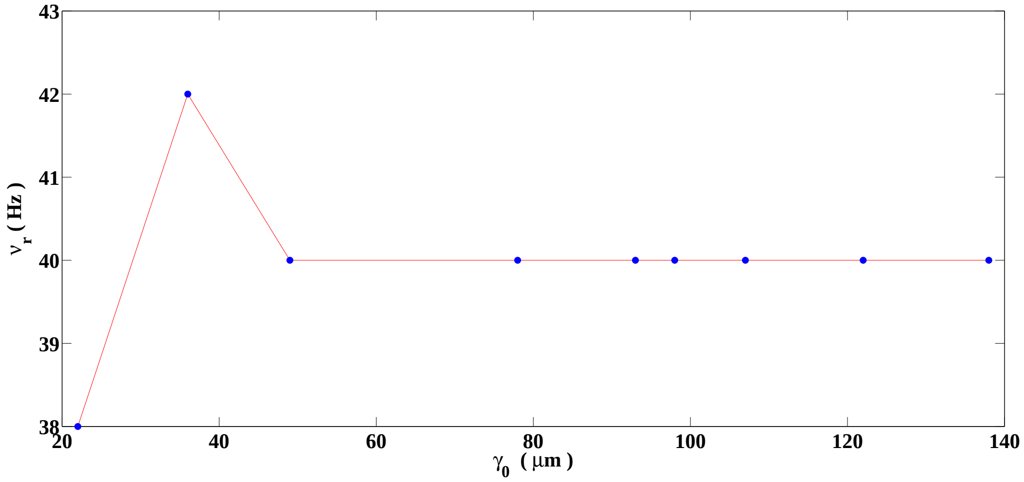

FIGURE 2.14: Plot of ν_r against amplitude at resonance (γ_0). The frequency remains constant for a wide range of amplitude variation.

B. Static method

In this method a 6cm long and 125μm diameter fibre is used as cantilever portion. The cantilever is mounted on a micro-meter translation stage and the tip of the cantilever was pressed against a calibrated sensitive balance. Tip of the cantilever exerts force on the balance on driving the other end of the cantilever using the micro-meter stage. The force(F) is read from the display of the balance and the cantilever deflection (ΔL) is the magnitude of micrometer drive. The motion of the weighing surface of the balance is assumed to be negligibly small. The deflection was applied in the steps of 5μm and the corresponding force values were noted. Young's modulus (E) was calculated using the following expression

$$E = \frac{FL^3}{3I\Delta L} \tag{2.2}$$

where L is the length and I is the second moment of inertia of the cantilever. For a cylindrical cantilever $I = \frac{\pi d^4}{64}$, where d is the diameter of the cantilever.

Plugging in the values of L and I we get

$$E = 6.0079 \times 10^{14} \frac{F}{\Delta L} \tag{2.3}$$

Slope of the fig. (2.15) gives $\frac{F}{\Delta L}$ and Young's modulus is calculated using equation (2.3).

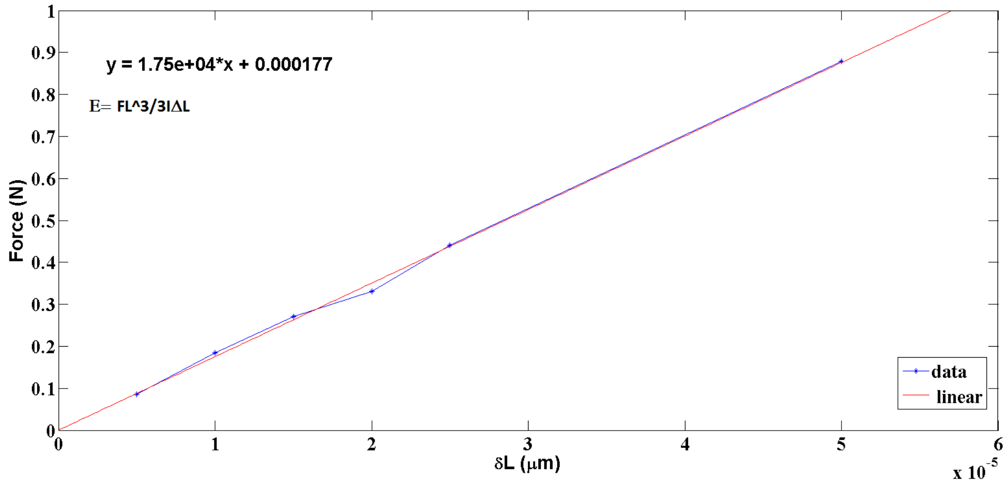

FIGURE 2.15: calibration of the cantilever using static method.

This method gave a Young‘s modulus value of 100GPa which is close to the manufacturer prescribed value. The value of spring constant obtained from the resonance method is larger by a factor of 1.5 as compared to the one we got from the static method. Some of the possible causes for the errors in resonance method are, the air resistance and the clamping methods [97]. The air resistance can be ruled out as the effect should decrease the resonance frequency and hence the spring constant. Cantilevers of different length and diameter combinations were used in the calibration process and there fore, contribution of errors from clamping method is doubtful. Further investigations are in progress to resolve this issue. In the experiments described in the next chapters spring constant calculated from static method was used for measurement of different parameters.

As we can tune the length and the diameter, we get wide range in the spring constant from $10^{-5} - 10$ N/m. Along with the position resolution and the of the device (discussed later), we can measure forces as low as 1pN.

2.5.2 Camera based detection system

The pixel resolution of the CCD camera was calibrated using a microscope calibration scale with a least count of 10μm (AX0001, OB-M, Olympus Corp., Japan). Here on, unless otherwise specified, we have used the 40x/0.5 objective. At this magnification, the calibration factor was found to equal 0.194μm per pixel. The image of a well-cut static fibre produces a nearly-Gaussian intensity profile on the camera. A Region Of Interest (ROI) larger than the beam profile is chosen when recording the data. The intensity-weighted centroid (or "centre-of-mass") of the fibre in the image plane is then calculated as $(x_{cm}, y_{cm}) \equiv (\sum_i I_i x_i/I, \sum_i I_i y_i/I)$, where $I = \sum_i I_i$, and x_i and y_i are the x and y positions of the ith pixel. The background intensity can affect the calculated position. To avoid this, the background intensity value I_b (2 times the average value along the edge of the ROI) was used as a cut off by setting $I_i = 0$ for $I_i < I_b$.

2.5.2.1 Scale calibration

Using the Olympus scale, the calibration factors of the different lens combinations for the microscope with Andor EMCCD camera were found to be:

1. 1 pixel = 0.368μm (for 20x/0.45 objective, optovar = 1.0x)
2. 1 pixel = 0.253μm (for 20x/0.45 objective, optovar = 1.6x)
3. 1 pixel = 0.161μm (for 20x/0.45 objective, optovar = 2.5x)
4. 1 pixel = 0.194μm (for 40x/0.5 objective, optovar = 1.0x)
5. 1 pixel = 0.128μm (for 40x/0.5 objective, optovar = 1.6x)
6. 1 pixel = 0.0811μm (for 40x/0.5 objective, optovar = 2.5x)
7. 1 pixel = 0.0781μm (for 100x/1.25 objective, optovar = 1.0x)
8. 1 pixel = 0.0503μm (for 100x/1.25 objective, optovar = 1.6x)

9. 1 pixel = 0.0324μm (for 100x/1.25 objective, optovar = 2.5x)

2.5.2.2 Noise estimation

In order to estimate the noise in this detection method we imaged a rigid cantilever, i.e. a short segment of an un-etched optical fibre with the tip stuck to a heavy aluminium block. A drop of immersion oil (Immersol 518F, Carl Zeiss AG, Germany) was placed on a cover slip above the objective with the tip of the fibre dipping into it, to reduce scattering due to any imperfections in the cut. These alterations gave a rigid cantilever with an almost perfect beam profile,enabling the estimation of detection noise. The position of the cantilever was recorded as a time series at 10Hz for 300s using the camera. The standard deviation for measured displacements of the x or y coordinate gives an estimate of the error in the detection method. A plot of standard deviation σ) as a function of microscope magnification is shown in Figure(2.16). Magnification was varied using different objectives and different tube lenses (1X, 1.6X, 2.5X). As can be seen from the plot,the noise decreased with increasing magnification and the best resolution was obtained at $M_o \geq 160$, with an error $\sim$ 1nm.

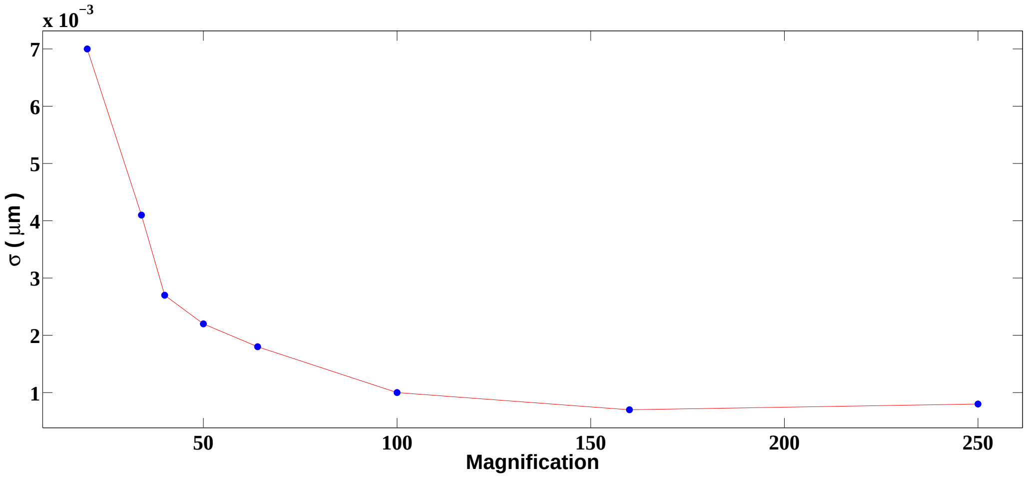

FIGURE 2.16: Plot of the standard deviation (σ) of the position of a rigidly mounted un-etched fibre, recorded using a camera as a function of microscope magnification. This trend indicates that the noise in the position measurement decreases with increasing magnification initially and saturates after certain magnification.

Table 2.1: CCD noise sources

Error source	Distribution
Signal light photon noise	Poisson
Back ground light photon noise	Poisson/Gaussian
CCD readout noise	Gaussian
CCD sampling error	Gaussian/correlated to spot size

2.5.2.3 Effect of magnification on the noise

When Charge Coupled Devices (CCD) are used for position detection, the CCD is generally placed in the focal plane of an imaging lens to detect the position of the light spot or point source. The intensity distribution of the image occupies a definite number of pixels and this number varies depending on the magnification of the objective used to focus the light on the CCD chip. Every CCD comes with some error contributed from the pixels and hence detected intensity varies from the actual intensity by this error, which affects the position resolution. In CCD based detection system there are different sources for these errors and each of these sources have different distributions in different conditions [98, 99]. The table (2.1) summarizes some of these error sources and their distributions.

In the process of calibrating the camera (explained earlier), we obtained the resolution as a function of magnification which is shown in the figure(2.16). It can be seen that the noise decreases with increasing magnification and then saturates. The sampling error and the readout noise of the CCD, decrease with increasing number of pixels and hence decrease with increasing magnification. At the same time each pixel contributes to a definite noise which is proportional to the number of pixels used in imaging. Therefore as the magnification is increasing the noise decreases initially and when this decrease is balanced by pixel noise, we see the saturation and beyond this point noise should go up. This feature sets a cap on highest useful magnification to get the best resolution.

As the CCD array is two dimensional, magnification of the objective used scales as the square of number of pixels. Therefore the detected noise should vary as inverse of magnification. We observe that the noise varies as $M^{-1.3}$ where M is the magnification of the objective (see the figure(2.17)). The difference in dependence is expected from the contribution due to remaining forms of the noise.

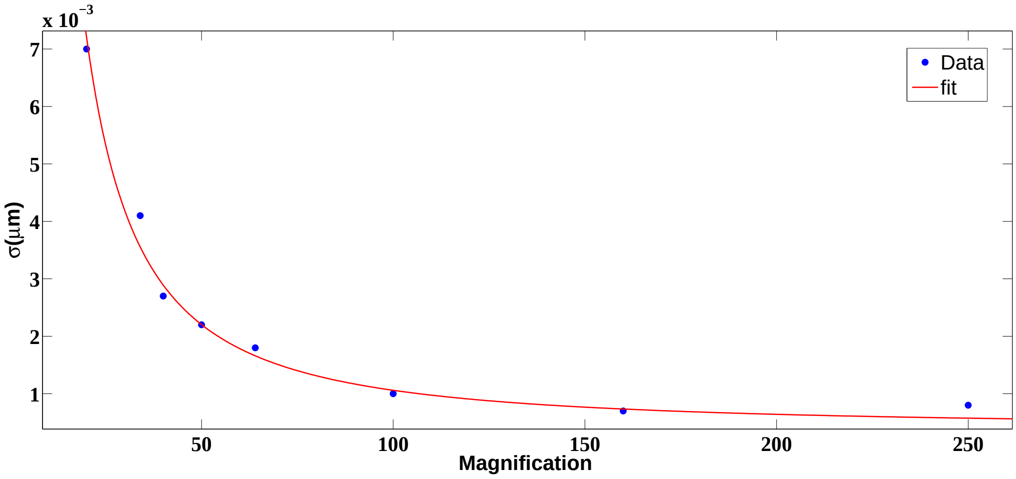

FIGURE 2.17: Noise level of CCD camera measured using a rigid fibre decreases with increasing magnification and later saturates. Standard deviation of the position-time data is plotted against the microscope magnification.

2.5.3 Position-Sensitive Detector (PSD)

The PSD used was a pin-cushion type two-dimensional model and the specifications are already mentioned in the setup description

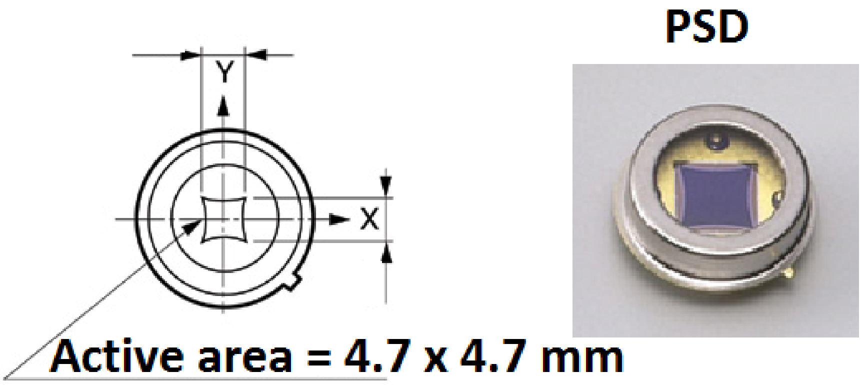

FIGURE 2.18: schematic and image of PSD. Schematic shows the active area of the PSD

2.5.3.1 Operating principle of PSD

PSD is operated under an applied reverse bias. When absorbed photons produce charge carriers (electrons and holes in the depletion region), this bias causes the charge carriers to move to the appropriate electrode (anode or cathode). The carriers have to first pass through the resistive silicon. As the P and N layers are produced with high spatial uniformity, the photo current at each electrode is inversely proportional to the distance between that electrode and the centroid of the incoming light spot. Hence the position of the light spot can be located by using the ratio of the signals from different electrodes.

2.5.3.2 Calibration

We calibrated the PSD using a manual micrometer stage and then the pre-calibrated camera. First we determined the linear range of PSD and then calibrated it for its position resolution.

In order to find the linear range of the working area of the PSD, we mounted one end of a stiff optical fibre on a translation stage and focused the laser onto the PSD directly, without using the microscope. The fibre was displaced in uniform steps along X and Y axes using the micro-meter stage and corresponding positions on PSD were recorded using LabVIEW software. Figure(2.19(a)) shows the PSD reading as a function of fibre displacement on the translation stage. By sweeping the cantilever across X and Y axes of the PSD, the linear range is determined. Figure (2.19(b)) shows the displacement as recorded by PSD matches with that of translation stage in the linear regime of PSD working area. The linear range of the PSD was found to be about 3.8mm along X as well as Y axes. Using the manual stage we could determine the linear range of PSD working area and also obtained the position calibration. As no microscope was involved in this process all the distances measured are in milli-meter .

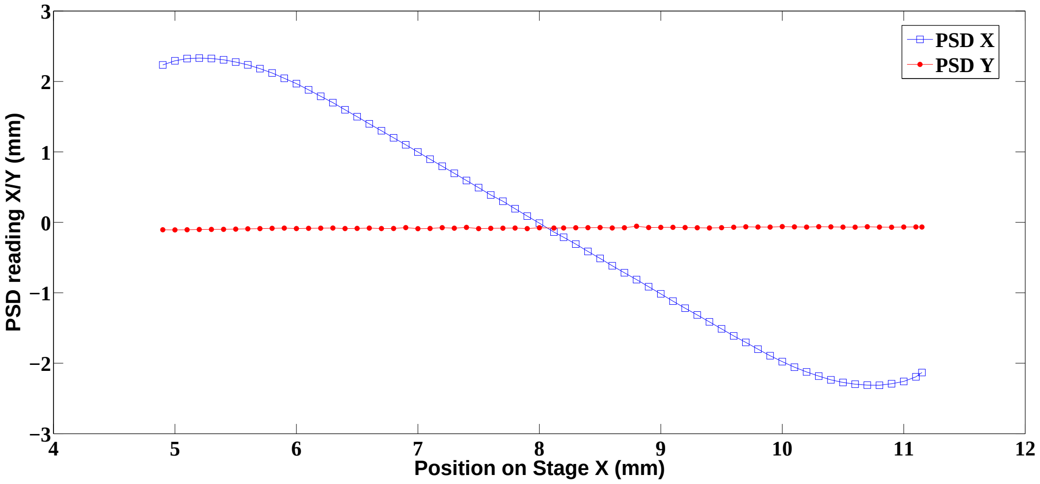

(a)

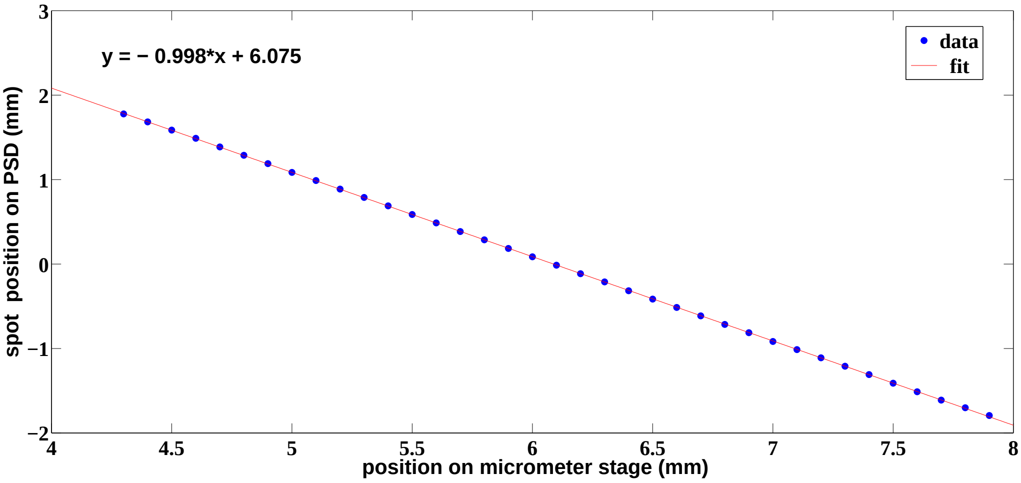

(b)

FIGURE 2.19: PSD reading against known displacement of the fibre mounted on an XYZ micro-meter stage along X-axis of the translation stage. Close to zero slope for the PSD's Y-axis data shows that axes of translation stage and PSD are well aligned. PSD's X-axis data shows both linear and non linear zones of PSD working area. (b) Linear region of PSD as calibrated against the micrometer stage.

In the next stage we calibrated the PSD against the Andor Luca camera. Camera was well calibrated and details are already given in the earlier section. Aim of calibrating the PSD against the camera was to confirm the results from the manual calibration and to obtain the calibration factor after including the microscope optics.

A rigid optical fibre was mounted on a translation stage and the laser was focused on camera as well as on the PSD simultaneously via microscope objective of 40x magnification. A beam splitter was used to direct laser on to the camera and the

PSD at the same time. An absorption filter was placed in front of the camera so as to keep the laser intensity below saturation limits of the camera. Position of the fibre tip was recorded using Image-J on camera and LabVIEW on PSD. The fibre was displaced in different steps using the manual micrometer stage and recordings were made for the position. Fibre position was maintained well within the linear range of the PSD obtained from previous measurements. Image sequences obtained from video recording were analysed using a home built MATLAB code. Figure (2.20) shows plot of position data as recorded by PSD vs that of camera for 40x magnification. As the camera data already incorporates the pixel to distance calibration factor for the used magnification, the slope of this plot acts as check on recovering the microscope magnification. The magnification value which we got from the slope matches with the calibrated value for the optics of the microscope camera system.

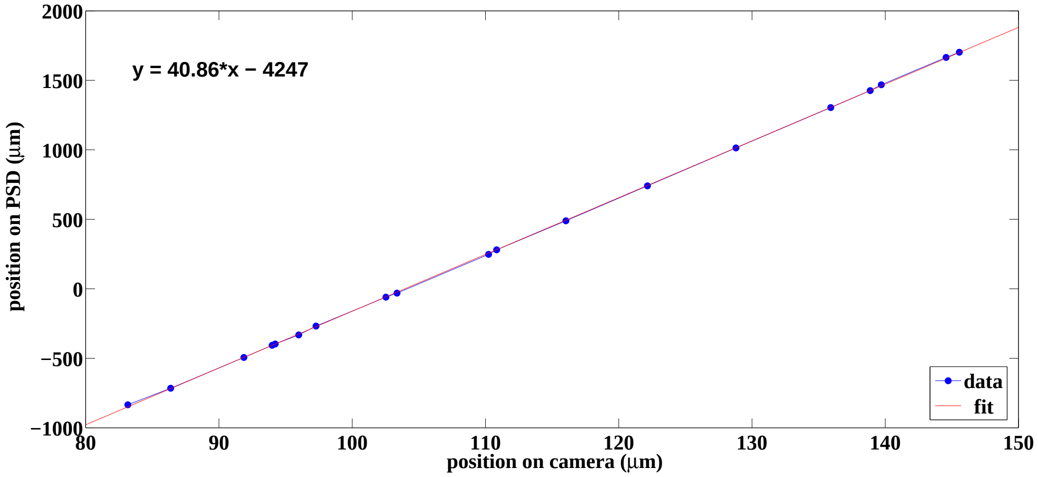

FIGURE 2.20: Calibration of PSD against camera. Fibre was mounted on a stage and the light coming out of fibre tip was focused on PSD and camera simultaneously. Images obtained on camera were processed to find the tip position which is the X-axis data and the PSD reading for the corresponding position is on Y-axis. The slope of this curve gives the magnification of the objective used.

2.5.3.3 Position resolution of PSD

Data is acquired from PSD via the signal processing circuit mentioned in set up description. This circuit employs a 12 bit card to output the data and the resistance length of the PSD is 5.7 mm. The estimated position resolution of the PSD is the ratio of resistance length and output buffer size which is $5700\mu\text{m}/2^{12} = 1.3916\mu\text{m}$ on PSD. This is the resolution with out considering any magnification. Effectively for a given magnification M_0 the position resolution of the PSD would be

$$\Delta r = \tfrac{1.3916}{M_0}\mu m$$

which amounts to 34.8nm for 40x magnification. This is the estimated position resolution from the device specifications. Now if we determine the noise experimentally recording the tip position of a rigid fibre as in the case of camera calibration, the only contribution to fluctuations in measured spot position should be the system noise (electronic etc). Therefore the measured noise should be either the system noise or resolution due to digitization (calculated resolution) whichever is large. We followed the same protocol as was implemented for camera calibration and recorded the rigid fibre tip position on PSD. Figure (2.21) shows the PSD reading vs time at 40x magnification. It can be noticed that the noise due to digitization dominates and there is a clear agreement between measured and estimated noise.

The position resolution for PSD at 40x magnification is about 35nm. This value is much larger than that of camera which is about 2 nm at this magnification. The trade off here is the temporal resolution of 200 Hz for the PSD as against the 10 Hz for the camera. Noise measures for all the magnifications from 20x to 250x were verified experimentally following the above mentioned protocol.

2.5.4 Quadrant Photo Diode (QPD)

The third source we used for position detection was the Quadrant Photo Diode (QPD). the specifications are already mentioned in the set up description.

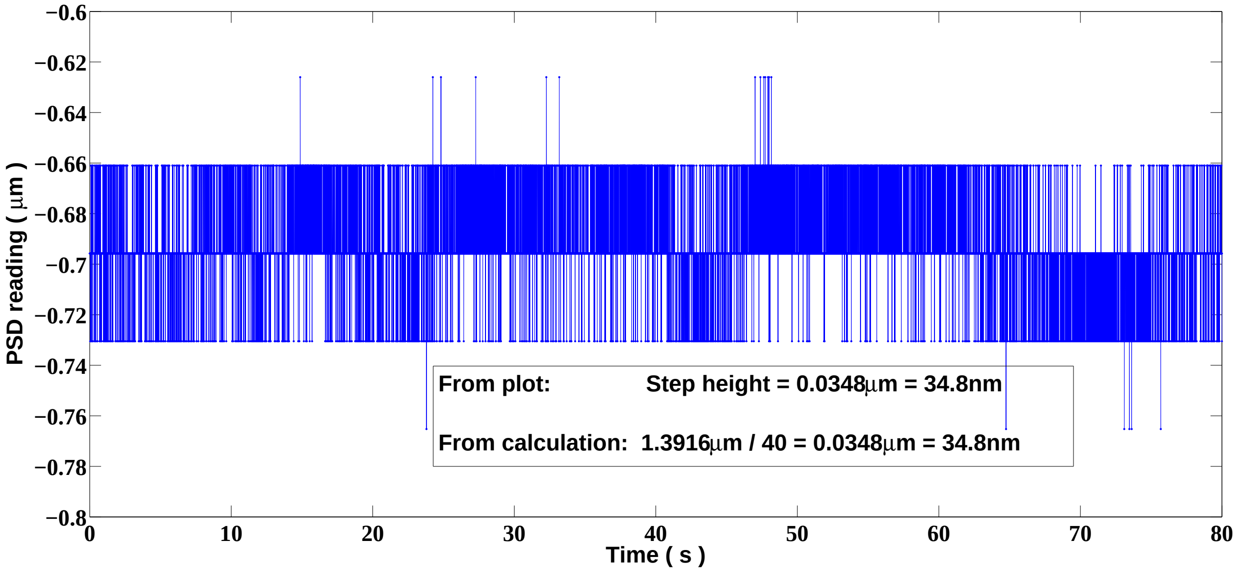

FIGURE 2.21: (a) Position time plot for noise determination at 40x magnification with details of position resolution. It can be seen that the step size is 35nm at this magnification which comes from 1.3916μm/magnification.

2.5.4.1 Operational principle and working

Quadrant photo diodes work on the principle of having four photo diode elements (anodes) separated by a small gap on a common substrate with a shared cathode (see figure(2.22). The anode or active area of each element is independent, so that a light spot illuminating a single quadrant can be electrically characterized as being in that particular quadrant. As the light spot moves across the detector, its energy gets distributed between adjacent elements of the detector and the difference in electrical contribution to each segment defines its relative position with respect to the centre of the detector. Consequently, the relative intensity profile over the active area of the device determines the position of the light spot. The position information from the detector can be obtained only over a linear distance of about twice the spot diameter or until the edge of the spot has reached the detector gap. Therefore while working with lasers and other collimated sources beam defocusing may be required to get the maximum range. Also it is generally presumed that the spot intensity distribution is symmetrical and produces a Gaussian profile.

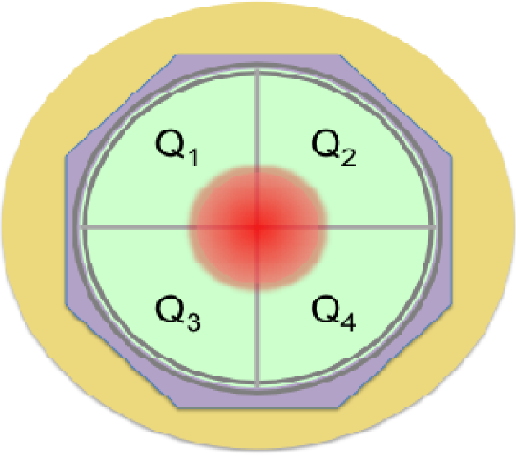

FIGURE 2.22: Schematic of a QPD. The incident light spot should illuminate all the four quadrants for position detection. Output from each quadrant is obtained in terms of voltages. X and Y positions are determined performing appropriate arithmetic on these voltage values

2.5.4.2 Position calculation

To get the position information, the following procedure is used.

1. The output is measured in volts as V_1, V_2, V_3, V_4 from Q_1, Q_2, Q_3, Q_4 respectively.
2. X and Y positions are calculated using the following expressions.

$$X = \frac{(V_1 + V_3) - (V_2 + V4)}{V_1 + V_2 + V_3 + V_4} \tag{2.4}$$

$$Y = \frac{(V_1 + V_2) - (V_3 + V4)}{V_1 + V_2 + V_3 + V_4} \tag{2.5}$$

The QPD comes with a sum and difference amplifier module where the sum $(V_1 + V_2 + V_3 + V_4)$ and the differences $(V_1 + V_3) - (V_2 + V4)$ and $(V_1 + V_2) - (V_3 + V4)$ are given as output. A DAQ card with 2MHz maximum acquisition speed was used to acquire the data from the quadrant diode circuit. Data acquisition and the remaining calculation as required from the equations (2.4) and (2.5) were performed using home written LabVIEW code. With this process we have position information from QPD in terms of voltage. In the next stage we calibrate the QPD against the piezo to get position information in terms of distance units.

2.5.4.3 Calibration

We calibrated the QPD against the piezo actuator to find the voltage to position conversion. A stiff fibre is mounted on piezo actuator and is focused at the centre of QPD. A LabVIEW code was written to drive the piezo, acquire and process the data from QPD. Fibre tip position as a function of time was recorded. The fibre is displaced by known steps by commanding the piezo and corresponding voltage output was recorded from QPD.

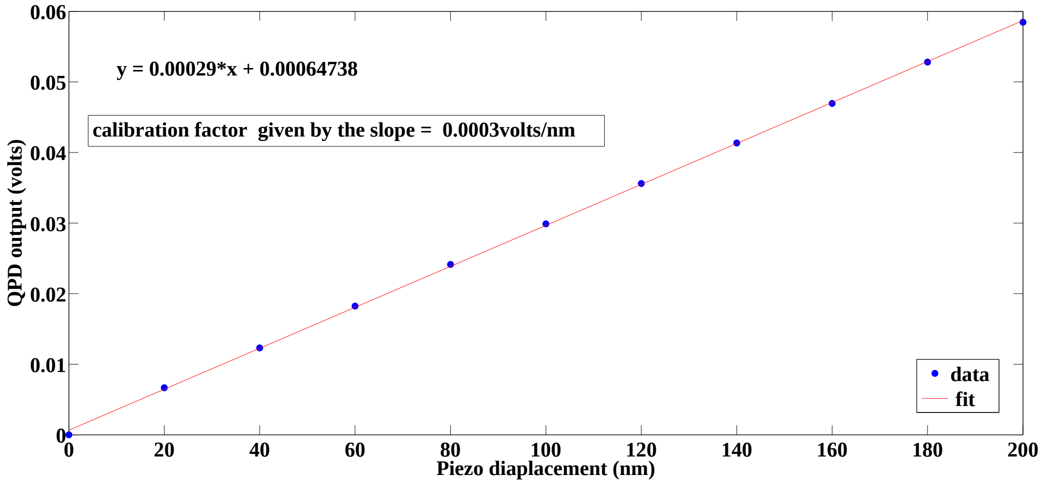

FIGURE 2.23: Calibration of QPD against Piezo. A stiff was fibre mounted on piezo and the light was made incident on the QPD. As the piezo moves, the position information is given out in micrometers while the corresponding QPD reading is obtained in voltage. The slope of this curve gives the calibration factor for the magnification used.

To determine the position resolution a stiff fibre glued to aluminium block was used similar to that used for the noise determination tests for camera and PSD. Position of the fibre tip was recorded as a function of time at 100 kHz. Standard deviation of this data is obtained and is taken as the noise or position resolution. Figure (2.24) shows the trajectory of the fibre tip and the position resolution obtained was about 1.5nm at 40x magnification.

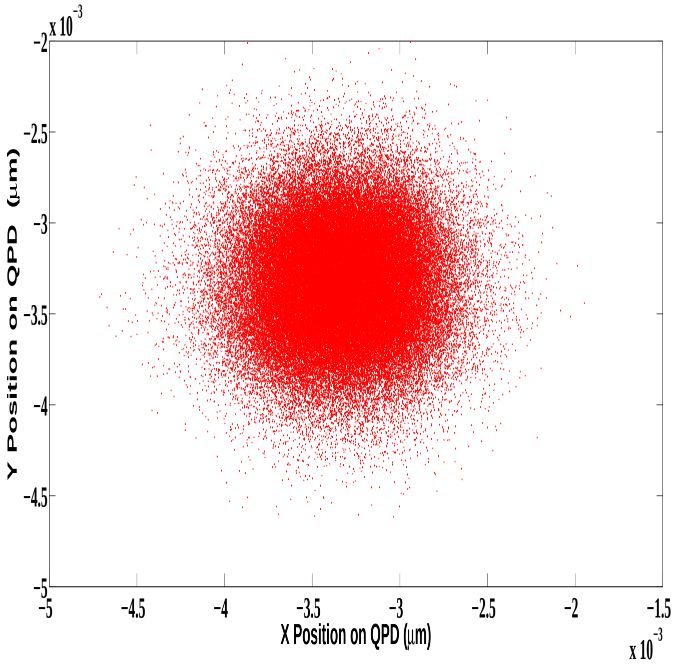

FIGURE 2.24: Position data obtained for a stiff fibre using QPD. The width of this distribution is a measure of the resolution.

2.5.5 Comparison of detection mechanisms

The three detection mechanisms we employed have their own pros and cons. Based on the experimental need one or more mechanisms were employed for position detection. For 40x magnification, Andor camera has an excellent position resolution of about 2nm but has a very poor temporal resolution about 10Hz. It is not possible to get real time data using camera but it is the simplest mode of detection to implement. The PSD has a larger working area but its position resolution is about35nm. Considering QPD, it has a very good temporal resolution of the order of MHz and spatial resolution similar to that of camera but very small working area of less than a micron. Table (2.2) summarises their capabilities and short comings in numbers for 40x magnification.

Choice of the detection mechanism to be employed is based on the experimental requirement. For axon pulling experiments, we can not use QPD as the cantilever is used to pull on the axons and needs several microns of detection area where camera and PSD are suitable detection modes. For extension rheology of polymers the needle is pulled and cantilever deflections are usually well within QPD working

Table 2.2: Comparison of position detection devices

Device	spatial resolution (40x)	temporal Resolution	active area (40x)
Andor camera	< 2nm	10hz	200μmx200μm
PSD	35nm	200Hz	120μmx120μm
QPD	$< 2nm$	1MHz	0.5μmx0.5μm

area. Therefore QPD or PSD would be suitable for cantilever tip detection and camera for imaging filament evolution. Similarly for bacteria experiments QPD would be the best choice as the cantilever deflections are not more than a couple of hundreds of nano-meters.

2.5.6 Piezo electric actuator

The piezo actuator (P-841.60,Physik instruments GmbH Germany) with an inbuilt strain gauge sensor has a 90μm travel range, and is controlled by a single-axis piezo servo controller (E-625.SR) via a USB interface. The strain gauge acts as a feedback system to the controller, in order to overcome hysteresis effects. The piezo can be operated in an open loop mode without employing the strain gauge or in a closed loop mode, where the strain gauge is functional.

The piezo was calibrated against the camera with the following protocol.

1. A needle was magnetically attached to the piezo actuator

2. 2.84μm diameter Carboxylate-modified fluorescent micro-spheres (Invitrogen corp., United states) were stuck to the tip of the needle.

3. The micro-spheres were imaged at 40x magnification using Andor EMCCD camera.

4. The needle was displaced by commanding the piezo using the application software PI mickromove Ver. 2.6.0.

5. Images of the bead were recorded by camera for 180 seconds per trial.

A home built Matlab code was used for the analysis. The standard deviation of the noise for the X_{cm} and the Y_{cm} coordinates was found to equal 0.0056μm and 0.0054μm respectively.

Position calibration against camera was performed for the displacement of the actuator over the entire travel range of 90μm, in steps of 5μm. Then similar recordings were done with 10nm and 1 nm steps commanded to the piezo. In Fig. (2.25)(a), the centre of mass coordinate Y_{cm} of the spot is plotted calculated from the recorded images vis-a vis the commanded piezo displacement of 5μm steps. In figs.(2.25)(b) and (2.25)(c), Y_{cm} is plotted for piezo displacements with step sizes 0.01μm and 0.001μm respectively. We can see that piezo actuator motion and spot tracking using the camera, agree to an accuracy of better than 10nm at 40X magnification..

2.6 Feedback Mechanism

To control the force or extension as per the requirement a user-friendly software for the MER has been written using LabVIEW. The software allows the user to select from the modes of operation: Constant Strain Mode and Constant Force Mode. The user-selected mode is implemented via a feedback-loop algorithm. The screen-shot of the Front Panel of the code is shown in Fig.(2.26). The user selects the mode of operation and supplies as input, the desired value of the extension (or force), the diameter and length of the cantilever and the initial filament length in case of polymer rheology experiments (after loading the sample and allowing the filament to stabilize). The code implements the desired mode of operation and outputs the calculated spring constant and the current values of the PSD and piezo positions. A graphical display shows the current values of the force and the strain as a function of the elapsed time. A flowchart outlining the different steps of the algorithm is shown in Fig.(2.27).

Force and extension are defined in terms of the measurable quantities which are the PSD reading and strain gauge output of the piezo. These definitions vary

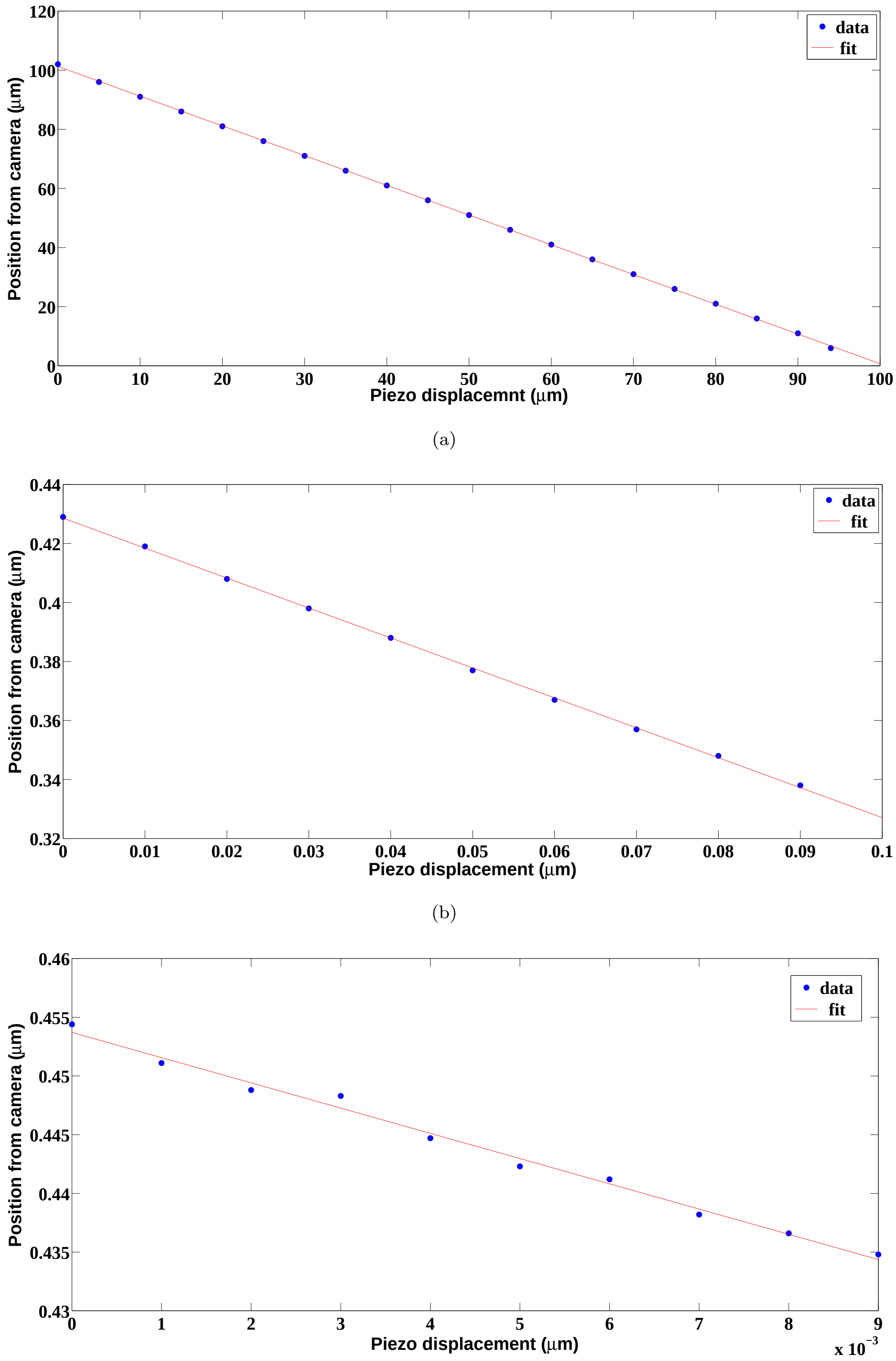

(a)

(b)

(c)

FIGURE 2.25: Plot of the Ycm coordinate of the bead calculated from camera images as a function of the commanded piezo displacement, insteps of (a) 5μm (b) 0.01μm or 10nano-meter and (c) 0.001μm or 1nano-meter

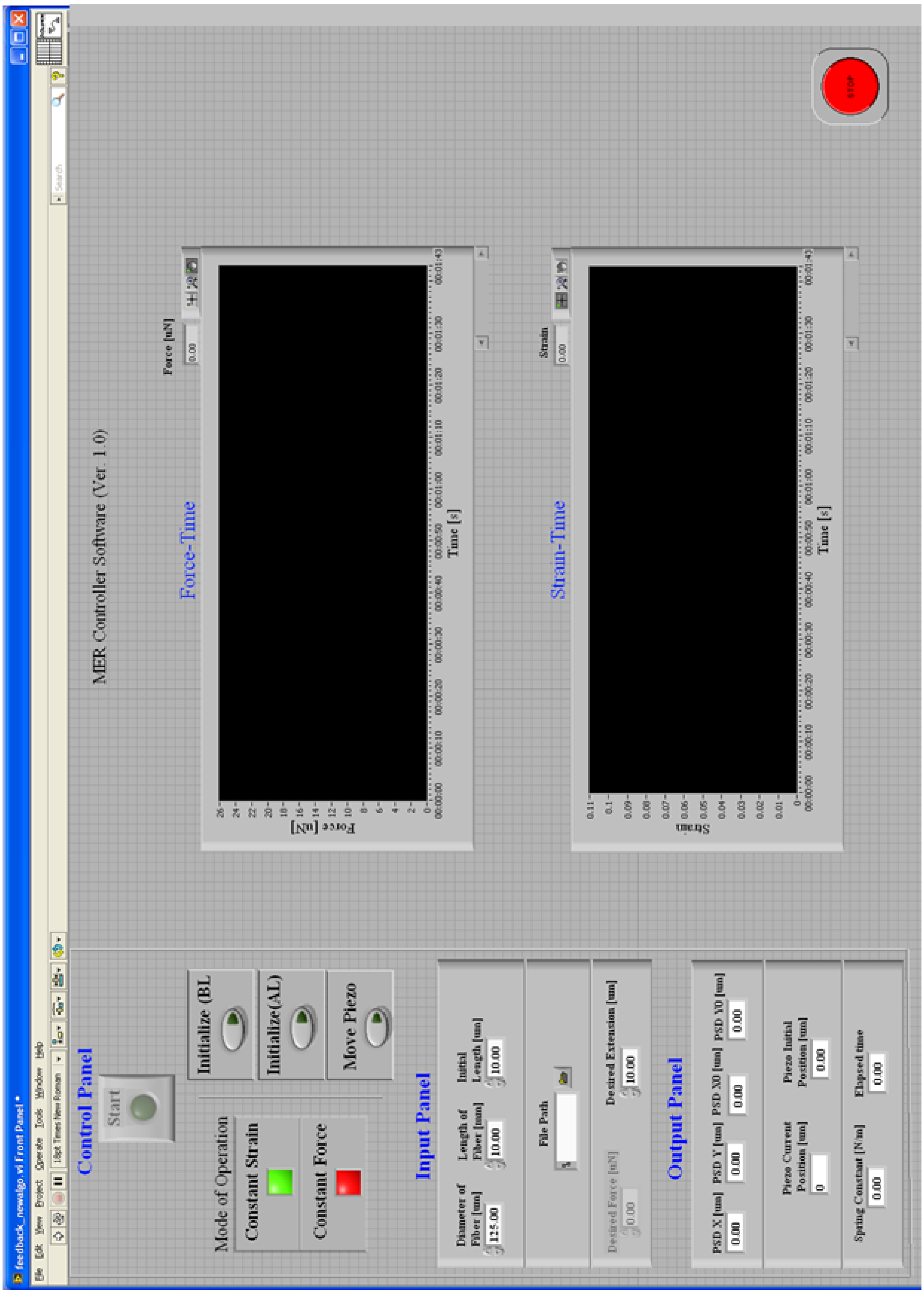

Diameter of Fiber [um] 125.00

Length of Fiber [mm] 10.00

Initial Length [um] 10.00

Desired Force [uN] 0.00

Desired Extension [um] 10.00

PSD X [um] 0.00

PSD Y [um] 0.00

PSD X0 [um] 0.00

PSD Y0 [um] 0.00

Piezo Current Position [um] 0

Piezo Initial Position [um] 0.00

Spring Constant [N/m] 0.00

Elapsed time 0.00

Force [uN] 0.00

Strain 0.00

FIGURE 2.26: A screen shot of the MER Controller software, which permits operation of the device in constant force or constant strain modes via a feedback-loop algorithm.

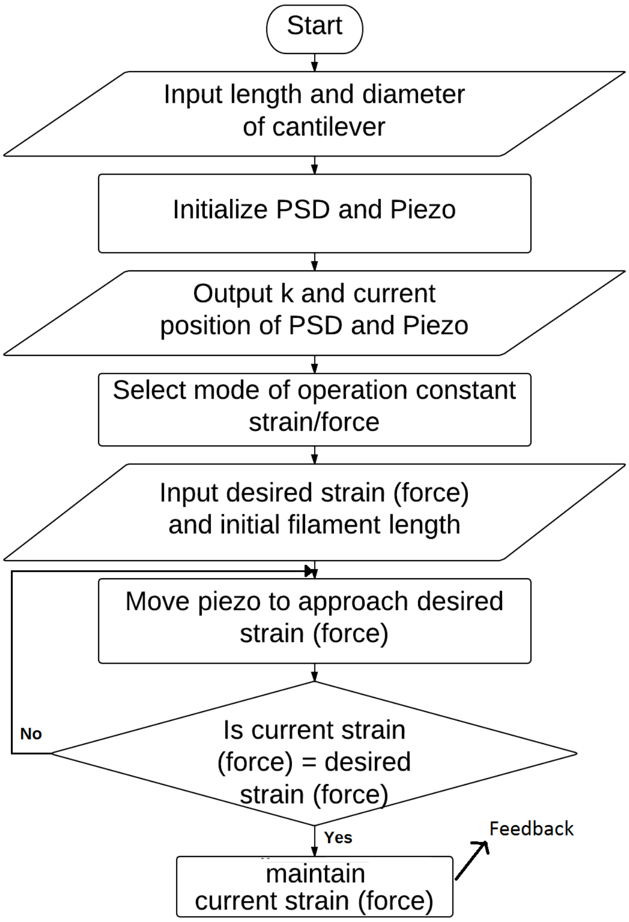

FIGURE 2.27: A flowchart of the feedback-loop algorithm for controlling the MER

based on whether the experiment uses cantilever on piezo as in the case of axon pulling experiments or the rigid rod is driven by the piezo which is connected to cantilever via a polymer in extension rheology experiments. Details of these definitions are already discussed in earlier sections where setup configurations are described.

The figure(2.28) shows the results of imposed constant extension on a polymer(PDMS). A drop of polymer was placed between the cantilever and the other rigid rod mounted on the piezo.Feedback algorithm was used to maintain the filament extension at 4μm. It can be seen that while the extension is maintained constant, force relaxes in time.

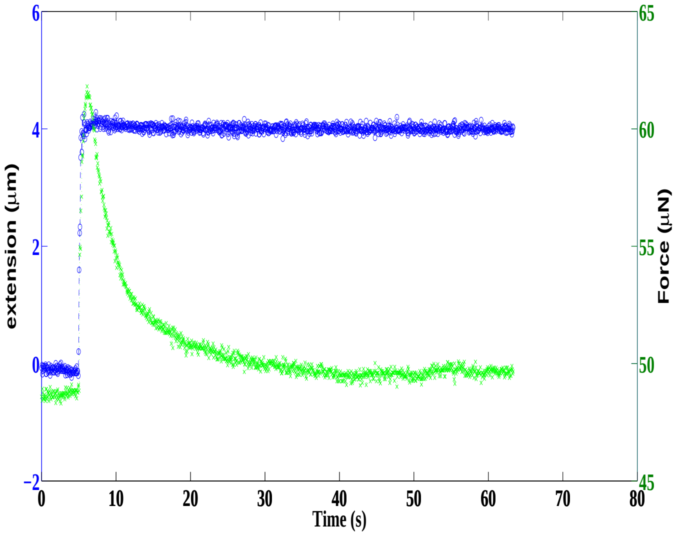

FIGURE 2.28: Extension and force plotted as a function of time for a polymer under imposed constant extension. While the extension reaches the imposed value and remains close to this value, the force shows relaxation in time.

Similarly the figure(2.29) shows the implementation of constant force during filament extension of a polymer solution. In this case the imposed force is maintained close to the commanded value and the response of the extension in the filament can be seen. The filament extends continuously till it breaks up.

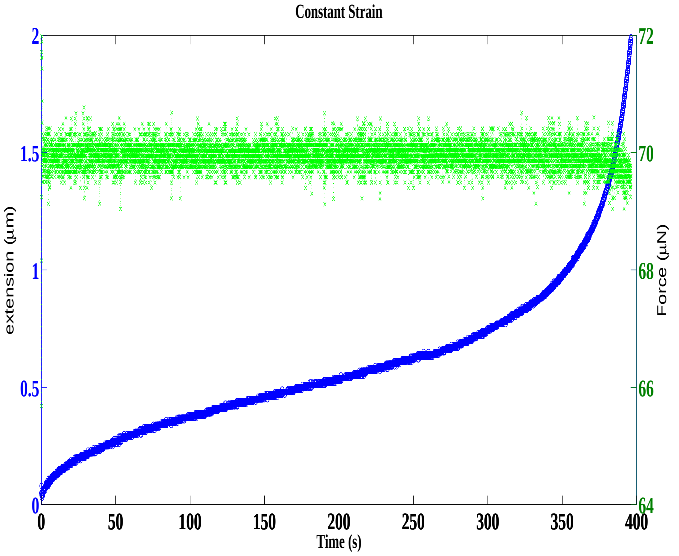

FIGURE 2.29: Extension and force plotted as a function of time for a polymer under imposed constant force. While the force reaches the imposed value and remains close to this value, the extension increases in time until the filament breaks.

Table 2.3: Comparison of MER with different force devices

Property	AFM	Optical Tweezers	Magnetic Tweezers	MER
Spatial resolution (nm)	$0.5 - 1$	$0.1 - 2$	$1 - 10$	$1 - 2$
Temporal Resolution(s)	10^{-3}	10^{-4}	$10^{-2} - 10^{-4}$	10^{-4}
Stiffness range(pN/nm)	$10 - 10^5$	$0.005 - 1$	$10^{-6} - 10^{-3}$	$10^{-8} - 10^{-1}$
Force range(pN)	$10^{-1} - 10^4$	$10^{-1} - 10^2$	$10^{-3} - 10^2$	$1 - 10^{11}$
Displacement range(nm)	$0.5 - 10^4$	$10^{-1} - 10^5$	$1 - 10^5$	$1 - 10^5$
Probe geometry	V-shaped	spherical	spherical	Cylindrical
probe size(μm)	$100 - 400$ (Length)	$0.25 - 5$ (Dia)	$0.5 - 5$ (Dia)	$7 - 125$(Dia), $3000 - 20000$ (Length)
Method of position detection	indirect	indirect	direct	direct
Applications	pulling, surface scanning	3D manipulation Tethered assay Interaction assay	Tethered assay, topology	Pulling, Force sensing extensional rheology
Advantages	High force Z-scanning	Low noise low drift	Force clamp, rotation	Wide range in force, simple design
Limitations	Large minimal force	Photo damage Sample heating	Force hysteresis	Long and fragile probe

2.7 Comparison of MER with other force devices and Rheometers

In the introduction I tried giving a glimpse of various competing techniques. In this section I will summarize the comparison of some of the standard devices and MER giving a feel for numbers for some of the important properties in the form of tables. Table (2.3) gives comparison of MER with AFM, Optical tweezers and Magnetic tweezers and table (4.1) compares MER with CaBER and FiSER.

Table 2.4: Comparison of MER with other Rheometers

Property	CaBER	FiSER	MER
Mode of operation	capillary breakup	Filament stretching	Both
Strain profile	Step	Exponential	Both
Force Measurement	Not measurable*	Measurable	Measurable
Force sensitivity	-	10μN	1pN
Force range (mN)	-	$0.01 - 500$	$10^{-9} - 10^{-2}$
Zero Shear viscosity range ($Pa.s$)	$10^{-2} - 10^{3}$	$10^{0} - 10^{4}$	Yet to be confirmed
Plate Geometry	Flat	Flat	flat/curved
Plate diameter	6mm	10mm	125μm
sample Volume	few ml	few ml	few pl

2.8 Discussion

The field of force measurement is equipped with several state of art instruments and we have added one more cutting edge tool to the arsenal. We built a force measurement device that can be applied to perform a variety of experiments in the fields of mechano biology active matter dynamics and extensional rheology. The device has force resolution of the order of a pico-newton and position resolution of the order of a nano-meter. The device can be operated in passive as well as active modes to sense or apply forces of magnitudes discussed earlier. The feedback control enables measurements in constant extension or constant force modes as per the need. A variety of detection mechanisms employed make experiments at different length scales possible.

Further development and up gradation of the device can make it an even more powerful tool to handle a variety of problems. Following are a few such possibilities in the wish list.

1. At present the maximum displacement is limited by the travel range of the piezo which is 90μm. We can employ mechanical amplifiers to increase this travel range.

2. The etching process in the current state is some what cumbersome to handle and time consuming. The whole fibre along with FC-connector has to be taken to the chemical facility, which means each time the fibre has to be disconnected

and reconnected to the laser source. Life of the etched fibre depends mainly on the handling capability of the user. Typically an etched fibre survives for three to four weeks (10-15 experiments) with some experience in handling the fibres. Also it depends on the frequency of mounting and un mounting the fibre. As an alternative, we can fix the position of the optical fibre connected to the laser source. Several short fibre pieces can be etched simultaneously giving identical cantilevers. We can couple these units to the fixed fibre with the help of fibre-fibre coupling systems. Implementing this modification to the setup gives a lot of ease in handling the device and time advantage.

3. Incorporating humidity and temperature control (temperature control is now available) will enable handling biological samples like neuronal cells and aqueous samples like silk efficiently.

Chapter 3

Dynamics of active suspensions

3.1 Introduction

Dynamics of active matter, explored using statistical physics and hydrodynamics, is an emerging area where advanced technology can contribute to make it experimentally rich. Many a system like living organisms at cellular level [42–44] systems of molecular motors [45–47], and granular systems under vibration [50] show dynamics that are much different from that of standard equilibrium systems. This non-equilibrium behaviour is usually due to the inherent nature of these systems to consume or lose energy. In this context, bacterial baths [51–55] form attractive model systems owing to various reasons. The energy input is homogeneous, individual bacteria can be directly observed, bacterial cells are easy to culture and grow and several characteristic parameters like density, activity, and swimming behaviour [51] can be controlled. There are reported experiments on different types of bacterial non-equilibrium behaviour. Also on theoretical front a great deal of work is presented on the dynamics of the collective active systems, fluctuations and instabilities [48, 57], and rheological phenomena of these active systems [58], and giant density fluctuations [59, 60].

I will introduce some of the reported works on tracking bacterial cells and/or tracer particles in bacterial suspensions, to understand some aspects of their dynamics and go ahead to present our experimental work performed using the force measurement device described in earlier chapters.

An experimental paper by Wu and Libchaber [52] is one of the early works on studying tracer particle motion in a bacterial bath. They mixed fluorescent beads in a bacterial bath drawn on a freely suspended soap film. Positions of the beads were recorded as a function of time. Mean square displacement (MSD $=< r^2(t) >$) vs time plots of this data shows super diffusive pattern for shorter time scales and diffusive nature in the long run. The crossover happens at around $2 - 4$ seconds while the observation continues till more than 100 seconds. They attribute this crossover to bacterial activity and not to inertia of the particles.

The next paper surveyed is by Mingming Wu and co-workers [100]. In this work they track the bacterial cells using a Three-Dimensional Population-Scale Defocused Particle Tracking technique. The bacterial cells are made fluorescent and tracked. Three different strains of E.coli are used as samples here,namely RP-437 (wild type), RP-1616 (tumblers) and RP-9535 (swimmers). MSD vs time is plotted for a period of 10 seconds and they see the effective diffusion coefficient D, increasing from tumblers to wild type to swimmers.

A paper by A G Yodh and co-workers [101] gives the measurement of one and two point correlation functions of beads in bacterial bath using the wild type and tumblers. They confirm that viscosity does not change for the concentrations used in the experiment, by performing response measurements using optical tweezers. They conclude that these measurements demonstrate violation of fluctuation dissipation theorem and the macroscopic stress fluctuations depend on microscopic swimming behaviour of the cells (strain used).

Raymond Goldstein and his group [102] study tracer particles in Alga Chlamydomonas. They show that while cells exhibit ballistic motion, the tracers embedded in the suspension move diffusively.

The force apparatus described in chapter (2) has an estimated force sensitivity close to 1 pico-newton [96]. The individual bacterial cells exert typically forces of the order of a pico-newton. We planned to first verify the capability of our device to measure fluctuations of the cantilever due to the effect of low density bacteria in suspensions and then study how the nature of dynamics of active particles influence statistical properties of the system. For our experiments we used well characterised strains of E.coli with different run and tumble behaviours.

With the help of our device we introduce a new method to probe active suspensions. There are definite advantages of using this device as compared using the techniques like optical tweezers. Experiments do not suffer from the issues like to local heating up of the sample and co-trapping of bacterial cells with beads.

Having different strains with us, we decided to perform two different types of experiments with these bacterial baths.

1. Cantilever based experiments, where the cantilever of suitable dimensions is immersed in the bacterial bath and deflections of the cantilever recorded and analysed for various parameters.

2. Particle tracking experiments, where fluorescent beads mixed in bacterial baths are tracked and analysed. These experiments were aimed at comparing the results of cantilever experiments wherever relevant in terms of numbers or trends.

These two types of experiments are completely different in nature and other than the sample (bacterial bath at a given density) there are no shared features. As we started with the motivation of determining the parameters like effective temperature due to bacterial activity, the choice of performing the experiments in the above two modes gives the estimate of the desired quantities independently and their agreement in values/trends stands as a robust test for the consistency in the results. All the experimental sets in both the modes were repeated 3 times with fresh cultures.

3.2 Characterized strains

E.coli can be genetically modified to exhibit specific characteristics predominantly like growth without motility, swim or tumble etc. We used three well characterized strains of E.coli RP-5232, RP-437 (source Lab of Judith Armitage, Oxford University) and RP-1616 (Source-Sandy Parkinsons lab, Utah). RP-5232 is a predominant swimmer, RP-437 swims and tumbles (wild type) and RP-1616 is a predominant tumbler. All these strains are rod shaped cells and are nearly $2-3\mu$m long and close to 1μm in diameter. While RP-5232 has a typical swimming speed of 30-60 microns/sec, RP-1616 is characterised for the parameters like tumbling frequency ($1.8Hz$) and a mean tumble time (0.2s) [103].

All these strains were cultured using the standard protocols [104], tested for optical density OD-600 to be around 0.6. This sample was diluted to required densities, using Tryptone Broth and motility buffer. Details of culture protocols and media recipes are given in Appendix B

3.3 Cantilever based experiments

The first set of cantilever based experiments were performed to find the effect of activity of different strains on the cantilever fluctuations.

The optical fibre based force setup built in our lab was used for this set of experiments. About 400μl of bacterial suspension was taken in a transparent cylindrical container of height 22mm and diameter 3mm with a glass cover slip as the bottom surface. The container was placed above the objective of an inverted microscope (Zeiss Observer.D1, Carl Zeiss GmbH, Germany) in an aluminium box which covers the microscope stage, to minimize the fluctuations due to air currents etc. A portion of optical fibre was etched to make a cantilever about 9μm diameter and length was fixed at 21mm. This cantilever was treated with Bovine Serum Albumin (BSA) in order to prevent bacterial adhesion to the cantilever. The cantilever along with a small portion of the holder was inserted into the solution in the container as shown in figure (3.1). The cantilever tip was focused using a 40x objective lens. Laser light coming out of the cantilever was collected via this objective and was made incident on to the calibrated QPD to track the cantilever tip position. Also we used the Andor Luca camera as detection mode for some of the experiments. The aluminium box was covered at the top and was sealed so as to minimize the external disturbances. Both the camera and the QPD have about few nm position resolution. While QPD has about a MHz temporal resolution the camera is limited to 10Hz. As the cantilever is calibrated for its stiffness, its spring constant can be obtained with the knowledge of its length and diameter. Cantilever deflection as a function of time is the measured quantity using the camera or the QPD [96].

Before proceeding for the measurements, the extent of convection was tested by imaging suspended tracer particles in the medium without bacteria. The following measures helped eliminate convection almost completely.

1. A narrow tube was chosen for the container.

2. A drop of mineral oil was placed on top of the suspension to prevent evaporative cooling.

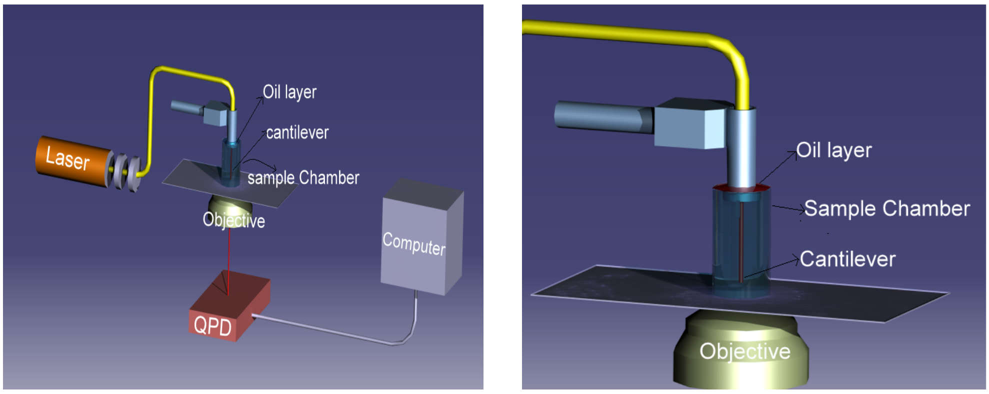

(a) (b)

FIGURE 3.1: (a) Schematic of the setup used for recording the fluctuations of a cylindrical cantilever dipped in bacterial suspension. The cylindrical container, with glass cover slip as bottom surface, is filled with the bacterial solution and an etched fibre acting as cantilever is immersed in the bath. The effect of bacterial activity reflected in terms of cantilever fluctuations can be tracked by a QPD. Choice of a narrow tube and placing a drop of oil on top of the liquid help minimising convection. (b) Zoomed in version of working area.

Initially, control experiments were performed using plain medium without bacteria and cantilever position was recorded with time. The standard deviation of the cantilever fluctuations was found to be $12 - 15$nm. This value is about an order of magnitude larger than the position resolution of QPD which is about 1.5nm for the used magnification (40X). Then the medium was replaced by bacterial solution of different strains and similar recordings were made. The fluctuations were well above those for plain medium without bacteria and was considered to be occurring due to the activity of the bacteria in the suspension. Figure (3.2(a)) shows the position-time (X - t) data for cantilever deflections in plain medium, tumblers and swimmers. Both the strains are at a volume fraction of 8.4×10^{-4}. It can be seen that from control to tumblers to swimmers the amplitude of fluctuations goes up. Figure (3.2(b)) shows a zoomed in view of the same. The Occasional large amplitude fluctuations are exhibited by swimmers, while the behaviour of tumblers appears by and large comparable to that of control but with larger amplitude. The standard deviation σ (defined later) of these distributions increases steadily from control to swimmers.

Also we calculated Kurtosis (β_2), which shows the degree of peakedness of a distribution, defined as a normalized form of the fourth central moment of a distribution.

$$\beta_2 = \frac{1}{\sigma^4 N}\sum_{i=1}^{N}(X_i - \bar{X})^4 \tag{3.1}$$

where

$$\sigma^2 = \frac{1}{N}\sum_{i=1}^{N}(X_i - \bar{X})^2 \tag{3.2}$$

and

$$\bar{X} = \frac{1}{N}\sum_{i=1}^{N} X_i \tag{3.3}$$

Its value is 3 for a normal distribution and higher values indicate larger probability of abrupt larger fluctuations. Kurtosis was calculated for the distributions of all

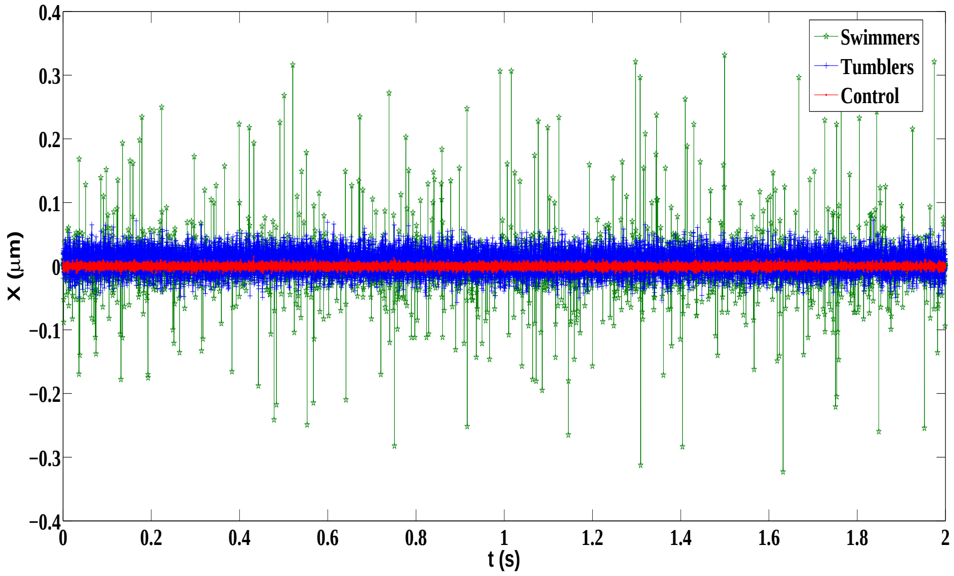

(a)

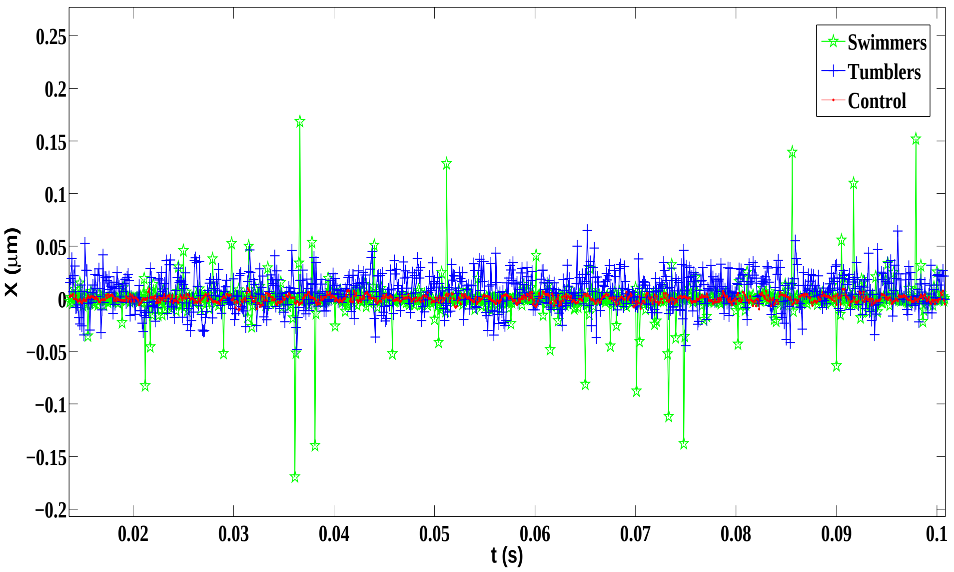

(b)

FIGURE 3.2: (a) Position-time plot of cantilever tip in plain medium (red), tumbling bacteria (blue) and in swimmers (green). The bacterial baths are at a volume fraction of 8.4×10^{-4}. It can be seen that from control to tumblers to swimmers the amplitude of fluctuations goes up. (b) Zoom of a small portion of plot (a). Occasional large amplitude fluctuation can be seen in swimmers, while the behaviour of tumblers appears by and large comparable to that of control but with larger amplitude.

.

the strains we used and it was found that for control and tumblers it is close to 3 and it is about 8 for the wild type and about 60 for the swimmers.

The results clearly indicate that the experimental setup can sense the effect of bacterial activity and also that the nature of the strain influences the distribution of these fluctuations.

3.3.1 Action of Sodium azide on Bacterial activity

To confirm that the increase in the fluctuations in cantilever position and in kurtosis are due to the bacterial activity, we performed an experiment wherein, we gradually decreased the bacterial activity while monitoring the cantilever fluctuations. Sodium azide is a drug that interferes with the ATP hydrolysis and hence decreases the energy release in the cells [105]. Therefore, the bacterial activity decreases gradually with time due to the action of Sodium azide on Bacterial cells. Bath was prepared with wild type bacteria, a drop of 0.02% Sodium azide was added to the bacterial suspension and tip of the cantilever was recorded using Andor Luca camera at 10Hz under the same conditions as mentioned in the above experiments. The results shown in figure (3.3) confirm that the bacterial activity is responsible for the deviation in σ and β_2. A dead suspension shows expected passive response with gaussian profile.

Next we study specific bacterial strains as a function of their volume fraction in the medium.

3.3.2 Experiments on RP-1616 (Tumblers)

First control experiments were performed using plain medium without bacteria and cantilever position was recorded with time. Then the plain medium was replaced by bacterial solution and similar recordings were made. The experimental protocol is same as described in the above section. Position time data for cantilever deflections were obtained for each strain at six densities. Figure (3.4) shows the histograms for the position data of tumblers and control experiment. We see that the standard deviation increases with density of bacterial suspension and kurtosis remains close to 3. Table (3.1) gives the values of σ and β_2 for different densities of tumblers used.

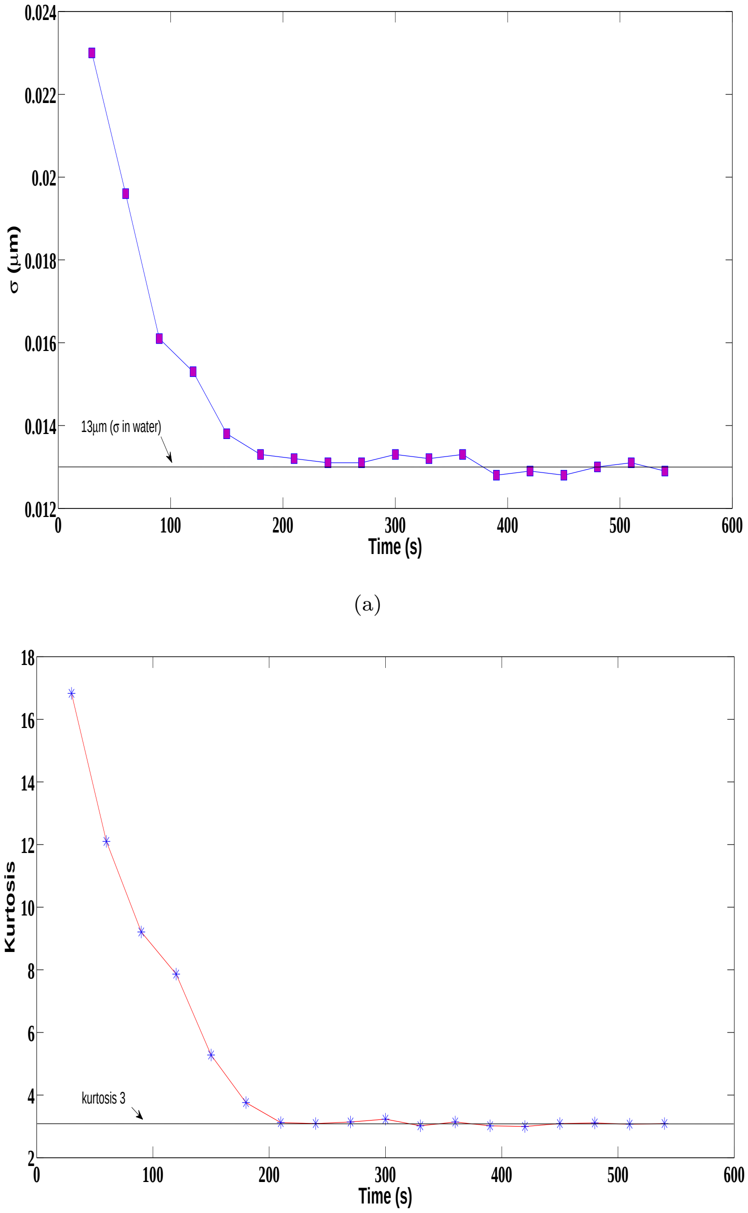

(a)

(b)

FIGURE 3.3: Effect if a depressant on bacterial activity. Sodium azide was added to the bacterial solution and cantilever tip position is monitored with time. (a) Systematic decrease in standard deviation show that, the fluctuations that are large as compared to those seen in plain medium, are likely due to bacterial activity. It is to be noted that the standard deviation approaches a value near $12 - 13$ nm and remains around there which is the typical value in water for the dimensions of the cantilever used. (b) Decrease in the value of kurtosis from around 20 to that about 3 and continuation there indicates the decrease in rare events and restoration of Gaussian behaviour as in the case of water.

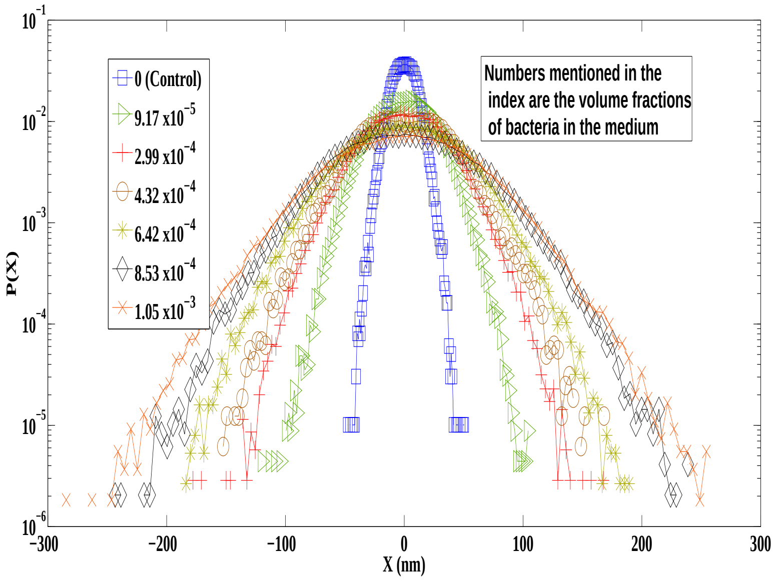

Figure 3.4: Probability densities of the position data for tumblers. The innermost histogram (squares) shows the distribution for control experiment and rest in the increasing order of density. In case of control experiment the standard deviation of the position data is about 10.5nm and in the presence of bacterial cells the standard deviations increase from about 24nm to about 56nm for the volume fractions of samples used.

Table 3.1: Values of σ and β_2 for different volume fractions in tumblers

Volume fraction	σ (nm)	β_2
0	12.80	3.04
9.17×10^{-5}	24.09	2.96
2.99×10^{-4}	32.54	3.06
4.32×10^{-4}	36.38	3.14
6.42×10^{-4}	43.91	3.03
8.53×10^{-4}	49.31	3.25
1.05×10^{-3}	55.89	3.26

3.3.3 Calculation of effective temperature

One useful parameter we can directly measure and verify independently is the ‘effective local temperature’ of the medium and effect of bacterial activity on this parameter. This can be done for tumblers as the distribution remains gaussian.

The measurements show that this quantity increase with the density of the tumblers. This force device therefore can be a good means of measuring this quantity directly.

Position data recorded using QPD is processed using home built MATLAB programs. Probability densities of the data are plotted and the parameters like standard deviation,variance and kurtosis are computed.

Effective temperature was calculated using the expression [106]

$$\frac{1}{2}k_BT = \frac{1}{2}k\sigma^2 \tag{3.4}$$

where $k_B = 1.38 \times 10^{-23} JK^{-1}$, k is the spring constant calculated as $k = 6.2515 \times 10^{-5}(\frac{d^4}{l^3})$, d and l being diameter and length of the cantilever respectively.

The numerical constant in the expression for the spring constant is computed from the measured Young's modulus of the cantilever material using the static method (86.8GPa) and the density of the cantilever material ($2.3 \times 10^3 kgm^{-3}$). σ^2 is the variance of the position data. For these experiments $l = 21$mm and $d = 8.9\mu$m.

In case of control experiments where no bacteria is present, the standard deviation of the position data is about 10.5nm which gives the variance as $1.102 \times 10^{-16} m^2$. Plugging in these values the temperature T works out to be around 320K. The scatter in this data is about 20K for different realisations. This could be due to the error in detection which results in a higher σ^2. Similarly in the presence of bacterial cells the standard deviations increase from about 24nm to about 56nm for the volume fractions of samples used. With these values and the spring constant of the cantilever the effective temperature can be calculated using the expression (3.4).

It can be seen from figure(3.5) that the effective temperature increases with density. In the absence of bacterial cells the value is about 320K. In the presence of bacterial cells, the value starts at about 1800K for the smallest volume fraction used (9.17×10^{-5}) and reaches about 10^4K for the highest used value (1.05×10^{-3}).

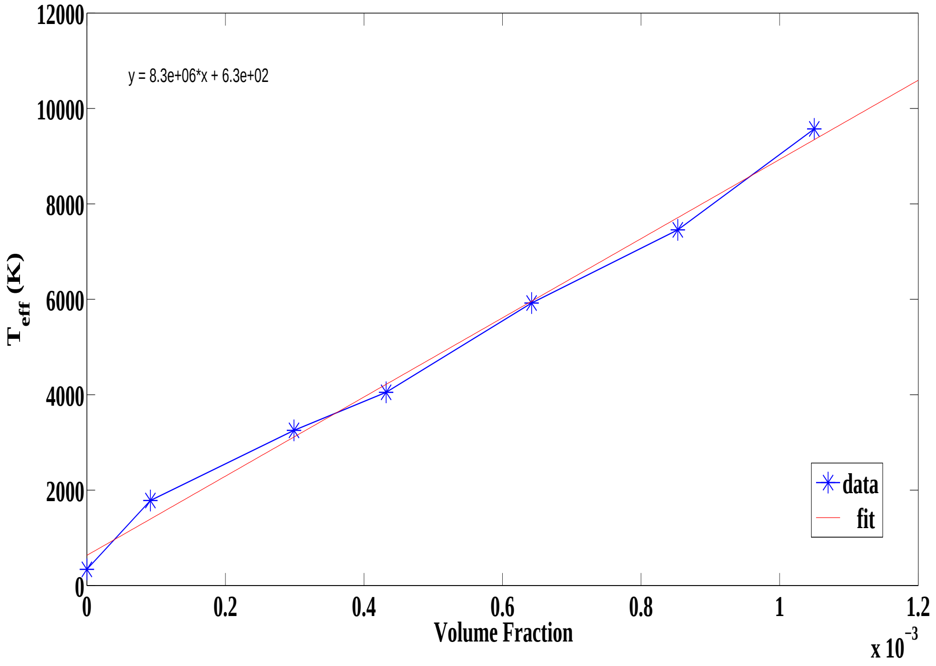

FIGURE 3.5: Effective temperature plotted against bacterial density as calculated from the equation (3.4). The first point at zero density indicates the temperature from control experiment without bacteria. The value for this point is 320 K. In the presence of tumblers the value starts at about 1800K for the smallest volume fraction used (9.17×10^{-5}) and reaches about 10000K for the highest density used (1.05×10^{-3}.)

Figure (3.6) shows the collapse of the distributions plotted in in figure(3.4) when normalized with $T^{1/2}$. This collapse confirms the scaling of the 'effective temperature' with density.

3.3.4 Experiments on RP-437 (Wild Type)

Cantilever based experiments performed on the wild type (RP-437) give distributions which are gaussian distribution with exponential tails. Figure (3.7) shows the distributions of the cantilever position in the bath of wild type bacteria. The inner most curve represents the control without bacteria and the remaining distributions correspond to those in the order of increasing density. With the increase in density the width of the distribution continued to increase but the shape remained similar indicating, the scaling of the amplitude of cantilever fluctuations with density while the nature of the effect of the activity remaining the same.

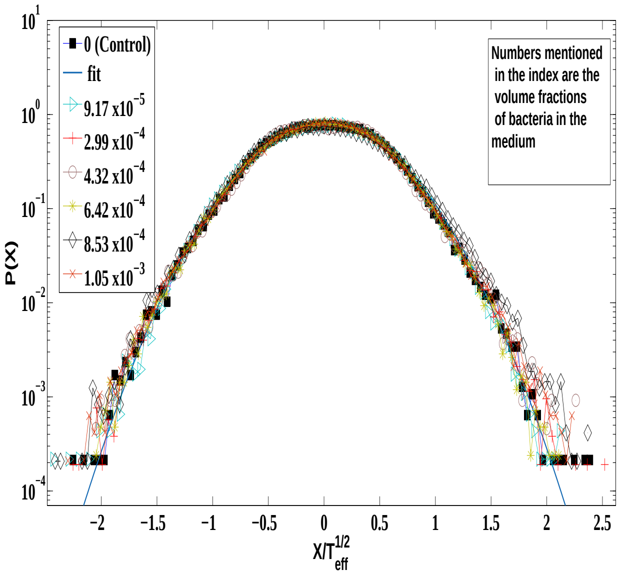

Figure 3.6: Collapse of pdfs, of tumblers of all the densities used, after normalisation with $T_{eff}^{1/2}$ and fit to Gaussian.

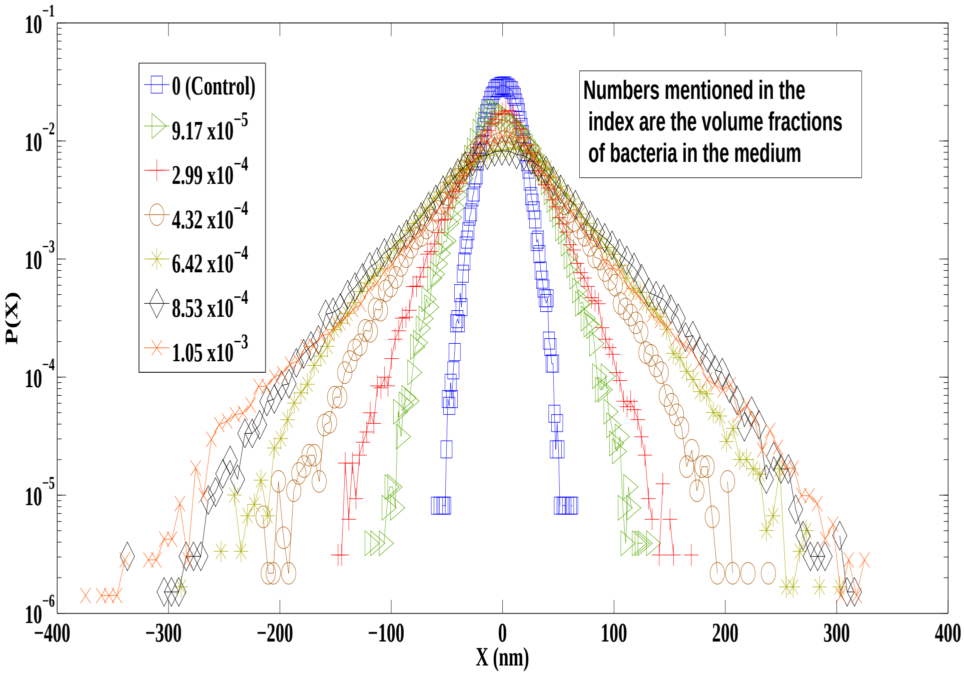

Figure 3.7: Probability densities of the position data for the wild type. The innermost histogram (squares) shows the distribution for control experiment and rest in the increasing order of density. It can be noticed that these distributions show gaussian profile with but show exponential fall off.

The kurtosis values for this strain are not close to 3 but vary between $4-9$. Table (3.2) gives the values of σ and β_2 for all the densities of wild type used.

Table 3.2: Values of σ and β_2 for different volume fractions in wild type

Volume fraction	σ (nm)	β_2
0	12.80	3.04
9.17×10^{-5}	23.11	3.74
2.99×10^{-4}	28.76	4.41
4.32×10^{-4}	41.40	4.80
6.42×10^{-4}	48.1	4.61
8.53×10^{-4}	55.92	4.83
1.05×10^{-3}	60.30	7.36

3.3.5 Experiments on RP-5232 (Swimmers)

The Probability distributions of the cantilever in the strain RP-5232, the predominant swimmers, show large scale deviation from gaussian profile and exhibit a large value of kurtosis in the range of $10 - 100$. Once again the amplitude of fluctuations increased with the increasing density in the observed range. This large deviation from ideal gaussian behaviour could be due to interactions of swimming cells with cantilever via the medium as well as direct collisions of these cells with the cantilever. Figure (3.8) shows the distributions of the cantilever position in the bath of swimmers.

Table (3.2) provides the values of σ and β_2 for all the densities of wild type used.

3.3.6 Conclusions from cantilever based experiments

The position distributions of the cantilever in the presence of tumblers showed a gaussian behaviour and the width of the distribution increased with increasing

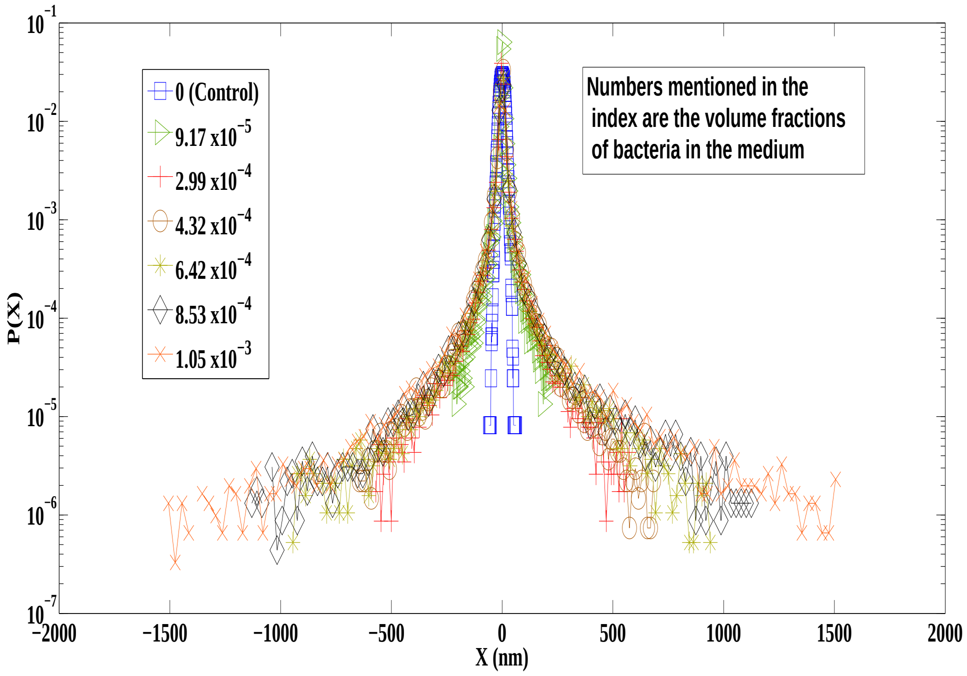

FIGURE 3.8: Probability densities of the position data for the swimmers. The innermost histogram (squares) shows the distribution for control experiment and rest in the increasing order of density. The distributions exhibit large deviations from gaussian behaviour and show a power law fall with an exponent close to −1.5 .

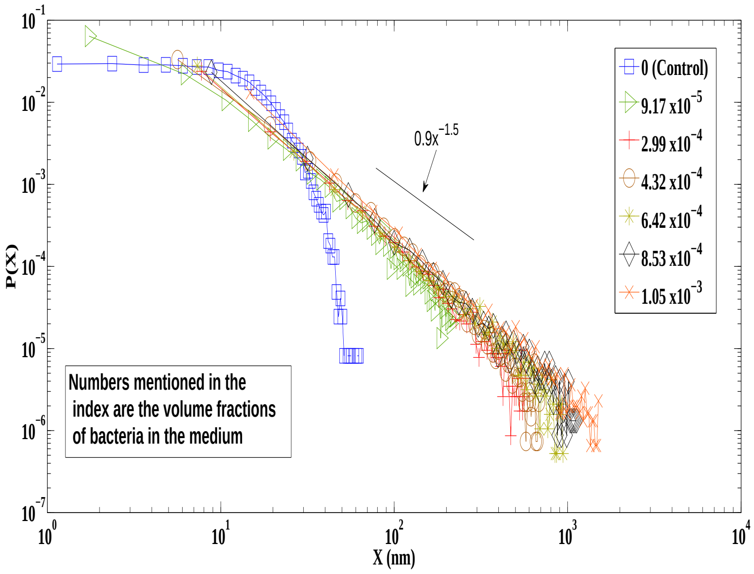

FIGURE 3.9: log-log plot of Probability densities of the position data for the swimmers. The innermost histogram (squares) shows the distribution for control experiment and rest in the increasing order of density. The distributions exhibit large deviations from gaussian behaviour and show a power law fall with an exponent close to −1.5.

density. This observation indicates that the interaction of the tumblers with cantilever can be considered as stochastic gaussian noise. Therefore,we can define an

Table 3.3: Values of σ and β_2 for different volume fractions in swimmers

Volume fraction	σ (nm)	β_2
0	12.80	3.04
9.17×10^{-5}	24.18	25.72
2.99×10^{-4}	40.41	54.42
4.32×10^{-4}	47.40	52.31
6.42×10^{-4}	55.18	85.63
8.53×10^{-4}	67.46	86.65
1.05×10^{-3}	87.52	92.02

'effective temperature' which is a measure of bacterial activity. The effective temperature increased linearly with the density and is found close to two orders larger as compared to the room temperature. In case of wild type bacteria, the position distributions of cantilever fluctuations show deviations from gaussian behaviour with exponentially falling off tails. The distributions of cantilever in the presence of swimmers are far from gaussian profile, with heavy tails exhibiting a power law fall with an exponent close to -1.5.

3.4 Particle tracking experiments

After performing experiments using cantilever as probe, we went ahead to carry out particle tracking experiments, using the three bacterial strains.

These experiments were similar to those mentioned in the literature [52, 100–102]. In this set of experiments carboxylate modified micro-spheres (Flospheres,F-8888, Life technologies, USA) were used as probes. The micro spheres of 2μm diameter with a poly-dispersity less than 0.02 were embedded in the bacterial baths and tracked in 2-dimensions. The nature of motion of the bead was used to understand the activity of bacterial cells.

Experimental chambers were prepared using BSA treated cover glasses and Parafilm spacers with a circular hole of 3mm diameter and about 100μm depth. The beads were diluted in Millipore water, sonicated, washed with the medium and then suspended in the baths at known lower densities. The suspension of bacteria with infused beads was the sample for these set of experiments. Once the sample was filled in, the chambers were sealed using vacuum grease to arrest evaporation and external disturbances. Experiments were performed within 15-20 minutes of preparation of sealed chambers. As there were free particles, a QPD could not be used due to its limited spatial range. Observations were made at 10Hz frame rate using the CCD camera. From the recorded image sequences, particle tracking was performed using a home built MATLAB program with a resolution of few nm.

As in case of cantilever based experiments, particle tracking experiments were also performed on all the three strains.

3.4.1 Experiments on RP-1616 (Tumblers)

For control experiments, medium without bacteria was used and motion of the beads was recorded using camera and position time data of beads were obtained. Later the medium was replaced with bacterial bath containing tumblers and similar observations were made for bead positions at different densities of bacterial suspension. The densities of the bacteria used in this set of experiments were same as those used in cantilever based experiments. From the position time data Mean Square Displacement (MSD) was computed and plotted against lag time. Figure (3.10)shows the MSD of the beads in plain medium and tumblers as a function of time. Plots corresponding to every volume fraction represent the average of 5 runs. It can be seen that for control as well as tumblers MSD vs time plots are linear for low densities. Only at the highest density the plot deviated from linear behaviour. The relation between MSD and time is $< r^2(t) >= 4Dt$. When the power law is close to 1, the nature of motion of the bead can be taken as diffusion. Using the slope of the MSD vs time plots the diffusion coefficient ’D’ can be calculated. From the value of ‘D’, the ‘effective temperature’ is estimated.

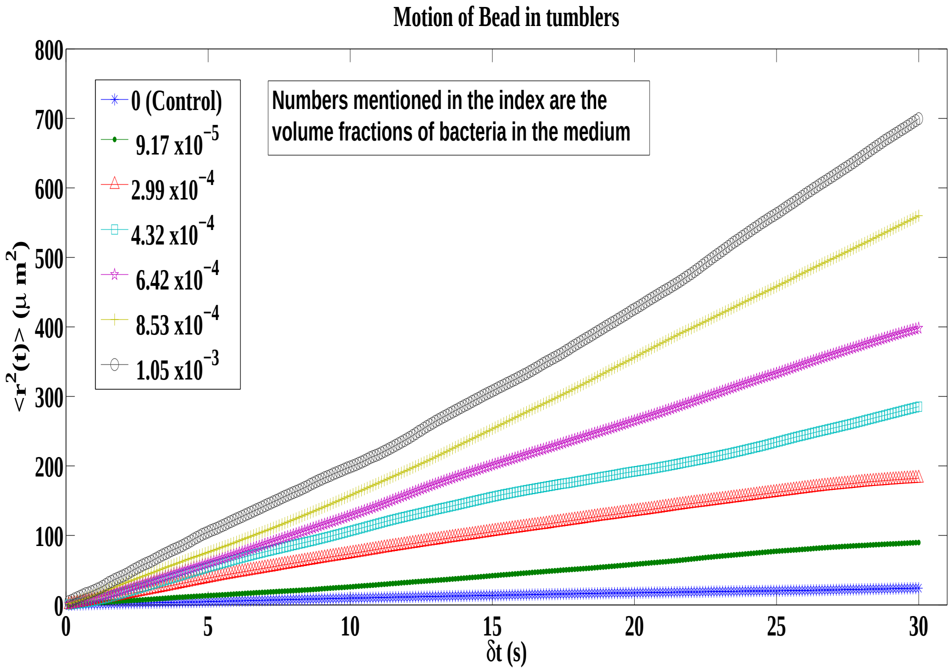

(a)

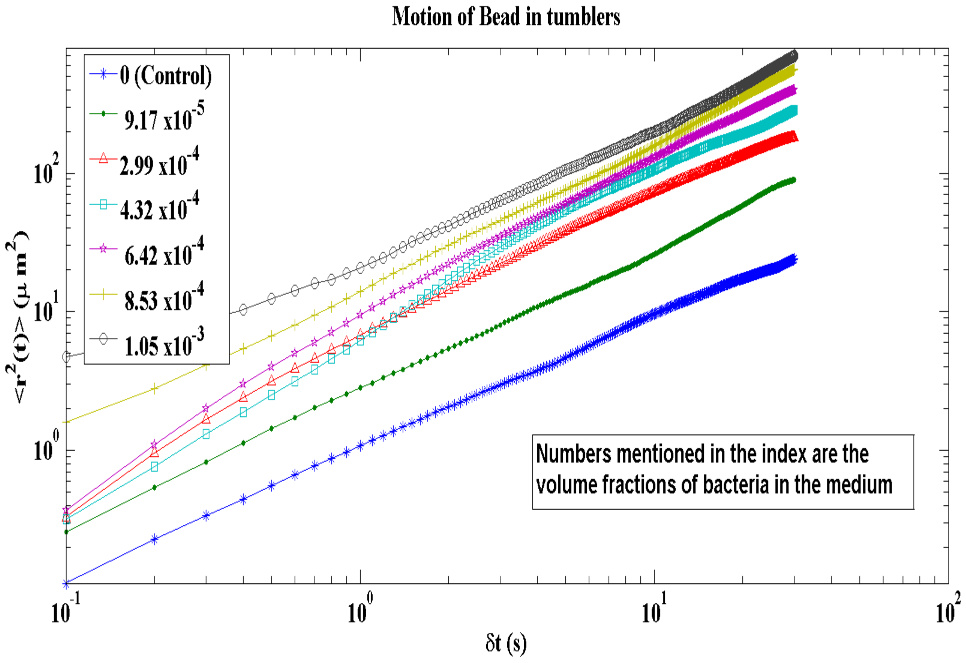

(b)

Figure 3.10: (a) Mean square displacement of bead plotted against time. The blue line with smallest slope corresponds to control experiment without bacteria. With the increase in bacterial density the slope increases indicating an increase in effective temperature. At higher densities the dependence deviates from linear behaviour as can be seen for the density of 1.05×10^{-3}. (b) log-log version of the plot shown in (a)

3.5 Calculation of temperature

Position-time data of the tracked bead is processed to get mean square displacement (MSD) vs time. For a quasi two dimensional system this relation can be written as

$$< r^2(t) >= 4Dt \tag{3.5}$$

where D is the diffusion coefficient given by

$$D = \frac{k_B T}{6\pi\eta a} \tag{3.6}$$

The slope of the plot of MSD vs time gives $4D$ and temperature is computed from this slope and $\eta = 0.9 \times 10^{-3} Pa.s$ (viscosity of water at the given temperature) and $a = 1 \times 10^{-6} m$ (bead radius). The effective temperature calculated for control experiments, averaging over 40 realisations, is around 440K which is about a factor of 1.5 higher than the room temperature and about 1.3 times that of temperature obtained from cantilever experiment. The effective temperatures obtained from particle tracking experiments for control and the six densities of tumblers are shown in figure (3.11). It can be seen that the trend of increase in effective temperature with increasing density is the same, as in cantilever case. In the absence of bacterial cells the value is about 440K. In the presence of bacterial cells, the value starts at about 1900K for the smallest volume fraction used (9.17×10^{-5}) and reaches about 12300K for the highest used value(1.05×10^{-3}). The above expression is computed for a two dimensional case, as we imaged a projection of the trajectory of the beads and the information to compute $< r^2(t) >$ comes from x and y position data of the camera.

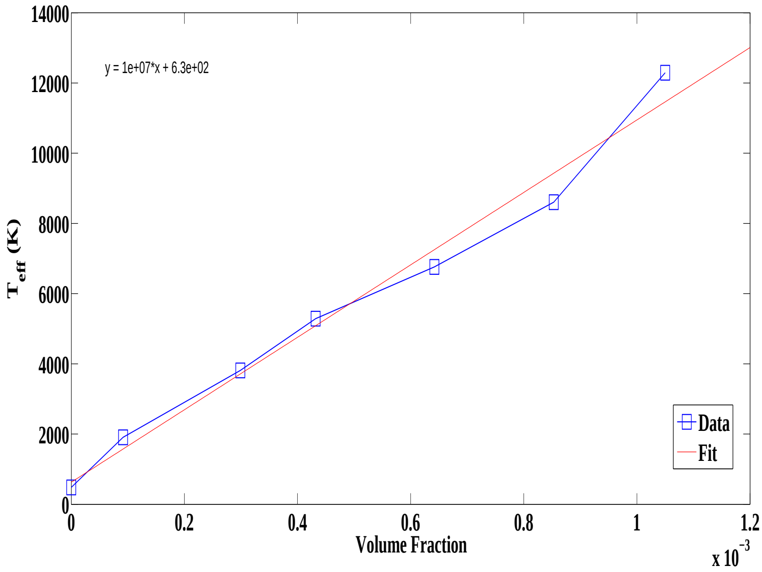

FIGURE 3.11: Effective temperature plotted against bacterial density as calculated from the equation (3.5). The first point at zero density indicates the temperature from control experiment without bacteria. The value for this point is about 440K. In the presence of tumblers the value starts at about 1900K for the smallest volume fraction used (9.17×10^{-5}) and reaches about 12300K for the highest density used (1.05×10^{-3}).

Figure (3.12) shows MSD vs time for tumblers after normalising with the effective temperature.

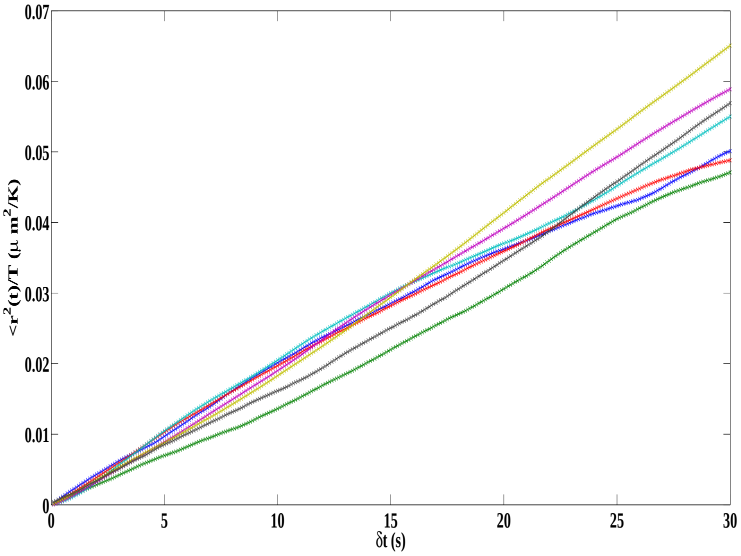

FIGURE 3.12: MSD vs time for all the densities of tumblers normalised with Effective temperature T_{eff}

The increase in effective temperature as a function of bacterial density could be attributed to the activity of these cells. Using our force set up, direct measurement of these quantities becomes a possibility and the results can be compared with those of particle tracking experiments with reasonable agreement as discussed later.

3.5.1 Experiments on RP-437 (Wild Type)

Following the same experimental protocols as was used for tumblers, particle tracking experiments were performed using wild type, RP-437 cells. Observations are shown in figure (3.13). Mean square displacement of beads vs time plot shows a non-linear trend for all the densities. This trend indicates departure from diffusive behaviour. The power law varies from 1.3 for the smallest density to 1.9 for the highest.

3.5.2 Experiments on RP-5232 (Swimmers)

In case of swimmers the mean square displacement vs time plots show, the non linear trend with greater slopes up to about 10 seconds of observation and beyond that, the behaviour follows no particular trend. The motion appears to be erratic, shifting between super diffusive and sub diffusive patterns. Figure (3.14) shows the MSD vs time plots for all the densities of swimmers including control experiment.

3.5.3 Conclusions from particle tracking experiments

We showed that the bead motion in tumbler is nearly diffusive and the effective temperature obtained from MSD - time plots show the same trend as those corresponding to cantilever experiments.

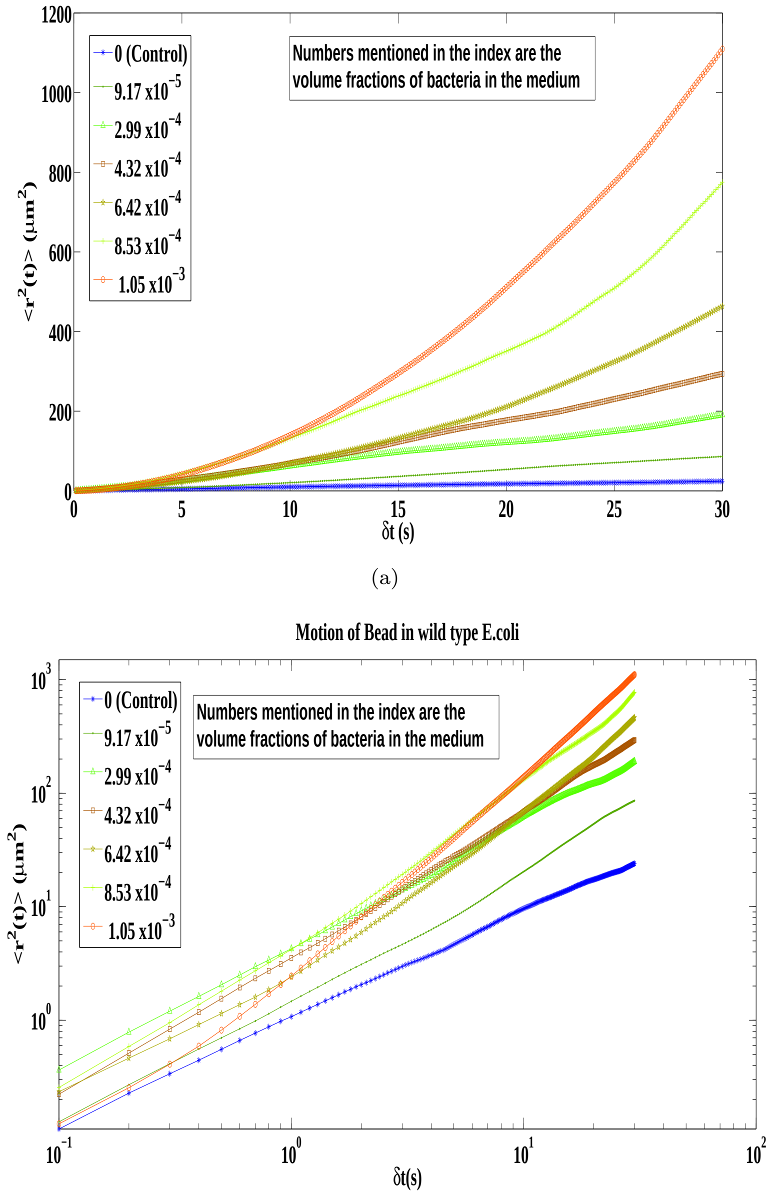

(a)

(b)

FIGURE 3.13: (a) Mean square displacement of bead plotted against time. The blue line with smallest slope corresponds to control experiment without bacteria. For the runs with wild type cells the power law varies from 1.3 for the smallest density to 1.9 for the highest. (b) log-log version of the plot shown in (a)

Previous works comparing the diffusion coefficient for different strains at a given density, presented the MSD - time data for 10 seconds or less [100, 102]. We present the data for longer duration where we see dramatic change in the behaviour of bead motion particularly in case of swimmers. We observe that the diffusion coefficient 'D' of the bead motion in the presence of bacterial cells,increases with volume

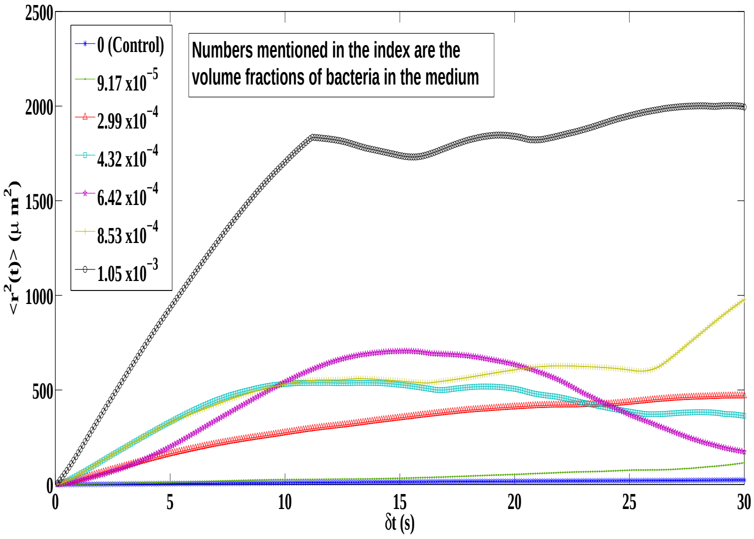

(a)

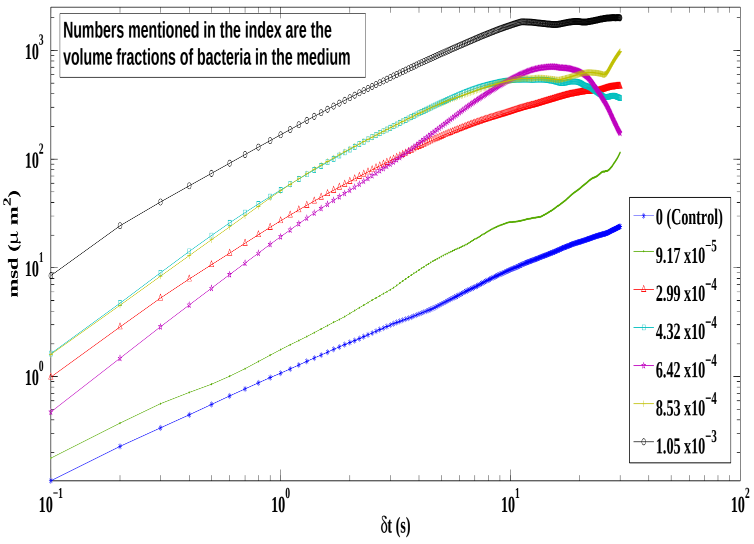

(b)

FIGURE 3.14: (a) Mean square displacement of bead plotted against time. The blue line with smallest slope corresponds to control experiment without bacteria. It can be seen that beyond 10seconds the behaviour turns erratic and no particular trend is followed. (b) log-log version of the plot shown in (a).

fraction of the bacteria for any strain. At a given density value of 'D' is maximum for the bead motion in the presence of swimmers followed by wild type and least for the bath of tumblers. Understanding these anomalous behaviour at longer time scales and exploring the underlying physics is being included in the future work plan.

3.6 Discussion

We started with looking at the influence of bacterial cells, at a known density, on the fluctuations of the cantilever. Figure (3.15) shows the distributions for the position data of cantilever in medium without bacteria and medium with different strains of bacteria at a volume fraction of 8.4×10^{-4}. We see that the distributions of cantilever fluctuations in the control medium and the tumblers are gaussian, while that of wild type shows gaussian profile with exponentially falling tails. Distributions corresponding to cantilever fluctuations in swimmers exhibit large deviation from gaussian profile showing power law fall off with an exponent close to -1.5. The standard deviation of these distributions increases steadily from control to swimmers. Kurtosis, was found be close to 3 for control and tumblers, about 8 for the wild type and about 60 for the swimmers on the average.

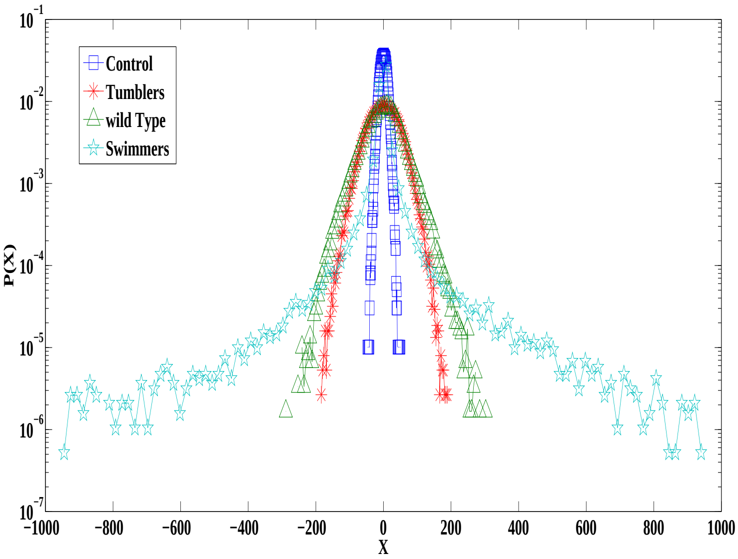

FIGURE 3.15: Distributions for the position data of cantilever in medium without bacteria and medium with different strains of bacteria at a volume fraction of 8.4×10^{-4}. We see that the distribution for plain medium and tumblers shows a gaussian while that of wild type shows distorted gaussian and that of swimmers exhibit large deviation from gaussian behaviour and the tails fall off with a power law close to -1.5. The standard deviation of these distributions increases steadily from control to swimmers.

Then we tried to measure and compare the effective temperature of tumbling strain as a function of the density using both cantilever based experiments and particle tracking experiments. We see good agreement in the trend of variation of effective temperature with density from the two independent modes of experiments.

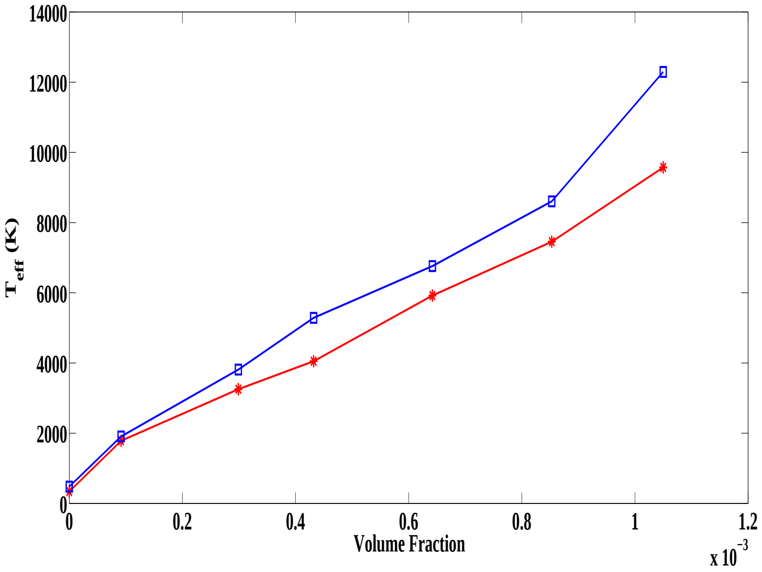

FIGURE 3.16: Effective temperature plotted against bacterial density as calculated from the equations (3.4) and (3.5). The first point at zero density indicates the temperature from control experiment without bacteria. The value for this point is 328 K in case of cantilever experiments and about 450 K for bead tracking experiments. It can be seen that there is a good agreement in the trend of change in temperature with density from both the measurements.

Experiments were performed on the remaining two strains,the wild type and the swimmers. Detailed analysis for these strains is to be worked out as apart of future perspective. As the position distributions of cantilever in wild type bacteria and swimmers deviate largely from gaussian behaviour, more experiments and involved theoretical framework could be required to understand the effect of activity of these strains on cantilever fluctuations. This work is excluded from the scope of this thesis and is intended to be pursued in the coming future.

As a part of applications of the device, we performed experiments that are technologically advanced in the field of active particle dynamics. These type of experiments are of their kind in the interface of non-equilibrium statistical physics and hydrodynamics. Our device has definite advantages over techniques like optical tweezers for these type of experiments. With optical tweezers, often the cells under observation get trapped along with the beads, sample can suffer heating effects in the presence of direct lasers, where as in our case a BSA coated cantilever can sense the forces exerted by the bacteria mechanically without the bacterial cells adhering to the cantilever.

These types of experiments open up the possibility of investigating challenging problems in the less explored fields like the interface of non-equilibrium statistical physics and hydrodynamics. These areas, mainly explored by theories and simulations can get richer by the state of art experiments like those ours and shed light on several aspects of self propelled systems.

Chapter 4

Extensional rheology at micro-scale

4.1 Introduction

Rheology can be broadly defined as the study of flow and deformation of matter. Two types of flows with relative motion of adjacent particles in a fluid are usually studied in rheology. If the liquid elements flow over or past each other we call it a shear flow and if the adjacent fluid elements flow towards or away from each other it is termed as extensional flow [107]. See figure (4.1) for illustrations of shear and extensional deformation and flow respectively

4.1.1 Some important definitions

Shear stress (σ), Shear (γ) and Shear rate ($\dot{\gamma}$) and their counter parts, extensional stress (σ_e), extensional strain (ϵ) and extensional strain rate ($\dot{\epsilon}$) are the important parameters that characterise shear and uni-axial extensional flows respectively. Figure (4.2) illustrates the definitions of all the above parameters. When the fluid is subjected to the force F, on its surface with an area A, a velocity V is developed in that layer of the fluid due to the applied force F. δ is the deformation in shear

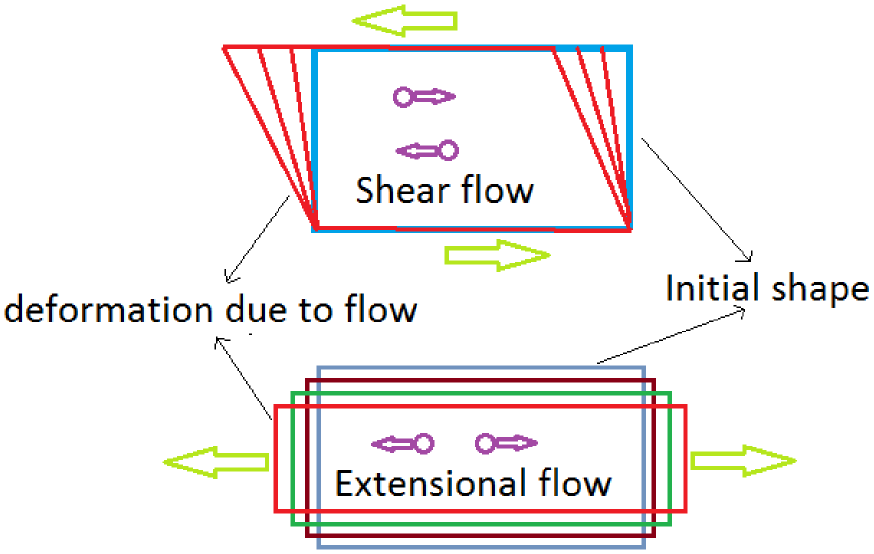

FIGURE 4.1: Schematic depicting shear and uni-axial extensional flows. In shear flow the adjacent fluid elements flow over or past each other while in extensional flow they move towards or away from each other. It can be seen that a hypothetical rectangular fluid sheet under shear flow deforms to parallelogram while under extensional flow it deforms to a rectangle with larger aspect ratio (Figure adapted from 'A handbook of elementary rheology, Howard A. Barnes, 2000)

flow and elongation in uni-axial extensional flow. Knowing F, V and δ, we get the required definitions for shear and extensional flows.

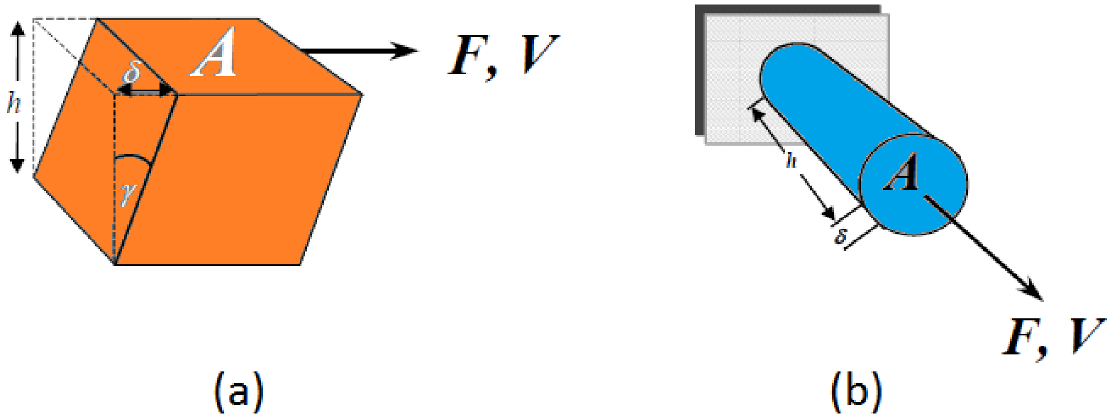

FIGURE 4.2: Schematic illustrating definitions of basic parameters in shear and uni-axial extensional flows. When the fluid is subjected to the force F, on its surface with an area A, a velocity V is developed in that layer of the fluid due to the applied force F. δ is the deformation in shear flow and elongation in uni-axial extensional flow. (Figure adapted from 'A handbook of elementary rheology, Howard A. Barnes, 2000')

$$\sigma = \frac{F}{A} \qquad\qquad \sigma_e = \frac{F}{A} \tag{4.1}$$

$$\gamma = \frac{\delta}{h} \qquad\qquad \epsilon = \frac{\delta}{h} \tag{4.2}$$

$$\dot{\gamma} = \frac{V}{h} \qquad\qquad \dot{\epsilon} = \frac{V}{h} \tag{4.3}$$

stress developed in the material under flow would be $\sigma = \frac{F}{A}$ and the viscosity of a material is defined as the ratio of stress and strain rate

$$\eta = \frac{\sigma}{V/h} \tag{4.4}$$

for small rates of uni-axial extension and shear the corresponding uni-axial extensional viscosity η_E and the shear viscosity η are related as

$$\lim_{\dot{\epsilon}\to 0} \eta_E(\dot{\epsilon}) = 3 \lim_{\dot{\gamma}\to 0} \eta(\dot{\gamma}) \tag{4.5}$$

This relation is universally true for any liquid irrespective it being Newtonian, non-Newtonian, visco-elastic etc. For higher values of shear and extensional rates this relation is not readily applicable and depending upon the situation the ratio η_E/η, which is called Trouton ratio, can be very large [107].

Apart from uni-axial extension there can be two other types of extensional flow, namely the bi-axial extension and the planar extension

Bi-axial extension: In this type of extensional flow a liquid sheet is stretched in two directions while it undergoes compression along the third direction as the thickness of the element decreases. This is the kind of deformation experienced by a portion of a balloon or a bubble being inflated.

Planar extension: In planar extensional flow a liquid sheet undergoes stretching along one direction and compression another direction while the third direction remains unaffected. For example, when a long cylinder is inflated, the stretching only takes place in one direction, but the thickness of the sample decreases, with the third dimension unaffected.

The figure (4.3) illustrates the different modes of extensional flow.

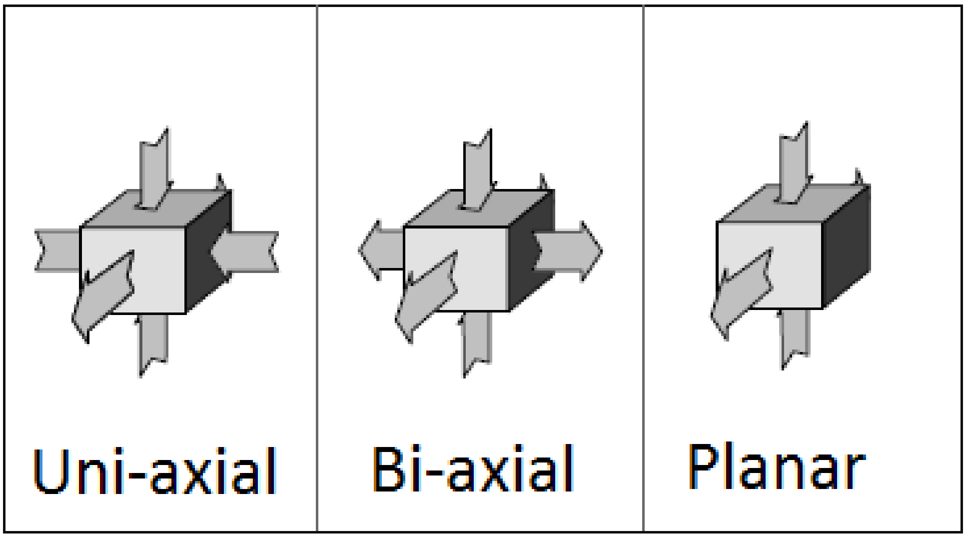

FIGURE 4.3: Schematic illustrating uni-axial, bi-axial and planar extensional flows.(Figure adapted from 'A handbook of elementary rheology, Howard A. Barnes, 2000')

4.2 Extensional rheology

Many real fluids in everyday life are subjected to extensional flows for various purposes and for some of these fluids there can be a very large difference between their shear and extensional viscosities. Below mentioned are some of the applications of extensional flows. See the reference [107].

1. Flow into and out of orifices

2. Break-up of liquid jets, droplet break-up, atomisation and spraying

3. Expanding bubbles, in foam and doughs

3. Atomisation (misting) in coating and printing operations

4. Drinking through a straw (entry flow) and swallowing

5. Blow-moulding and other inflation operations for plastic components

6. Man-made fibre spinning, and spinning spider webs

7. Flow through porous media, and some rapid squeezing, forming and stamping operations.

In the above mentioned situations extension rates can be obtained by finding the appropriate velocity gradient along the flow direction. As already mentioned, in cases where the strain rates are large, the shear and the extensional viscosities can be different by orders of magnitude. It is to be note that the equation (4.5) hold good only for infinitesimally small rates of shear and extension. We would like to explain the importance of extensional rheology with the help of a few examples narrated in the following subsections.

4.2.1 Liquids with suspended fibres

One good example to mark the striking difference between shear and extensional viscosities is a Newtonian liquid with a single fibre suspended within the liquid. “If the liquid with the suspended fibre is subjected to a shear flow, the fibre will align along the flow axis, and then the disturbance it presents to the surrounding liquid is a minimum. On the other hand, if the same suspended fibre is subjected to an extensional flow, it again aligns, but now the resistance it presents to the flow is maximised, since the liquid being stretched tries in turn to stretch the fibre. This is reflected in the viscosity of a suspension made up of such suspended fibres in which the viscosity will decrease as a flow aligns the fibre in shear flow, but will increase the viscosity as it aligns in extensional flow."[107].

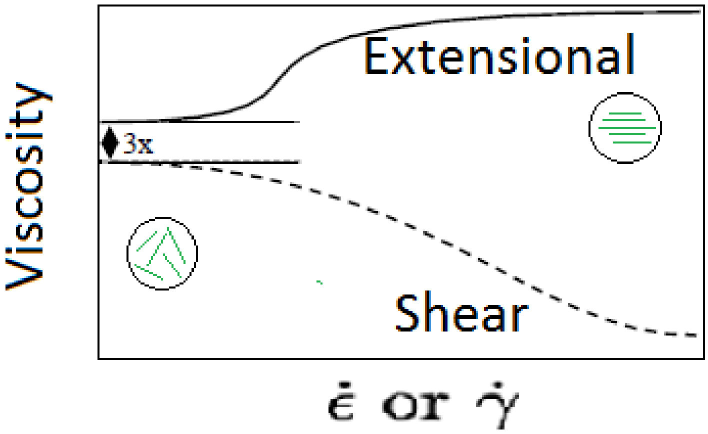

Figure 4.4: Illustration of difference between shear and extensional flows. Rigid fibres are suspended in a Newtonian liquid. Dotted line shows the effect of shear flow and the solid line the effect of extensional flow. It can be seen that while the viscosity of the liquid with suspended fibre decreases with increasing shear rate the extensional viscosity increases for increasing extensional strain rate. (Figure adapted from 'A handbook of elementary rheology, Howard A. Barnes, 2000')

4.2.2 Coil-stretch transitions

As another example to demonstrate the stark difference in viscosity under shear and extensional flows, we consider dilute solutions of high molecular weight polymers. The isolated individual polymer coils influence their properties. At low shear and extensional rates, the polymer chains are coiled in a loose spherical shape, and the viscosity of the solution is low. But after a critical rate of extensional strain, the polymers unwind suddenly to form long stretched strings. This is called the coil-stretch transition. As a result of unwinding, the polymer string starts offering large extensional resistance. The extensional viscosity increases dramatically and this increase can be several thousands of times higher than the corresponding viscosity under shear flow.

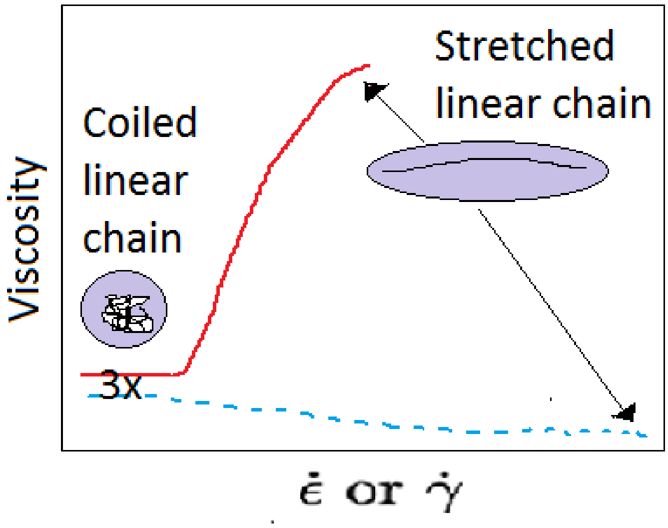

FIGURE 4.5: Difference between shear and extensional viscosities after coil stretch transition.After the coil is unwound into linear string it offers enormous resistance to extensional flow increasing the extensional viscosity of the solution. Dotted line shows the effect of shear flow and the solid line the effect of extensional flow. It can be seen that while the viscosity of the solution decreases with increasing shear rate the extensional viscosity increases drastically for increasing extensional strain rate.(Figure adapted from 'A handbook of elementary rheology, Howard A. Barnes, 2000)

4.2.3 Fibre spinning

Fibre spinning is one of the widely used industrial applications of polymer processing which uses extensional flows. It can be shown in this context that extensional rheological properties play a very important role in 'spinnability' of the chosen polymer material. The material under consideration can be either extension-thickening or extension thinning owing to its properties. One of the requisite conditions for spinning is that the spun thread remains stable and does not snap. During the spinning process there can be instances, where due to some technical reasons the diameter of the fibre undergoes a change. If the material is extension-thinning, the extensional strain rate starts growing in the narrower part of the fibre, the resistance to the flow decreases and ultimately the fibre snaps. On the other hand if the material is extension-thickening, the resistance to the flow grows with the increasing rate of extension, the flow in the filament slows down and the diameter could be recovered to that of remaining part of the fibre. In this case the extension-thickening works as stabilising agent. Therefore, a priory knowledge of extensional flow properties of the material plays a vital role in its processing.

Above narrated situations are a few among several applications where, knowledge of behaviour of materials under extensional flow is very important. Although extensional properties are pivotal in several situations, the field remained less explored experimentally owing to the challenges in the process of measuring the extensional flow parameters some of which we will discuss later.

4.3 Extensional Rheometers

As already discussed, extensional properties of materials are important because extensional modes of deformation are obtained in a wide variety of industrial and laboratory settings, including tensile testing of materials, flow from an orifice, fibre-spinning of a thread, atomization involving breakup of liquid jets, flow through porous media, stagnation-point flows among others. In the field of extensional rheology [32–34], some widely used methods for the study of materials such as polymer melts and solutions involve devices such as the Filament Stretching Extensional Rheometer (FiSER) [35, 36], the Capillary Breakup Extensional Rheometer (CaBER) [37, 38], Meissner-type elongational Rheometer [39], Sentmanat Extensional Rheometer (SER) [40], etc. The Meissners apparatus consists of two rotary clamping systems which are independently controlled by DC motors to impose extensional strain. It has an electrically heated chamber and fritted-metal gas-bed polymer support that can melt a polymer specimen. This sample can be supported at the ends by clamps and extension can be imposed. This device is suitable for melts. SER has two counter rotating wind-up drums that produce extensional deformation during the measurement. The sample volume can be fixed by two clamps. The SER system can be used for characterization of polymeric materials in uni-axial extension and solid tensile testing. These devices operate at macroscopic scales and require large quantities of sample from about tenth of a milli-litre to few tens of milli-litres based on the application and device. Small-scale extensional Rheometers include the micro plate-based Rheometer [10–12], magnetic bead micro Rheometer [41], etc. Using these techniques material functions such as the uni-axial extensional modulus and the uni-axial extensional viscosity of the specimen are calculated. Details of some of these Rheometers were discussed earlier in chapter(1) and a brief recap of is provided in the section.

FiSER employs an exponential strain profile on one of the end-plate, measuring the tensile force and the mid-filament diameter to extract the extensional viscosity. CaBER gives a step strain profile on one of the end plates, keeping the other end plate fixed. The fluid under consideration evolves due to surface forces and only its mid-filament diameter is monitored. As the conventional CaBER does not measure the axial force, the dependency on a relevant rheological model is inevitable. Meissner apparatus involves a setup significantly different from the above mentioned devices. It is predominantly used to characterize extensional properties of polymer melts. Micro-fluidic devices have also been popularly used to get extensional properties. The details of some of these devices have been discussed earlier.

4.4 MER - Rheometry at micro-scale

All the existing extensional rheometers probe the material properties at macroscopic scale. The amount of sample used in the filament stretching rheometers is large enough so that they can ignore (a) the end plate effects, (b) force contribution due to surface tension etc. MER is the first extensional rheometer that holds potential to study extensional rheological properties at scales that conventional Rheometers are unable to probe. Extensional Rheometry at microscopic scales is an important application of the MER. The aim of these experiments is to measure rheological properties of materials such as polymer melts, bio-polymer gels, synthetic silk, etc., subject to an uni-axial extensional flow. The sample requirement is just a few pico-litre and the filament lengths are of the order of few tens of micrometers. This feature can be very useful while characterising scarce or expensive liquids, especially biological fluids. As an extensional Rheometer, MER is flexible in its mode of operation and can be employed for both step strain and exponential strain profile. MER offers a new perspective to filament stretching experiments that can be carried out on filaments that are orders of magnitude smaller in dimensions as the one formed by the FiSER. Its facility of high resolution force measuring over a wide range is a major improvement over the other similar devices. Simultaneous imaging of the entire filament profile allows for particle tracking velocimetry and birefringence studies to measure stress or strain profiles in the samples.

There are associated challenges owing to the scale in which the setup operates. At microscopic scales surface forces become very important and the assumptions that the filament profile is cylindrical is no longer valid. Therefore several assumptions made by other existing rheometers may not be applicable to our experiments. For example, force as measured by FiSER is assumed to be only axial and all the other terms which draw contribution from surface tension and inertia etc, are neglected. In contrast, the force measured by MER cannot ignore the contribution from surface tension effects and treating this force as only the axial component, could lead to large discrepancy in the value of estimated transient extensional viscosity.

In this thesis we demonstrate the capability of our device to perform extensional rheology experiments at ultra small scales. We present experimental data for the required measurable parameters like force, extension and filament profile etc. We see that in computing final quantities like extensional viscosity and extensional modulus our results would not match the results from those of the existing rheometers which operate at macroscopic scale. Surface tension effects and filament profile need to be addressed to resolve these issues.

4.5 Experiments with MER

The basic experimental setup for extensional rheology experiments is already described in chapter (2). Figure (2.1) illustrates the complete setup. The zoomed in portion of the working area is shown in (2.4). In this section we will explain different modes in which the device can be configured for the extension rheology experiments and then go ahead to describe the course of the experiments.

Table 4.1: Comparison of MER with other Rheometers

Property	CaBER[108]	FiSER [33]	MER
Mode of operation	Capillary breakup	Filament stretching	Both
Strain profile	Step and exponential	Exponential	Step and exponential
Force sensitivity	-	10μN	1pN
Force range (mN)	-	$0.01 - 500$	$10^{-9} - 10^{-2}$
Zero Shear viscosity range ($Pa.s$)	$10^{-2} - 10^{3}$	$10^{0} - 10^{4}$	Yet to be confirmed
Plate Geometry	Flat	Flat	Flat/curved
Plate diameter	4 to 8mm	10mm	125μm
sample Volume	Few ml	Few ml	Few pl

The aim of this work is to develop the capability to perform extensional rheology at microscopic scale. We present the protocols we have developed, tests, current status and future directions.

The device can be set in three basic configurations at the instrumentation level as shown in the figures (4.6) and (4.7).

1. Curved surfaces mode

One end of the optical fibre is connected to the laser source and the other end is allowed to pass through a brass rod and clamped such that the required length of the fibre acts as the cantilever. On the other side a metal needle is taken, a small portion of the optical fibre ($\sim$ 1mm) is fixed into the needle so that the sample holding ends are identical on both sides as shown in figure (4.6 (a)). In this mode the cantilever and the glass rod with fibre, are aligned such that their curved surfaces face each other. The sample is loaded between these curved surfaces. The region where sample wets the surfaces is not planar in this mode. This configuration will be termed curved surfaces mode from now on.

2. Flat surfaces mode without cantilever

In this mode there is no cantilever. On both sides rigid needles with fibre pieces are used. These needles are bent at right angles close to the bottom and a piece of fibre fixed into them. See figure (4.6 (b)). The circular sections of the two fibre pieces face each other and the sample is loaded between them. Force measurement is not possible in this mode, as there is no cantilever. This mode is similar to the conventional CaBER.

3. Flat surfaces mode with cantilever

A small piece of fibre is attached to the cantilever just above its tip, perpendicular to the cantilever axis. The attached piece is just about $200-300\mu$m in length and attaching this piece to the cantilever has to be done under a stereo microscope. On the other end the rigid needle is bent at the bottom at right angle and a small piece of fibre is fixed into this needle. See (4.6 (c)). The fibre pieces on both the ends needs to have well cut flat surfaces for uniform wetting and this is ensured by cutting these pieces under the stereo microscope. On both the ends horizontal planes of the attached fibre pieces face each other. The sample is loaded between the exposed circular planes. Light spot coming out of the cantilever tip as well as the whole filament with end plates is imaged. It is possible to read the position of light spot on camera or on PSD based on the requirement. This configuration will be termed as flat surfaces mode.

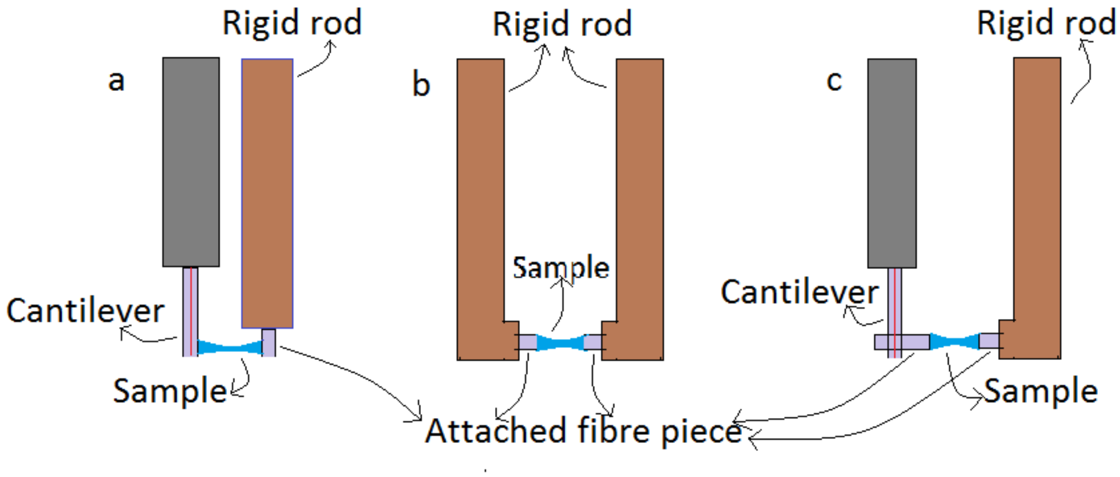

Figure 4.6: Schematic showing the curved and flat surface configurations. (a) sample is loaded between the cylindrical surfaces close to the tip of the cantilever and the rigid rod. (b) A small piece of fibre is attached close to the bottom of the cantilever. The rigid rod is bent at the bottom with protruding fibre piece. In this configuration the flat sections (circular face) face each other and the sample is loaded between them.

The experiments we performed were classified into two types based on the nature of the strain imposed. The piezo was commanded either step strain or exponential strain based on the requirement. Suitable LabVIEW codes was employed to command piezo in order to impose different types of strains. Both types of strains can be imposed in all the plate geometries shown in (4.6). The response of the sample to imposed strains varies based on the type of chosen strain.

We performed relevant experiments in all the above modes on both Newtonian and non-Newtonian fluid samples. Glycerol (Sigma Aldrich, USA) was used as the test sample for Newtonian fluids and Polydimethylsiloxane (PDMS)(Anton Paar GmbH, Austria) for the non-Newtonian visco-elastic fluids. The following procedure is followed to perform all the extension rheology experiments. Detailed protocol is provided in Appendix C.

Sample under probe was loaded between the cantilever and the other rigid rod with attached fibre piece as shown in the figure (4.6(a) or (b) or (c)) based on the mode used. Distance between the surfaces is adjusted to form a small, stable, filament. Initial length of the formed filament was measured using the camera. A LabVIEW program was used to impose the strain or force in the desired mode. The feed back mechanism was employed wherever strain or force control was needed.

The Figure (4.7) shows the images of surfaces and the liquid bridge between them in flat as well as curved configurations.

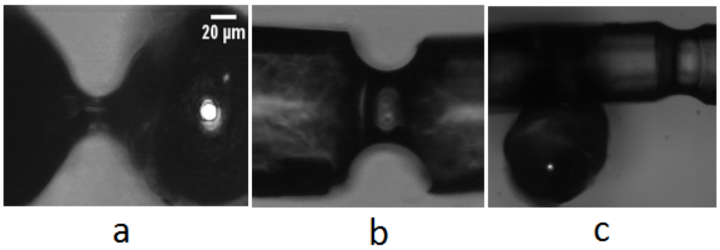

Figure 4.7: Different experimental configurations. (a) Sample loaded between the cantilever and the rigid rod between their cylindrical surfaces (b) Sample between the two flat ends without cantilever (c) Sample between the flat ends with cantilever. The bright spot in (a) and (c) is the laser light exiting the cantilever

Before proceeding for the experiments we measured the baseline noise. A few picolitre PDMS was loaded between the cantilever and the rigid rod and was allowed to settle and spread evenly. Using the LabVIEW code for MER operation, force and strain were recorded. For this test we chose a cantilever of length 10mm and diameter 125μm. The Liquid bridge between the surfaces was 9.8μm long. From the data we get a standard deviation of 0.05 for the strain fluctuations and 1.5μN for the force fluctuations,which is the base line noise for the system under regular operating conditions. This noise is well within 2% at the most for the force and extension measurements.

Experiments imposing exponential and step strain are discussed in the following sections.

4.6 Exponential strain

For a uni-axial, shear-free, extensional flow of a sample with a cylindrical profile of initial diameter D_0 and length L_0, which is subjected to a stretch in the axial direction z by an external force F so that its radius decreases uniformly along the length the kinematics are independent of spatial position. The velocity-gradient tensor $\dot{\epsilon}_{ij}$ is given by

$$\dot{\epsilon}_{ij} = \frac{1}{2}\dot{\epsilon}\begin{pmatrix} -1 & 0 & 0 \\ 0 & -1 & 0 \\ 0 & 0 & 2 \end{pmatrix} \tag{4.6}$$

where $\dot{\epsilon}$ is the rate of extension. If $\dot{\epsilon}$ is constant throughout the imposing time, then the flow is considered to be a steady flow. The length of the extending filament varies with time as $\frac{dL}{dt} = \dot{\epsilon}t$. Under the volume conservation condition, the length and the diameter of the flowing sample at a given time t can be written as

$$L(t) = L_0 \exp(\dot{\epsilon}t) \qquad\qquad D(t) = D_0 \exp(-\frac{1}{2}\dot{\epsilon}t) \tag{4.7}$$

Where L_0 is initial length of the filament and D_0 is the initial diameter. Under ideal conditions (cylindrical evolution of the filament) imposing an exponential strain results in a constant rate of extension at which the sample is subjected to uni-axial extensional flow.

4.6.1 Experiments on Glycerol

Glycerol is a canonical Newtonian fluid. Nevertheless, there have been no reported experiments at the scale that the MER can handle. The general procedure of loading the sample is same as that mentioned earlier (detailed protocol in Appendix C). In these tests we used a cantilever of 9.12mm length and 125μm diameter which give the spring constant of 27.4N/m. Few pico-litre of glycerol sample was loaded on to the fibre tip on the rigid rod. Cantilever and the rigid rod were brought into the focus using a 20X objective lens. The rigid rod is moved towards the cantilever initially with the help of translation stage until the distance of separation between the blob of glycerol and the cantilever was about $3 - 4\mu$m. The contact is made by moving the rod with the help of piezo for the remaining distance. The sample was allowed to settle and form a stable filament. A known value of exponential strain rate $\dot{\epsilon}$ was imposed using the home made LabVIEW code. We fed in an analog signal from the function generator, in which case it was exponential. Also we used digital input, in which case the exponential was approximated by a series of steps where the step size scales with the strain rate. The cantilever tip as well as the evolving filament were imaged using the high speed camera (MotionPro Y4, Integrated Design Tools Inc., United States) at $10,000$ fps.

Using suitable home developed MATLAB codes (a) position of cantilever tip as a function of time and (b) mid radius of the evolving liquid filament were computed. With the knowledge of the spring constant of the cantilever and the position information cantilever tip, force was calculated as a function of time. Force data and filament radius data together gave the stress varying in time and the imposed strain rate was a known quantity. With these known parameters transient uni-axial extensional viscosity is obtained using the relation $\eta_e(t) = \eta_0 \exp(\dot{\epsilon}t)$ [33]. Experiments were performed at different imposed strain rates from $0.5s^{-1}$ to $10.5s^{-1}$ in steps of $1s^{-1}$. Figure (4.8) shows the transient uni-axial extensional viscosity plotted against time for the imposed strain of $3.5s^{-1}$.

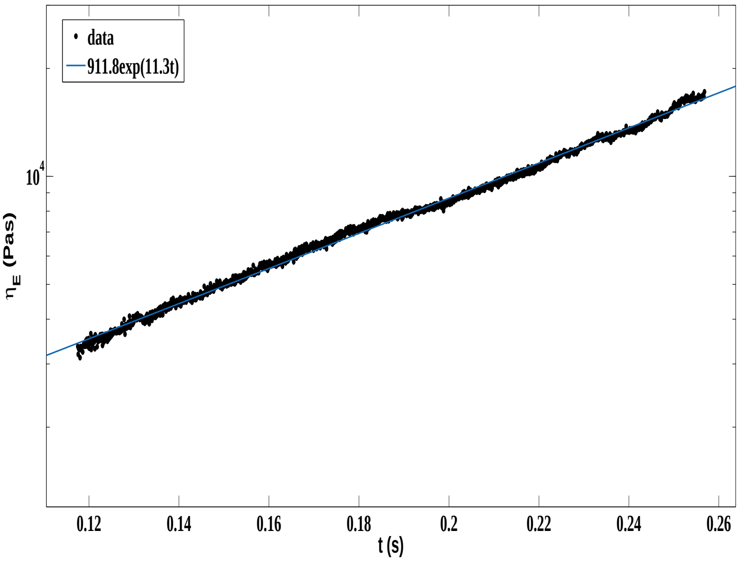

FIGURE 4.8: Log-linear plot of transient uni-axial extensional viscosity of glycerol under exponential strain. Imposed strain rate ($\dot{\epsilon}$) is $3.5s^{-1}$.

The results are compared with the known model for the transient extensional viscosity $\eta_E(t;\dot{\epsilon})$ for Newtonian fluids under steady, homogeneous, uni-axial extension [109]

$$\eta_E(t;\dot{\epsilon}) = \frac{Fe^{\dot{\epsilon}t}}{3A_0\dot{\epsilon}} \tag{4.8}$$

The comparison shows that the transient viscosity follows an exponential trend as required by the model but the calculated strain rate is larger by a factor of about 3 as compared to the experimental strain rate. We predict that the discrepancy is due to the assumptions made in the constitutive model. The model assumes the evolution of a cylindrical filament as shown in figure (4.1). In our case the filament geometry is an evolving catenoid and the filament dynamics are very likely geometry dependent. See figure(4.9).

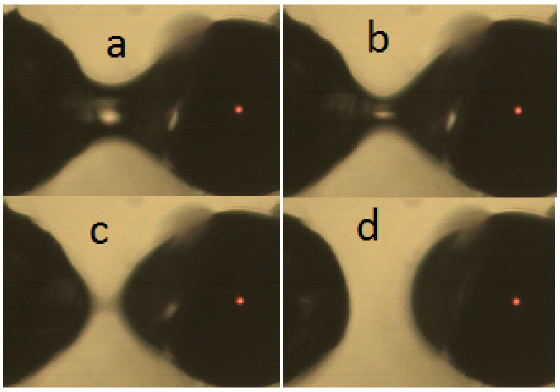

Figure 4.9: Filament extension and breakup in glycerol sample under exponential strain.

4.6.2 Experiments on PDMS

Following the same experimental protocol as was used for Glycerol we performed experiments imposing exponential strain on PDMS. PDMS being visco-elastic, the filaments survive longer than those in case of Glycerol. We used a cantilever of length 9.65mm and diameter 125μm for these experiments and imaging was done at 2000fps using the high speed camera. The imposed strain rate was $6s^{-1}$. variation of viscosity with time is assumed to follow the one mentioned in the earlier case. We assumed the transient uni-axial extensional viscosity of PDMS to vary with time as $\eta_e(t) = \eta_0 \exp(\dot{\epsilon}t)$ and the data was fit to the model (4.8). Results are shown in figure (4.10). We can see that the calculated strain rate is $5s^{-1}$ which is close to the value of imposed strain rate. But in case of polymer melts like PDMS there is no constitutive model that can be used to compare our results of the experiments at microscopic scale. FiSER was used to perform similar experiments but at a very large scale. The filaments formed in case of FiSER were few tens of centimetre long and were fairly cylindrical in geometry. They consider the measured force to be mainly axial, ignoring the contribution from surface tension and inertia. As previously mentioned, in our case surface forces can not be ignored and due to this aspect a relevant model is to be developed to interpret our results completely.

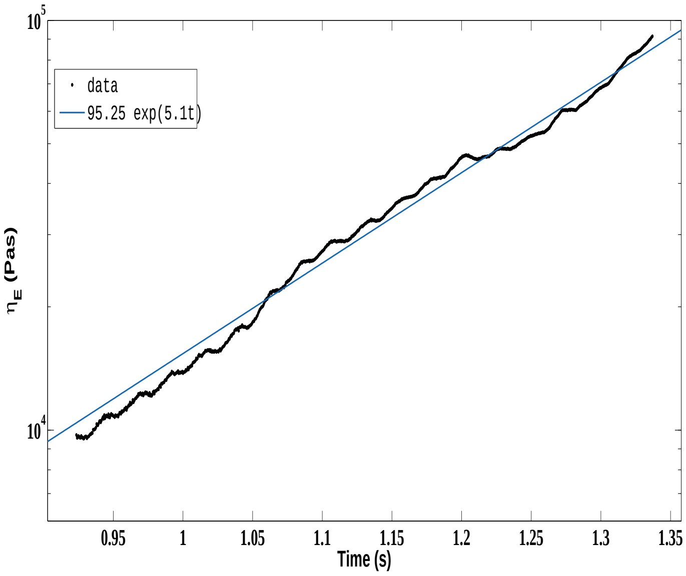

Figure 4.10: Log-linear plot of Transient uni-axial extensional viscosity of PDMS under exponential strain. the imposed strain rate ($\dot{\epsilon}$) is $6s^{-1}$.

In the above two cases of glycerol and PDMS exponential extensions, we assumed that the variation of viscosity with time obeys the relation $\eta_e(t) = \eta_0 exp(\dot{\epsilon}t)$ and compared the experimentally imposed strain rate with the strain rate obtained from the expression.

4.7 Step strain

In these set of experiments a step strain of known magnitude is imposed on the sample and that extension is maintained with the help of the feed back mechanism. As already mentioned the feed back mechanism can be operated in constant force or constant strain mode. In the constant strain mode, the deflection of the cantilever and the cross-sectional area are monitored. Details concerning the formulae used to calculate the force and the strain are discussed earlier. In these experiments we measure the uni-axial extensional modulus. The (transient) uni-axial extensional modulus of the material is defined as the ratio of the extensional stress (the time-varying force divided by the time-varying cross-sectional area of the mid-portion of the filament) and the extensional strain. The step strain experiments were performed on Glycerol well as on PDMS.

4.7.1 Experiments on PDMS

We performed constant extension (or strain) experiments with feedback control using PDMS, with a commanded extension of 10μm. The experimental protocols and sample loading procedure were same as already mentioned in earlier sections. The cantilever had a length $\ell = 15.1$mm and a diameter $d = 125\mu$m. In Figure (4.11), a plot of the extension $\Delta y(t)$ and the response force $F(t)$ as a function of the elapsed time t is shown. The plot shows that the extension (or strain) equilibrates to the commanded value within 0.5s, and the force exerted by the filament decays over a longer period of time. For incompressible materials subject to uni-axial extension in the linear visco-elastic regime, it can be shown[110] that $\lim_{\epsilon\to 0} G_u(\epsilon) = 3 \lim_{\gamma\to 0} G(\gamma)$, where G_u is the uni-axial extensional modulus, $|G| \equiv \sqrt{G'^2 + G''^2}$ is the shear modulus, where G' and G'' are the moduli obtained from the two components of the modulus from an oscillatory shear test, ϵ is the uni-axial extensional strain and γ is the shear strain. A stress-controlled rheometer (MCR-301, Anton Paar GmbH, Austria) with 50mm diameter cone-plate geometry was used to estimate the value of the shear modulus ($G \approx 7800$Pa) at shear strains $\gamma \lesssim 0.01$. For values of the extension $\Delta y(t) \lesssim 10\mu$m (or $\epsilon \lesssim 0.28$), we find a negligible change in the mid-plane diameter of the filament and assume that its cross-sectional area is a constant. The calculated extensional modulus (using the equilibrated value of the force $F \approx 22.7\mu$N) is found to equal $G_u \approx 61000$ Pa, i.e. $G_u/G = 7.82$. For visco-elastic materials such as PDMS, the filament is subject to surface tension forces, elastic stresses, gravity (which is usually negligible), viscous forces and inertia. The complete force-balance equation for the filament may be found in some earlier references[36]. In our test, we do not take into account effects due to curvature of the filament or the inertia, and thereby ignore contributions to G_u from such terms. We have also assumed that our deformation is purely uni-axial, which may not be true near the ends of the filament. In a future study, we aim to reduce this discrepancy in our measurements, by explicitly taking into account effects due to surface tension and inertia and with the inclusion of results for a Newtonian fluid.

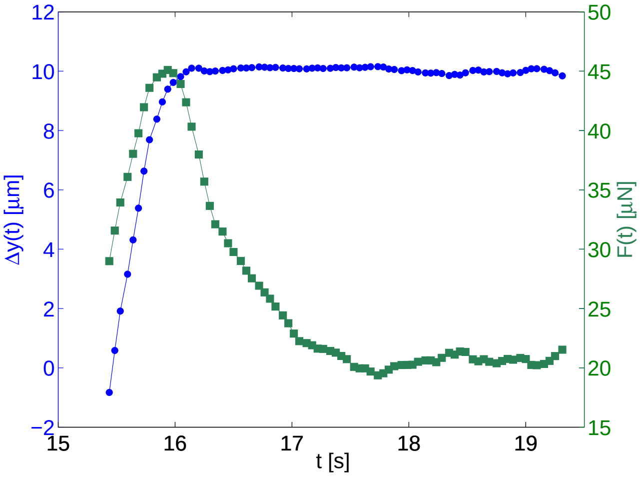

FIGURE 4.11: A plot of the extension $\Delta y(t)$ and the force $F(t)$ as a function of the elapsed time t, from a test with a commanded step of 25μm imposed on a polydimethylsiloxane (PDMS) filament with initial length $L_0 = 30.6\mu$m.

4.7.2 Experiments on Glycerol

To perform step strain experiments on glycerol we used the flat surfaces configuration without cantilever. In this mode the viscosity is calculated using the mid filament radius and the surface tension. Same protocols as mentioned earlier were used to perform the tests. Length of the cantilever used was 11.1mm and the diameter was 125μm. a step strain of 60μm was imposed. Filament evolution was recorded at $10,000$Hz. Viscosity(η) of a Newtonian liquid can be obtained from capillary breakup measurements using the evolution of mid filament radius ($r_{mid}(t)$) , surface tension (γ) and breakup time (t_c) using different models [38]. While the form of expression is similar under the assumption of cylindrical evolution of the filament, the pre factors are calculated using numerical simulations based on experimental conditions(4.9) . In our case, as the filament evolution is not cylindrical, even the form of expression might change. Here we present the radius - time data. detailed CFD simulations are in progress with our collaborators, to obtain the appropriate model considering our experimental conditions

$$r_{mid}(t) = k_1 \frac{\gamma}{\eta}(t_c - t) \tag{4.9}$$

the pre factor k_1 comes from the boundary conditions.

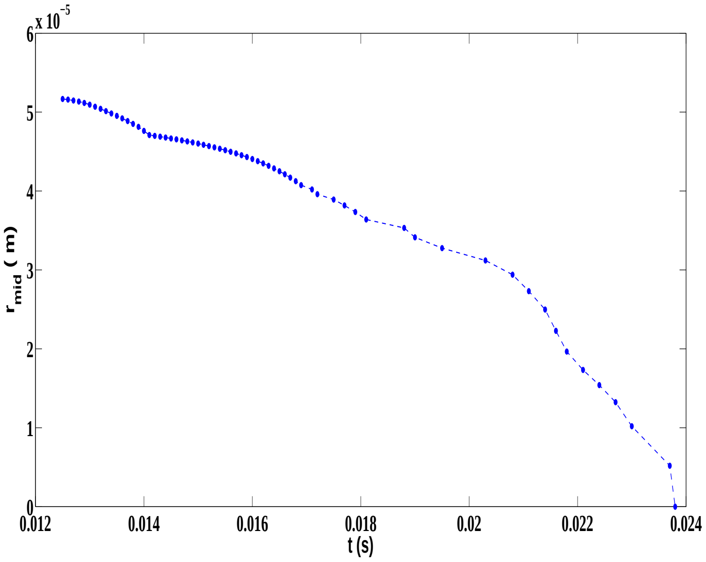

FIGURE 4.12: Mid filament radius plotted against time for glycerol under step extension. Impose extension (ϵ) is 60μm. This experiment was performed in the flat surface mode without using cantilever. The plate diameter is 125μm.

4.8 Flat vs Curved surfaces

As it is already discussed in setup configurations the plate geometry can be chosen to be either flat or curved. We performed tests using both these surfaces to mark differences if any in the nature of filament evolution. We used glycerol as the test sample for these experiments. sample was loaded between the plates and following the standard protocol a 60μm step strain was imposed. From the figure(4.13) we see that there are kinks in the plot for flat surfaces. This non smooth decrease in radius profile could be due to the slip of the liquid at the boundaries (end plates) in flat surfaces configuration. Hence the cylindrical surfaces could be better suited for MER.

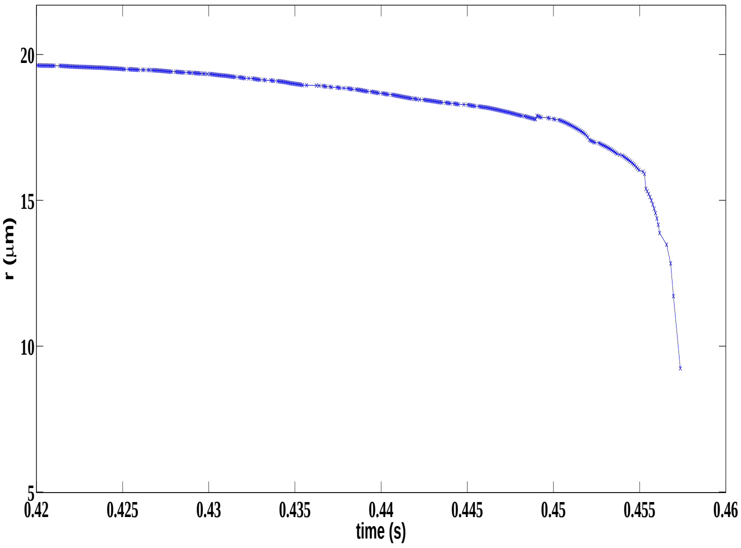

(a)

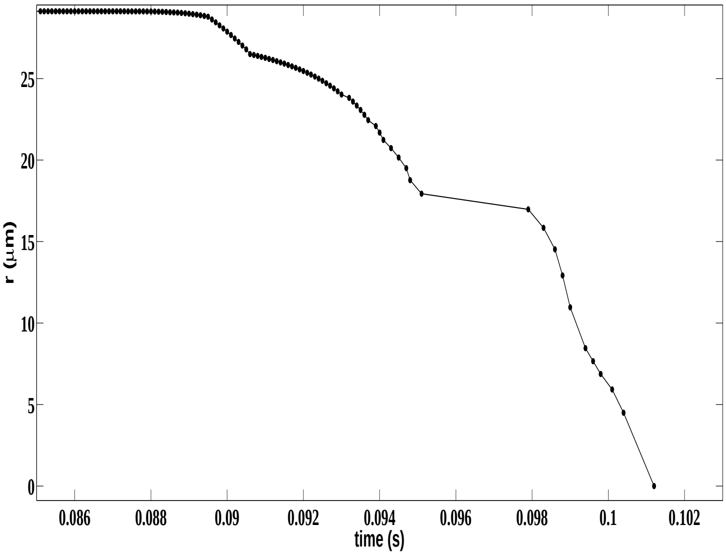

(b)

FIGURE 4.13: (a) Radius vs time plotted for the extension of glycerol under step strain. We see a smooth fall in the radius with time when we used curved surfaces. (b) similar test using flat surface configuration. As the radius starts to decrease,there are kinks which could be due to slip at the end plates

4.9 Measuring surface tension

We hypothesise that, surface tension could have a non-trivial contribution to the measured forces, and this may partly account for the observed discrepancies. If this is the case, surface tension of the material under probe has to be known before proceeding with any extensional rheology measurements. We wanted to demonstrate that this set up can measure surface tension of equilibrated fluid samples. This would also add to the capabilities of the applications of the device.

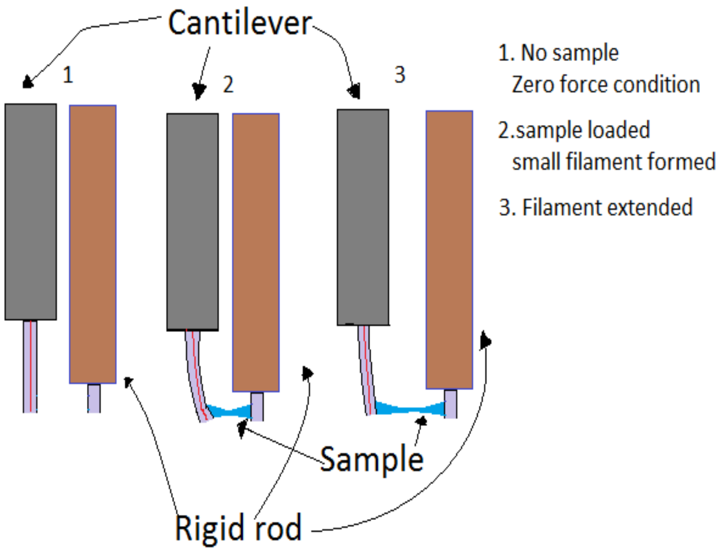

FIGURE 4.14: (1) Zero force condition. As no sample is loaded cantilever does not experience any force (2) Sample loaded, a definite extension imposed and waited for the filament to equilibrate (3) Filament elongated further and equilibrated at the new extension

To measure surface tension, the following protocol was used. The cantilever was focused using a 20X objective and laser light coming out of the tip of the cantilever was made incident on the PSD. The PSD reading at this step along with cantilever spring constant gives the zero force condition. Then the sample (Glycerol) was loaded between the two flat surfaces described earlier. A small filament was formed by giving a step extension using piezo and was allowed to settle. When force has equilibrated the force on the cantilever was measured. Filament with the surfaces

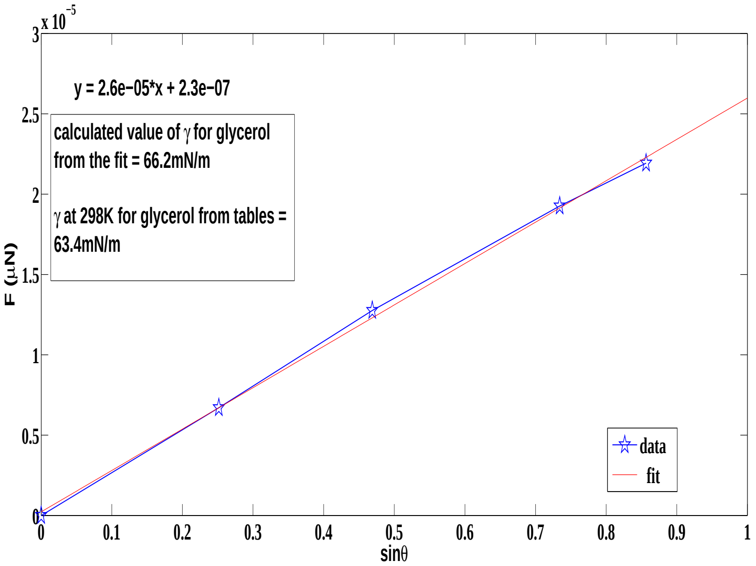

(a)

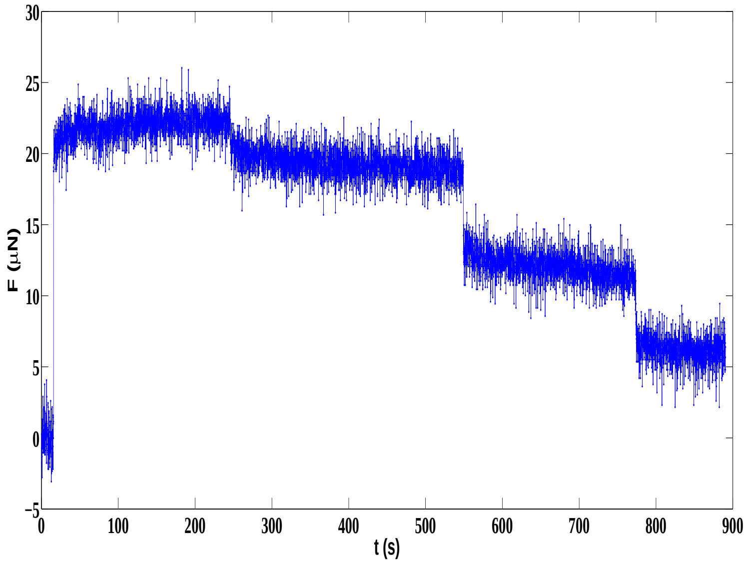

(b)

FIGURE 4.15: (a) Force as measured by the cantilever as a function of sine of the contact angle obtained by applying 5μm step displacements to a filament and allowing it to equilibrate. Surface tension is calculated from the slope of the curve and using the expression (4.10) and is compared with standard values from tables. (b) Variation of force with time. Each step corresponds to force at a particular filament profile.

was imaged using the camera. This process was repeated for different values of force and filament profile. Measuring the angle between the liquid bridge and the flat surface, surface tension was calculated using the expression

$$\gamma = \frac{F}{2\pi r \sin\theta} \tag{4.10}$$

Where r is the radius of the flat surface figure(4.6(c)) The figure(4.15(a)) shows the measured force as a function of sine of the angle measured. Figure 4.15(b))shows the measured force for different steps. Using the slope of the force vs $sin\theta$ curve, surface tension of glycerol was found to be 66.2mN/m.This is close to the value 63.4mN/m, obtained from standard tables.

4.10 Discussion

There is a need for a micro-extension rheometer as many processes like fibre spinning and silk extrusion etc happen at micro-scale. This chapter is aimed at exploring this possibility. Hence we have developed protocols for performing Micro Extension Rheology using our force apparatus. This work was done to explore the capability of our device to perform extensional rheology experiments at ultra small scales. We show that we can indeed perform filament extension at micro-scale with simultaneous precision force measurements. The experiments were performed using different plate geometries and different types of imposed strains. Using feedback mechanism we could control strain with high precision (4.11). Tests performed using standard Newtonian and non-Newtonian materials show that simple comparison between macro-scale experiments and micro-scale experiments do not hold.

The discrepancies, between the results with our device and the other existing rheometers, can be broadly attributed to two effects.

1. In the filament stretching mode (FiSER) using an exponential strain profile, material properties are calculated ignoring the contribution of surface tension to the measured force and cylindrical profile is assumed for the filament evolution. In our case both these conditions need modification and suitable models are to be developed to account for surface effects as well as catenoidal filament evolution.

2. In capillary breakup mode experiments the constitutive models are based on calculating viscosity using surface tension, but assume uniform cylindrical evolution of the filament. In case of MER the filament being catenoidal we need modified models to account for the role of geometry

On the experimental front, these problems may be overcome by measuring the entire filament profile in real time and an accurate estimate of the surface tension of the material under study. We show that both these measurements are indeed possible with our device. However, existing models have to be modified to take these effects into account, if one is to extract useful information from such measurements. Such an effort is in progress and is beyond the scope of this thesis.

Chapter 5

Summary

Summary

We have developed a force measurement device that can be applied to perform a variety of experiments in the fields of mechano biology, active matter dynamics and extensional rheology. The device has force resolution of the order of a piconewton and position resolution of the order of a nano-meter. The device can be operated in passive as well as active modes to sense or apply forces of magnitudes discussed earlier. The feedback control enables measurements in constant extension or constant force modes as per the need. A variety of detection mechanisms employed make experiments at different length scales possible.

Using the device we explored the dynamics of active suspensions taking different strains of E.coli as model systems. These types of experiments open up the possibility of investigating challenging problems in the less explored fields like the interface of non-equilibrium statistical physics and hydrodynamics. These areas, mainly explored by theories and simulations can get richer by the state of art experiments like those ours and shed light on several aspects of self propelled systems.

Then we investigated the material properties of Newtonian and non-Newtonian liquids under extensional flow. Our device is the first and only instrument which can perform extensional rheology in ultra-small scales. With the necessary theoretical and computational tools developed the instrument has potential to probe extensional properties materials like biological fluids, synthetic and spider silk which have non-trivial importance in academic and industrial research.

Motivation and one of the major aims of the device is to investigate mechanical properties of axons. The active and visco-elastic properties of axons are considered to be important in axonal retraction after injury or during rewiring and in stretching during limb movement. The device has a dedicated configuration to perform the experiments to pull on axons (2.6). Necessary LabVIEW codes were developed to execute feedback mechanism to control strain or force in this configuration. Plot from a proof principle experiment is shown in the figure (5.1). These experiments are in progress by other members in the lab as their thesis problems.

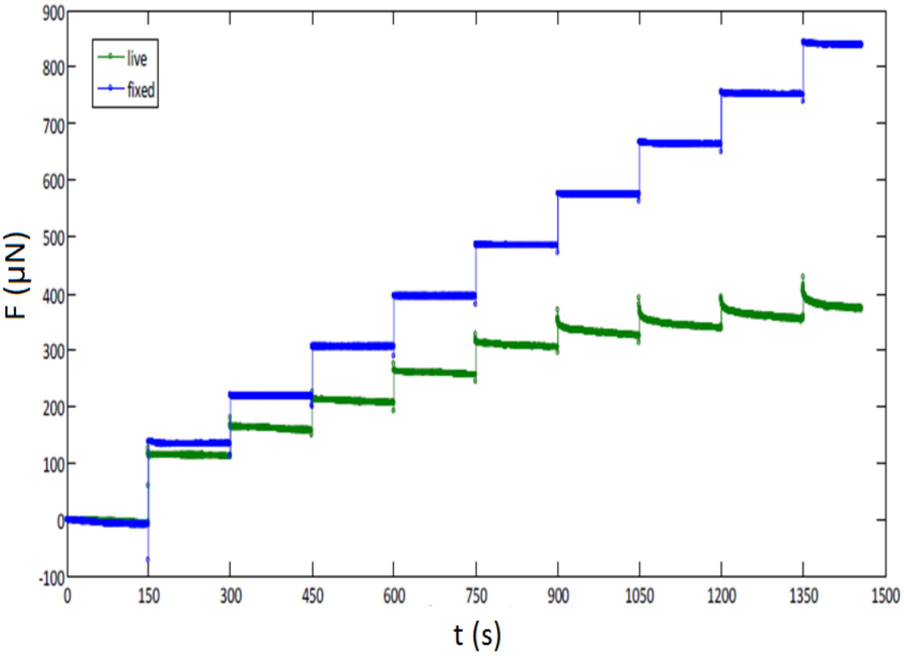

FIGURE 5.1: Live and fixed axons being pulled under constant extension. The feedback mechanism imposes and maintains constant extension and force response is measured.

In short we have developed a force apparatus using an etched optical fibre as cantilever. We have used the device to explore the dynamics of bacterial suspensions and have shown that the device has a potential to perform extensional rheometry at microscopic scales.

Appendix A

Important components of setup

1. Vibration isolation table.

2. Laser source and accessories

3. Optical fibre

4. Inverted microscope and related optics

5 .Position sensitive detector

6. CCD camera

7. Piezo electric actuator

The specifications of above components are given below:

Laser Source

Melles Griot 25 LHR-925-230 ,He- Ne laser

Wave length 633 nm (red)

Output Power (performance) : 17 mW

Bream diameter: 1.23mm

Polarization: Linear, 500:1

Cantilever:

Single mode Optical fibre from THORLABS (p1 -630A- FC-10)

wave length range :630nm -680nm

Core (MFD) : Dia 4nm (Glass, silica composite)

clad :Dia 120nm (glass)

Outer sheath (yellow): Dia 3mm

Middle sheath (green/white): dia 1mm

Density : 2.329E3 kg/m3(Thorlabs suggested value)

2.2974x103kg/m3(Measured in lab)

Youngs modulus: 73GPa (thorlabs suggested Value)

Microscope:

ZEISS Axio observer - D1 (coded,semi-motorized)

Free working distance : 70mm

(Distance between condenser and specimen)

Objective:20x/40x/100x in 1/1.6/2.5 optovar

Filter inserted below trinocular tube - FILTER DICHROIC GRN25MM D(Edmund optics)

Microscope stage : In house designed 228mmx140mm Aluminium stage

Position sensitive detector:

PSD 2044 ,Hamamatsu photonics 2D pincushion typed Position sensitive detector (photodiode surface resistance based position measurement system)

Active area 4.7mm x 4.7mm

Resistance length 5.7 mm on each of X and Y axes.

Signal processing circuit:

C 9069,Hamamatsu photonics, Japan with following specifications

Supply voltage 12V DC, 12 bit digital output at 200 Hz through RS 232 serial interface to a computer.

Serial port settings: Baud rate 38400 bps, databits 8, parity none, stopbits 1 and no flow control.

Vibration isolation table:

Model: Newport VH Iso-station VH3648- opt

Dimensions: 4ft x 3ft

Maximum pay load : 909 kg

Maximum air pressure: 90 psi

Platform: optical bread board with metric screw holes

The table provide pneumatic vibration isolation for the platform loads up to 909kg. With an air pressure maximum of 90 psi. Vibration isolation is provided at frequencies above of 5Hz and a low amplification at resonance (1.5to 2Hz).

Function Generator:

Model: Agilent 33220A, 20MHz Function/arbitrary wave form generator

Specifications:

waveforms: sine, square, Ramp, Triangle, Pulse, Noise, DC Built-in arbitrary forms: Exponential rise, Exponential fall, Negative Ramp, sin(x)/x, Cardiac.

Frequency: 1 Hz to 20 MHz with 1Hz resolution.

Amplitude: Maximum 10Vpp

Camera:

Active Pixels :1004(h) x 1002(v)

Pixel Size (m) : 8

Image Area :8mm x 8mm

Act. Area Pixel Well Depth (e-, typical): 30000

Gain Reg. Pix. Well Depth (e-, typical) : 80000

Max Readout Rate :13.5MHZ

Frame Rate (fps) :12.4

Read Noise (e-, typical):¡1 to 18 @ 13.5MHz

Piezo Electric Actuator :

Piezo actuator (P-841.60, Physik Instruments GmbH, Germany) with a strain-gauge sensor has a 90m travel range, and comes with a single-axis piezo servo-controller (E-625.SR) with 24-bit A/D, 20-bit D/A resolution, equipped with a USB interface. The actuator can sustain a pushing force up to 1000N, a pulling force up to 50N and a maximum torque on the tip of 0.35Nm.

Protocol for etching the fibre:

1. Remove the outermost jacket(yellow) using a surgical knife .

2. To remove the second layer (buffer), burn the wire using a lighter , it will melt off the buffer and we have a glass fibre of diameter about 125 . Desired length of this part is decided based on the need.

3. immerse the glass fibre part of the cable into 48% HF and keep it on a magnetic stirrer and allow the acid to etch for 25 min. Without stirring acid will corrode the fibre to give a conical cross-section which isn't desired .

4. The fibre is removed and dipped into 25% HF and again Subjected to stirring . This process usually should be continued for around 15 minutes .

5. Time of etching mentioned is relevant for a fresh stock of acid and is likely to increase as the solution gets aged. Care should be taken to avoid breaking the fibre at every stage

Appendix B

Protocols for bacterial cell culture

Making frozen stocks

Try to reduce risk of contamination at all times (ask bacteriologist colleagues for advice on this). Open one tube (e.g. RP-437), and insert sterile loop into the tube, scoop up some agar near the surface (which contains the bacteria). Then insert the loop with the bacteria on it in 5ml of LB media in a sterile test tube. Repeat with the other tube (RP-5232). Keep the remaining two tubes as backup in the fridge. Grow overnight at 37 deg C with shaking. In the morning the tubes should be turbid (this is because of the bacterial cells). Make glycerol stocks by adding 3.33ml 50% glycerol (that has been autoclaved) to the 5ml cell suspension.

Put one ml of this solution into a sterile cryogenic tube, label with strain name, and date, place in a safe place in a -80 deg C freezer. Repeat this two more times so you have a total of 3 tubes. Then repeat for the other strain (giving now a total of 6 tubes 3 repeats x 2 strains. These stocks will be your backup. For the experiments one needs to take 100μl of glycerol/cell solution and place in a sterile eppendorf. Repeat 50 times and label each tube with the strain name. Then repeat the procedure with the other strain. Keep the tubes of the two stains separate by placing in different boxes/bags and put them in a -80 deg C freezer. These are the stocks one will use to grow the bacteria for the experiments.

Growing cells for the experiment

Take a 100μl tube of cells from the -80 deg C freezer and defrost by holding in the hand. Add 20μl of cells to 5ml of TB media in a sterile test tube (or flask). Grow at 30 deg C with shaking for 5.5 hours. Test optical density of culture at 600nm using a Spectrophotometer. You want a reading of 0.6 (acceptable range $= 0.5 to 0.7$). If your OD is higher than this then add less than 20μl of cells next time (e.g. 5 or 10μl). If your OD is lower than this then add more than 20μl of cells next time (e.g. 50μl). The cells should be motile in TB media but will be more motile if you re suspend them in Motility Buffer (recipe below). Do this by taking 1ml of bacterial culture and put in an eppendorf. Spin down in a microcentrifuge at 7000rpm X 2minutes. The cells will form a pellet at the bottom of the tube. Remove supernatant and add 1ml Motility Buffer. Re suspend cell pellet by flicking tube hard 20 times. Spin down again, remove supernatant, and add 1ml fresh Motility Buffer. Look at cells under a microscope RP-432 cells should swim and tumble RP-5232 cells should swim continuously

Media recipes

1. Motility buffer

Per litre (with de-ionised water):

$K_2HPO_4 - -1.08g$

$KH_2PO4 - -0.52g$

EDTA – 0.015g

Adjust to pH 7 and autoclave

2. TB media:

Per litre (with de-ionised water):

$10g/lTryptone$

$5gNaCl$

Adjust to pH 7 and autoclave

Appendix C

Experimental Protocol for Extensional Rheology Experiments with MER

The piezo moves only along one axis, which is taken as the reference. First, align one of the axes of the translation stage (which would hold the cantilever) with the piezo axis. Align Y-axis of the PSD with that of the piezo. This is crucial, as it constitutes an assumption in the feedback-loop code. Note: Throughout the experiment, the objective should be protected by a loose cover slip.

1. Take a 26 Gauge needle between forceps (do not press too hard or fibre will not enter the needle), expose it to a flame and melt off the plastic cap. Spray the needle with 70% ethanol and stick it onto the piezo holder with super-glue wearing rubber gloves: Draw a line with super-glue on the piezo holder and press down with gloved finger for proper settling. Let the glue dry over 20 minutes. Make sure that the nozzle part of the needle is the free end.

2. Take the optical fibre, remove the yellow sheath with a scalpel and cut the nylon fibres. [Warning: Do not touch the tip of the fibre as it is extremely sharp]. Pass the fibre through the brass adaptor of the translation-stage (for the cantilever) and allow the white cladding (do not put a kink in the white cladding) to go through the brass rod exposing the required length ($\sim$ 1cm) of the fibre, which acts as the cantilever. Burn off the white cladding and spray 70% ethanol on the fibre to remove any accumulated debris.

3. Switch on the laser and look for the spot profile by focusing the tip of the fibre on a sheet of paper. If the profile is non-circular, cut the fibre tip again with a scalpel to get a clean (circular) spot. Mount the brass adaptor with the fibre on the translation-stage. The cantilever end is now ready to use.

4. Take the needle stuck to the piezo holder, dip a small piece of optical fibre (without yellow and white cladding) with the (180μm) cladding into super-glue, push it into the nozzle end of the needle with about 0.5cm fibre protruding out of the nozzle. Burn off the 180μm cladding on the protruding part of the needle, spray 70% ethanol. Put a drop of super-glue at the base of the needle to fix it and wait $\sim$ 20 minutes to dry.

5. Cut the fibre to about 3mm length under a magnifying glass/stereoscope. Bend the needle appropriately and mount the brass piezo holder on the piezo and focus to check if the profile cut is circular [Warning: Do not touch the tip of the needle since fibre glass tip is extremely sharp]. The piezo end is now ready to use.

6. Focus the mounted cantilever on the objective and ensure that the image of the fibre is a circular arc towards the end facing the piezo. Bring both the cantilever and the fibre on the needle into the field of view of the optical microscope, ensuring that they are not in contact.

7. Start PI MikroMove (servo on). Set the piezo position at its maximum displacement ($85 - 90\mu$m) using the piezo software.

8. Take another thin needle, dip into the sample being used, and touch it to the tip of the needle (attached to the piezo) to deposit a small quantity onto it. Ensure that you get a smooth near-cylindrical (or hourglass-shaped) filament profile between the needle and the cantilever by moving the needle towards the cantilever (in small increments) using the PI MikroMove. Wait for$\sim$ 5 minutes to allow residual stresses in the cladding, etc to relax and let the sample equilibrate.

Protocol for MER Application software (LabVIEW code)

1. Set the Move Piezo button to off if it is not already in the off position.

2. Select the mode of operation (constant strain or constant force).

3. Enter in the values of the cantilever diameter and length, and set the file path.

4. Start the VI. Press the start button.

5. The code asks user to fill in the desired value of strain or force.

6. The program starts running and the current PSD and Piezo positions are shown on the output panel.

7. Press Initialize (BL) button. The code starts writing current force and strain to output file.

8. Slowly move the needle on the piezo towards the tip of the cantilever with the help of the translation-stage (keep observing the camera image) and allow the sample to touch the cantilever. Care should be taken so as not to move the cantilever beyond its initial position. Allow the sample to equilibrate so as to form a stable filament by monitoring the fluctuations in the force in the graphical display.

9. Measure the initial length of the filament and enter this value in the input panel.

10. Press the Initialize (AL) button on the control panel.

11. Press the Move Piezo button.

12. Upon completion of your experiment, press the Stop button.

Appendix D

Effect of viscosity on amplitude of cantilever deflection

To establish the position resolution measurements in over damped conditions experiments were performed using aqueous glycerol solutions. The protocol followed was as follows.

1. An etched cantilever was immersed in water and allowed to relax for about an hour.

2. Laser light coming out of the tip of the cantilever was made incident on the quadrant photo diode (QPD) via 40x magnification objective.

3. QPD output (time series data) was collected at 10kHz for 10 seconds for each run as a function of time for X and Y axes.

4. This process was repeated replacing water with Aq.Glycerol solutions of different concentrations. Same cantilever was used for all the experiments.

5. Glycerol concentration was varied from 0% to 95%. This corresponds to 0.9 mPas to 380 mPas of viscosity at lab temperature ($24 - 25$ degree C)

6. Cantilever dimensions: Length 20.2 mm, Diameter 8.9μm.

7. Cantilever was coated with Bovine Serum Albumin (BSA). This measure prevents water from wetting the cantilever so that cantilever does not accumulate additional mass.

From the figure (2) we can observe a systematic decrease in cantilever amplitude up to a viscosity of about 100mPas and show very small fluctuations later. While this is the consistent experimental observation from three different sets of experiments, the trend what we see is counter logical with the theoretical predictions. For a Brownian oscillator in over damped condition, mean square amplitude is independent of viscosity beyond the relaxation time and in our case the relaxation works out to be few milliseconds while we wait much longer and perform the

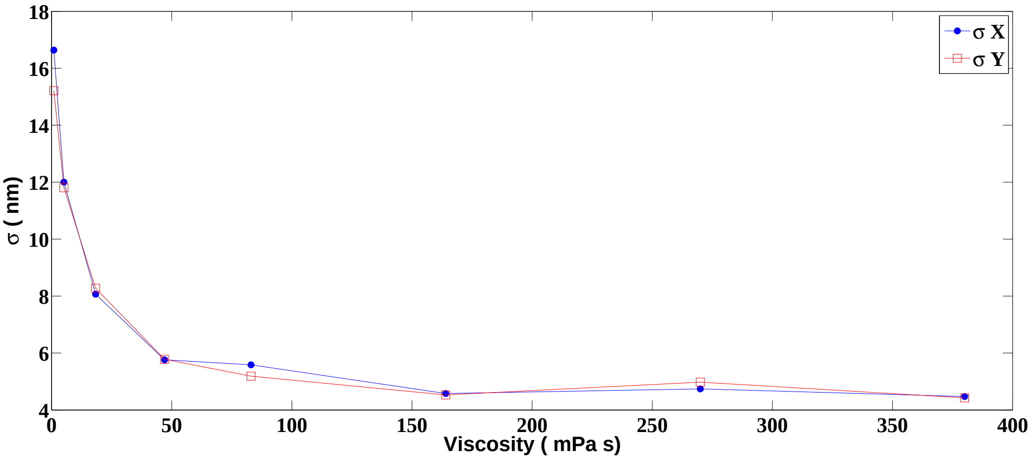

FIGURE 2: Standard deviation of cantilever deflection as a function of viscosity of the medium. The circles represent data of X-axis on QPD while the squares show that of Y-axis

experiments. From Smoluchowski equation, for an oscillator, the variance of the position is given by [106]

$$< x^2(t) > - < x(t) >^2 = \frac{k_B T}{m\omega_0^2}(1 - \exp{(\frac{-2\omega_0^2 t}{\gamma}}))\tag{1}$$

As t tends to infinity (time scales much larger than relaxation time are taken as infinity)

$$< x^2(t) > - < x(t) >^2 = \frac{k_B T}{m\omega_0^2}\tag{2}$$

Therefore, the standard deviation of the cantilever fluctuation becomes

$$\sigma = \sqrt{\frac{k_B T}{m\omega_0^2}}\tag{3}$$

Which means that standard deviation should saturate to its equilibrium value and become independent of viscosity after relaxation time scale which is our case. But in experimental realizations we see this happening beyond 100mPas and not below.

Bibliography

[1] G. Binnig, C. Quate, and Ch. Gerber. *Phys. Rev. Lett.*, **56**:930, 1986.

[2] O. Sahin, S. Magonov, C. Su, C. Quate, and O. Solgaard. *Nature*, **2**:507, 2007.

[3] A. Ashkin. *Phys. Rev. Lett.*, **24**:156, 1970.

[4] A. Ashkin. *Proc. Natl. Acad. Sci.*, **94**:4853, 1997.

[5] C. Haber and D. Wirtz. *Rev. Sci. Instruments*, **71**:4561, 2000.

[6] T. Strick, J. Allemand, D. Bensimon, A. Bensimon, and V. Croquette. *Science*, **271**:1835, 1996.

[7] C. Haber and D. Wirtz. *Rev. Sci. Instruments*, **71**:4561, 2000.

[8] R. Bernal, P. Pullarkat, and F. Melo. *Phys. Rev. Lett.*, **99**:018301, 2007.

[9] T. Dennerll, P. Lamoureux, R. Buxbaum, and S. Heidemann. *J. Cell Biology*, **109**:3073, 1989.

[10] N. Desprat, A. Guiroy, and A. Asnacios. *Rev. Sci. Instruments*, **77**:055111, 2006.

[11] P. Fernandez, P. Pullarkat, and A. Ott. *Biophys. J.*, **90**:1, 2006.

[12] O. Thoumine and A. Ott. *J. Cell Science*, **110**:2109, 1997.

[13] P. Cluzel, A. Lebrun, C. Heller, R. Lavery, J. Viovy, D. Chatenay, and F. Caron. *Science*, **271**:792–794, 1996.

[14] S. Smith, L. Finzi, and C. Bustamante. *Science*, **258**:1122, 1992.

[15] H. Mahmood T.J. Moon C. Casey Cunningham J. Guck, R. Ananthakrishnan and J. Kas. *Biophys. J.*, **81**:767–784, 2001.

[16] D. Simson, F. Ziemann, M. Strigl, and R. Merkel. *Biophys. J.*, **74**:2080, 1998.

[17] D. Cheneler, M. Ward, M. Adams, and Z. Zhang. *Sensors and Actuators B*, **130**:701, 2008.

[18] S. Jericho, M. Jericho, T. Hubbard, and M. Kujath. *Rev. Sci. Instruments*, **75**:1280, 2004.

[19] P G Haydon E Henderson and D S Sakaguchi. *Science*, **257**:1944–1946, 1992.

[20] Jianwu Dai and Michael P. Sheetz. *Biophys. J.*, **77**:3363–3370, 1995.

[21] Jianwu Dai and Michael P. Sheetz. *Biophys. J.*, **68**:988–996, 1999.

[22] Carlos Bustamante and Claudio Rivetti. *Annu. Rev. Biophys. Biomol. Struct.*, **25**:395–429, 1996.

[23] Julio M. Fernandez and Hongbin Li. *Science*, **303**:1674–1678, 2004.

[24] Robert Landick R. John Davenport, Gijs J. L. Wuite and Carlos Bustamante. *Science*, **287**:2497–2500, 2000.

[25] Joshua W. Shaevitz Robert Landick Elio A. Abbondanzieri, William J. Greenleaf and Steven M. Block. *Nature*, **438**:460–465, 2005.

[26] Mark J. Schnitzer Koen Visscher and StevenM. Block. *Nature*, **400**:184–189, 1999.

[27] Gautel M. Oesterhelt F. Fernandez J.M. Rief, M. and H.E. Gaub. *Science*, **276**:1109–1112, 1997.

[28] Kevan Larizadeh Kevin Travers Daniel Herschlag Michael T. Woodside, William M. Behnke-Parks and Steven M. Block. *Proc. Natl. Acad. Sci. U.S.A.*, **103**:6190–6195, 2006.

[29] Hummer G and Szabo A. *Acc. Chem. Res.*, **38**:504–513, 2005.

[30] Evan Evans. *Annu. Rev. Biophys. Biomol. Struct.*, **30**:105–128, 2001.

[31] Jarzynski C. *Phys. Rev.Lett.*, **78**:2690–2693, 1997.

[32] H. Barnes, J. Hutton, and K. Walters. *Introduction to Rheology.* Elsevier, 1989.

[33] G. McKinley and T. Sridhar. *Annu. Rev. Fluid Mech.*, **34**:375, 2002.

[34] C. Petrie. *J. Non-Newt. Fluid Mech.*, **137**:15, 2006.

[35] T. Sridhar, V. Tirtaatmadja, D. Nguyen, and R. Gupta. *J. Non-Newt. Fluid Mech.*, **40**:271, 1991.

[36] Peter Szabo. *Rheol Acta.*, **36**:277–284, 1997.

[37] A. Bazilevsky, V. Entov, and A. Rozhkov. In D. Oliver, editor, *Third European Rheology Conference*, pages 41–43, New York, 1990. Elsevier.

[38] G. McKinley and A. Tripathi. *J. Rheol.*, **44**:653, 2000.

[39] J. Meissner. *Annu. Rev. Fluid Mech.*, **17**:45, 1985.

[40] M. Sentmanat, B. Wang, and G. McKinley. *J. Rheology*, **49**:585, 2005.

[41] A. Bausch, F. Ziemann, A. Boulbitch, K. Jacobson, and E. Sackmann. *Biophys. J.*, **75**:2038–2049, 1998.

[42] James P. Butler Michael Glogauer Daniel Navajas Ben Fabry, Geoffrey N. Maksym and Jeffrey J. Fredberg. *Phys. Rev. Lett.*, **87**:148102, 2001.

[43] Ben Fabry Madavi Oliver David A. Weitz VirgileViasnoff James P Butler Predrag Bursac, Guillaume Lenormand and Jeffrey J Fredberg. *Nat.Mater.*, **4**:557, 2005.

[44] A. Davies J. C. Crocker A.W. C. Lau, B. D. Hoffman and T. C. Lubensky. *Phys. Rev. Lett.*, **91**:198101, 2003.

[45] C. F. Schmidt Daisuke Mizuno, Catherine Tardin and F. C. MacKintosh. *Science*, **315**:370, 2007.

[46] D. Saha D. Smith D. Humphrey, C. Duggan and J. Kas. *Nature(London)*, **416**:413, 2002.

[47] F. Julicher J. Prost K. Kruse, J. F. Joanny and K. Sekimoto. *Phys. Rev. Lett.*, **92**:078101, 2004.

[48] J. Toner and Y. Tu. *Phys. Rev. Lett.*, **75**:4326, 1995.

[49] Yuhai Tu John Toner and Sriram Ramaswamy. *Ann. Phys. (Leipzig).*, **318**: 170, 2005.

[50] S.ramaswamy et al. *europhys. Lett.*, **62**:196, 2003.

[51] H.C.Berg. *E.coli in Motion.* Springer, New York, 2004.

[52] X.L. Wu and A. Libchaber. *Phys. Rev. Lett.*, **84**:3017, 2000.

[53] X.L. Wu and A. Libchaber. *Phys. Rev. Lett.*, **86**:557, 2001.

[54] Christopher Dombrowski Charles W. Wolgemuth John O. Kessler Idan Tuval, Luis Cisneros and Raymond E. Goldstein. *Proc. Natl. Acad. Sci. U.S.A.*, **102**:2277, 2005.

[55] Sunita Chatkaew Raymond E. Goldstein Christopher Dombrowski, Luis Cisneros and John O. Kessler. *Phys. Rev. Lett.*, **93**:098103, 2004.

[56] Emil A. Yuzbashyan Hai Lin Nicholas C. Darnton Jeffry B. Stock Pascal Silberzan Sungsu Park, Peter M. Wolanin and Robert austin. *Proc. Natl. Acad. Sci. U.S.A.*, **100**:13910, 2003.

[57] R. A. Simha and S. Ramaswamy. *Phys. Rev. Lett.*, **89**:058101, 2002.

[58] Madan Rao Yashodhan Hatwalne, Sriram Ramaswamy and R. Aditi Simha. *Phys. Rev. Lett.*, **92**:118101, 2004.

[59] Francesco Ginelli Hugues Chate and Rau Montagne. *Phys. Rev. Lett.*, **96**: 180602, 2006.

[60] S. Mishra and S. Ramaswamy. *Phys. Rev. Lett.*, **97**:090602, 2006.

[61] Matthias Rief Hauke Clausen-Schaumann Michel Grandbois, Martin Beyer and Hermann E. Gaub. *Science*, **283**:1727, 1999.

[62] H.B. Fernandez, J.M.and Li. *Science*, **303**:1674–1678, 2004.

[63] L A Chrisey G U Lee and R J Colton. *Science*, **266**:771–773, 1994.

[64] P Wagner D Anselmetti-HJ Guntherodt U Dammer, O Popescu and GN Misevic. *Science*, **267**(5201):1173–1175, 1995.

[65] E. Vincent-J. Hammann A. S. Wills, 1 V. Dupuis and R. Calemczu. *PHYSICAL REVIEW B*, **62**(14):9264–9267, 2000.

[66] VT Moy EL Florin and HE Gaub. *Science*, **264**(5157):415–417, 1994.

[67] Matthew T. Smith Michelle L. Duval Traci R. Jensen John C. Hulteen, David A. Treichel and Richard P. Van Duyne. *J. Phys. Chem. B.*, **103**:3854–3863, 1999.

[68] R. M. Overney H. Heinzelmann J. Frommer H.J. Gntherodt T. Wagner H. Schier E. Meyer, L. Howald and S. Roth. *Nature.*, **349**:398–400, 1991.

[69] Goldstein L.S. Block, S.M. and B.J. Schnapp. *Nature*, **348**:348–352, 1990.

[70] K. Svoboda and S.M. Block. *Cell*, **77**:773–784, 1994.

[71] Mammen M. et al. *Chem. Biol.*, **3**:757–763, 1996.

[72] Siao CJ Berno A Young P Sapolsky R Ghandour G Perkins N Winchester E Spencer J Kruglyak L Stein L Hsie L Topaloglou T Hubbel E Robinson E Mittmann M Morris MS Shen N Kilburn D Rioux J Nusbaum C Rozen S Hudson TJ Lipshutz R Chee M Wang DG, Fan JB and Lander ES. *Science*, **282**:902–907, 1998.

[73] Becky J. Wong Rachel A. Mooney Keir C. Neuman Robert Landick Kristina M. Herbert, Arthur La Porta and Steven M. Block. *Cell*, **125**:1083–1094, 2006.

[74] Abbondanzieri E.A. Landick R. Gelles J. Neuman, K.C. and S.M. Block. *Cell*, **125**:437–447, 2003.

[75] Abbondanzieri E.A. Landick R. Shaevitz, J.W. and S.M. Block. *Nature*, **426**:684–687, 2003.

[76] Moller W. Bausch, A.R. and E. Sackmann. *Biophys. J.*, **76**:573–579, 1999.

[77] Schilling J. Keller, M. and E. Sackmann. *Rev. Sci. Inst.*, **72**:3526–3634, 2001.

[78] Strick T.R. Bensimon D. Charvin, G. and V. Croquette. *Annu. Rev. Biophys. Biomol. Struct.*, **34**:201–219, 2005.

[79] Vincent Croquette Terence R. Strick and David Bensimon. *Nature*, **404**: 901–904, 2000.

[80] D. Tabor and R.H.S. Winterton. *Proc. R. Soc. Lond. A.*, **312**:435–440, 1970.

[81] Jacob N. Israelachvili. *Intermolecular and Surface Forces.* Elsevier Science, 1991.

[82] Israelachvili JN and Tabor D. *Proc R Soc London Ser A.*, **331**:19–38, 1972.

[83] Dennis Bray. *Dev Biol.*, **102**(2):379–389, 1984.

[84] Robert E. Buxbaum Steven R. Heidemann, Stefanie Kaech and Andrew Matus. *The Journal of Cell Biology.*, **145**(1):109–122, 1999.

[85] Nathalie Q. Balaban Ulrich S. Schwarz Toshimasa Ishizaki Shuh Narumiya Zvi Kam Benjamin Geiger Daniel Riveline, Eli Zamir and Alexander D. Bershadsky. *The Journal of Cell Biology.*, **153**(6):1175–1185, 2001.

[86] Robert E. Buxbaum Philip Lamoureux and Steven R. Heidemann. *Nature.*, **340**:159–162, 1989.

[87] B. Lincoln R. Ananthakrishnan M. Romeyke J. Guck F.Wottawah, S. Schinkinger and J. Kas.

[88] L. Landau and L. Lifshitz. *Theory of Elasticity.* Pergamon Press, 1986.

[89] Zhdan P. Cumpson, P.J. and J. Hedley. *Ultramicroscopy.*, **100**:241–251, 2004.

[90] James W. M. Chon John E. Sader and Paul Mulvaney. *Rev. Sci. Instruments*, 70:3967, 1999.

[91] Jeffrey L. Hutter and John Bechhoefer. *Rev. Sci. Instruments*, 64:1868, 1993.

[92] H. Butt and M. Jaschke. *Nanotechology*, **6**:1, 1995.

[93] D. Bocek J. P. Cleveland, S. Manne and P. K. Hansma. *Rev. Sci. Instruments*, 64:403, 1993.

[94] C SHodges GAMatei E J Thoreson C J Roberts M C Davies NABurnham, XChen and S J B Tendler. *Nanotechology*, 14:1–6, 2003.

[95] Charlie Gosse and Vincent Croquette. *Biophys. J.*, **82**:3314–3329, 2002.

[96] Chirag Kalelkar Seshagiri Rao R. V. and Pramod A. Pullarkat. *Rev. Sci. Instruments*, **84**:105107, 2013.

[97] Yongqing Cao Paul I. Ro Qingquan Qin, Feng Xu and Yong Zhu. *Small.*, pages 1–6, 2012.

[98] Changhui Rao Xiaoyu Ma and Hanqing Zheng. *OPTICS EXPRESS*, **17(10)**: 8525, 2009.

[99] R. Changhui M. Xiaoyu and Z. Xuejun. *Acta Opt .Sin.*, **5**:882–888, 2007.

[100] Sue Kim Donald L. Koch Mingming Wu, John W. Roberts and Matthew P. DeLisa. *Appl. Environ. Microbiol.*, **72(7)**:4987–4994, 2006.

[101] L. A. Hough M. F. Islam M. Goulian T. C. Lubensky D. T. N. Chen, A.W. C. Lau and A. G. Yodh. *Phys. Rev. Lett.*, **99**:148302, 2007.

[102] J. P. Gollub Adriana I. Pesci Kyriacos C. Leptos, Jeffrey S. Guasto and Raymond E. Goldstein. *Phys. Rev. Lett.*, **103**:198103, 2009.

[103] Michael G.Surette Blaise Aguera y Arcas Yi Liu Stanislas Leibler1 Uri Alon, Laura Camarena and Jeffry B.Stock. *The EMBO Journal.*, **17**(15):4238–4248, 1998.

[104] J. Sambrook and D. Russell. *Molecular Cloning: A Laboratory Manual.* Cold Spring Harbor Laboratory Press, Cold Spring Harbor, New York, 2001.

[105] Herman C. Lichstein and Malcolm H. Soule. *J Bacteriol.*, **47**(3):221–230, 1944.

[106] V. Balakrishnan. *Elememnts of Nonequilibrium Statistical Mechanics.* Ane books Pvt.Ltd, New Delhi, 2009.

[107] H A Barnes. *A Hand book of Elementary Rheology.* Institute of Non-Newtonian Fluid Mechanics, University of Wales, 2000.

[108] Haake caBER manual. *Thermo Haake.* USA.

[109] R G Larson. *Constitutive equations for polymer melts and solutions.* Butterworths, Boston, 1988.

[110] J. Dealy and K. Wissbrun. *Melt rheology and its role in plastics procession - Theory and applications.* Springer, 1999.